Vibrations and Energy Transfer in Molecules Enhanced by Single Nanoantennas

Doctoral Thesis
by

Jana Ockova

Thesis advisor:
Prof. Niek F. van Hulst

ICFO - Institut de Ciències Fotòniques

BIST - Barcelona Institute of Science and Technology

UPC - Universitat Politècnica de Catalunya

December 2023

Thesis advisor
Prof. Niek F. van Hulst

Thesis committee
Dr. Emilie Wientjes (WUR - Wageningen University & Research, Netherlands)

Prof. Eric O. Potma (UCI - University of California, Irvine, USA)

Prof. María F. García-Parajo (ICFO - Institut de Ciències Fotòniques, Castelldefels, Spain)

Contribution statement

All work presented in this thesis is my own, unless explicitly stated otherwise. The grammatical use of plural of the first person reflects the crucial role of collaboration in the scientific process.

Abstract

Light is a powerful non-invasive tool for probing matter down to its fundamental molecular properties. The past three decades saw advent of metallic nanoantennas engineered to concentrate light into sub-diffraction limited hotspots and enhance optical properties of nearby emitters by many orders of magnitude. This boosted optical microscopy, allowing it to interrogate even extremely dim systems at their most fundamental single-molecule level. The enhancement and local confinement also unlocked sensing applications down to zeptomolar concentrations, which can revolutionise environmental monitoring, clinical diagnosis and personalised medicine. Beyond sensing, metallic nanoparticles can improve the efficiency of photovoltaic devices and next generation green catalysts. The current challenge for large-scale practical implementations is lack of understanding and control of the underlying nanoscale processes. Here, we use optical microscopy and metallic nanoantennas to perform single-molecule and single-particle experiments to shed light on fundamental mechanism of photosynthesis, nanoscale parameters crucial for sensing and underlying photochemistry in nanoantenna hotspots relevant for catalysis.

Firstly, we employ gold nanorods and cryomicroscopy to study excitation energy transfer in the Fenna-Matthews-Olson photosynthetic complex. By probing one complex at a time at room temperature and 77 K, we uncover energy transfer between its subunits, where both experimental approaches constitute the first of their kind for this extremely dim system. Furthermore, we show that maximising the nanorod enhancement likely yields more efficient energy transfer to the nanorod than between the subunits of the complex, making them operate as effectively independent. Our results shed new light on the role of excitation transfer and annihilation in the regulation of photosynthesis.

Next, we evaluate Raman scattering enhancement of a library of ten nanoparticles using a home-built automated Raman microscope. By recording a statistically-significant dataset of spectral traces from discrete nanoscale spots, we can distinguish Raman enhancement performance of different types of nanoparticles that would otherwise appear identical in classical bulk measurements. Furthermore, adding a dark-field scattering detection allows us to classify the measurements between single and multiple nanoparticles and directly probe the variability of single-particle enhancements. This is a crucial parameter for sensing applications and the detailed nanoscale insight provided by our measurement platform can be used to accelerate the rational design of new nanoparticles for quantitative sensing.

Finally, we employ the automated Raman microscope to study light-induced chemical reactions in metallic nanocavities. Specifically, we record surface enhanced Raman scattering of a few methylene blue molecules sandwiched between a gold mirror and a gold nanoparticle. We develop a new sample assembly compatible with oil immersion that yields a 150-fold increase in the molecular signal than previously published air-coupling schemes. We use a pulsed laser to induce a chemical transformation of the methylene blue molecules. By interpreting the results in the context of plasmonic properties of the gold nanojunction obtained from dark-field measurements and simulations, we were able to rule out lattice heating and narrow down the underlying mechanism to a plasmon-induced sub-picosecond process. Furthermore, we propose that spontaneous picosecond Raman spectroscopy is suitable to study reactions at metallic surfaces, which lie at the heart of heterogeneous catalysis.

Resum

La llum és una eina no invasiva de gran utilitat per a investigar la matèria fins a les seves propietats moleculars més fonamentals. En les últimes tres dècades, hem vist l'aparició de nanoantenes metàl·liques dissenyades per a concentrar llum en punts calents, i amplificar així les propietats òptiques dels emissors propers en molts ordres de magnitud. Això ha augmentat les possibilitats que ens ofereix la microscòpia òptica i ha permès d'interrogar, fins i tot, sistemes extremadament tènues al nivell de molècula única. La capacitat de concentrar la llum localment també ha anat acompanyada d'aplicacions de detecció fins a concentracions zeptomolars, que poden revolucionar el control ambiental, el diagnòstic clínic i la medicina personalitzada. Més enllà de la detecció, les nanopartícules metàl·liques poden millorar l'eficiència dels dispositius fotovoltaics i dels catalitzadors verds de nova generació. El repte actual per a la implementació pràctica a gran escala és la manca de comprensió i control dels processos a nanoescala implicats. En aquesta tesi, utilitzem la microscòpia òptica i nanoantenes metàl·liques per a dur a terme experiments de molècula i partícula única per a estudiar el mecanisme fonamental de la fotosíntesi, analitzar paràmetres a nanoescala crucials per a la detecció i la fotoquímica subjacent en punts calents de nanoantenes rellevants per a la catàlisi. En primer lloc, utilitzem nanorods d'or i criomicroscòpia per a estudiar la transferència d'energia d'excitació en el complex fotosintètic de Fenna Matthews Olson. En experiments a temperatura ambient i a 77 K, mesurem aquesta transferència entre les seves subunitats, on ambdós enfocaments experimentals constitueixen el primer d'aquest tipus en aquest sistema extremadament tènue. A més, mostrem que maximitzar l'amplificació del nanorod produeix una transferència d'energia més eficient cap a ell que no pas entre les subunitats del complex, fent que funcionin independentment. Els nostres resultats aporten nous coneixements sobre la transferència d'excitació i aniquilació en la regulació de la fotosíntesi. A continuació, avaluem l'amplificació en la dispersió Raman d'una col·lecció de deu nanopartícules mitjançant un microscopi Raman automatitzat construït a al nostre laboratori. Enregistrant un conjunt de traces espectrals de punts discrets a nanoescala, podem discernir l'amplificació Raman de diferents tipus de nanopartícules que semblarien idèntiques en les mesures clàssiques a nivell macroscòpic. A més a més, amb un sistema de detecció de camp fosc podem classificar les mesures entre nanopartícules simples i múltiples i copsar directament la variabilitat en l'amplificació de partícula única. Aquest és un paràmetre crucial per a les aplicacions de detecció i la visió a nanoescala proporcionada per la nostra plataforma de mesura es pot utilitzar per al disseny de noves nanopartícules per a detecció quantitativa. Finalment, emprem el microscopi Raman automatitzat per a

estudiar reaccions químiques induïdes amb llum en nanocavitats metàl·liques. Concretament, enregistrem la dispersió Raman amplificada en superfície d'unes quantes molècules de blau de metilè situades entre un mirall d'or i una nanopartícula d'or. Hem desenvolupat un nou muntatge compatible amb la immersió en oli que produeix un augment de 150 vegades en el senyal molecular que els muntatges en aire publicats anteriorment. Utilitzem un làser polsat per induir una transformació química de les molècules de blau de metilè. Interpretant els resultats en el context de les propietats plasmòniques de la nanounió d'or obtinguda a partir de mesures i simulacions de camp fosc, podem descartar l'escalfament de la xarxa i reduir el mecanisme subjacent a un procés sub-picosegon induït pel plasmó. A més, proposem que l'espectroscòpia Raman de picosegon espontània és adequada per estudiar reaccions en superfícies metàl·liques que es troben al cor de la catàlisi heterogènia.

Contents

1 Introduction

1.1 Historical background

Investigating matter using light is deeply rooted in our genome. Our eyesight evolved to be the most dominant of our senses: edge recognition allows us to perceive object boundaries and our advanced colour perception[1] yields crucial information on properties of objects such as ripeness of a fruit or emotional state of a fellow human based on a rush of blood to their face.[2] In the second half of the 16th century, we started to use the modern scientific approach to describe the natural world systematically and in detail. For example, in 1565 a Spanish physician Nicolás Monardes recorded an appearance of a bright blue tinge in water upon addition of wooden chips from a medicinal tree from Mexico.[3] This constitutes the first modern written record of fluorescence, long before the term was coined and its mechanism understood. As the scientific methods developed, so did the tools. In the 1600s, the invention of the first microscope and its subsequent popularisation as a scientific instrument by Antony Van Leeuwenhoek led to an explosion of our ability to "recognise edges" down to the scale of microbial life.[4] Concurrently, the prism experiment of Sir Isaac Newton revealed the individual colour components of white light improving our understanding of light as a spectrum.[5]

The 18th and 19th century saw a wealth of "object recognition" on the microscale aimed at understanding the building blocks of the natural world and in 1873 a German physicist Ernst Karl Abbe defined the resolution limit of optical microscopy as approximately half of the wavelength of light.[6] On the spectral side, towards the end of the 19th century, Sir George Gabriel Stokes used the prism to separate white light into its components to illuminate fluorescent substances and observed that fluorescence (a term he coined) was always redshifted with respect to the illumination colour.[7] Later in the 20th century, a Polish physicist Aleksander Jablonski explained the "redshifted light reemission" in terms of energy levels of the fluorescent molecules, linking information encoded in the colour of light to the energy structure of the molecules.

Within just three centuries, human investigation of the natural world developed from observations by a naked eye under natural sunlight towards nanoscale insight down to the level of single cells and organelles, with a spectral resolution pointing towards the energy structure of the constituent molecules. In 1989, optical microscopy reached a new milestone: observation of light absorption by a single molecule,[8] which was quickly followed by single-molecule fluorescence.[9] These molecular optical signatures can be greatly enhanced at surfaces of metals, which

was first observed in 1974 for pyridine molecules adsorbed on a silver electrode.[10] In 1989, the first experimental demonstration of a metallic nanoparticle acting as an antenna for light,[11] opening up possibilities for nanoparticle-enhanced single-molecule microscopy.

Nowadays, single-molecule microscopy belongs among the most powerful optical investigation methods thanks to its ability to probe matter at its fundamental molecular level. For example, it is sensitive to nanoscale variations of molecular conformations and their local environment. It also yields a more complete picture by revealing the underlying distribution for each measured parameter rather than the averaged value.[12,13] Moreover, metallic nanoantennas make single-molecule techniques possible for a wide range of molecules, including ones with small optical cross-sections or emission efficiencies.[14,15] In this thesis, we employ metallic nanoantennas and optical microscopy to study light-induced photochemistry at a single-molecule or single-nanoparticle level.

1.2 Thesis outline

In chapter 2, we cover the theoretical considerations necessary to understand the work in this thesis. We briefly outline the microscopy considerations specific to the single-molecule techniques, introduce the underlying mechanism of molecular signatures probed in this work and explain the physics governing the metallic nanoantennas and their interaction with nearby molecules.

In chapter 3, we study excitation energy transfer in the Fenna-Matthews-Olson photosynthetic complex. By employing gold nanorod antennas and a confocal microscope coupled to a cryostat, we managed to observe the photosynthetic complexes one at a time for the first time at room temperature and 77 K. We employed single-molecule photon statistics to gain a direct insight into the energy transfer within each complex and observed a regime where energy transfer to the nanorods themselves efficiently competed with that among the individual subunits of the complex.

Chapter 4 describes an automated microscope we developed for high-throughput single-spot or single-particle Raman spectroscopy. It combines wide-field imaging with particle recognition and a fibre-coupled spectrometer to scan samples, identify bright spots and acquire their Raman spectra. We employed it at two different wavelengths to ten nanoparticle types to systematically compare their ability to enhance molecular Raman scattering. For each sample, we recorded a statistically-significant single-spot dataset that yielded a detailed nanoscale insight unavailable in bulk techniques. Moreover, by combining dark-field imaging with the

collected spectra, we could identify the variations of performance among single and multiple nanoparticles, which is crucial for their practical applications like sensing.

In chapter 5, we lay grounds for interrogating chemical processes in metallic nanocavities in a time-resolved fashion. We used self-assembled nanojunction of a gold nanoparticle separated from a gold surface by the molecules of interest in combination with the single-particle microscope with spectral resolution introduced in chapter 4. We monitored the Raman signature of the few molecules in each nanojunction as a function of illumination with a pulsed laser that induced a chemical change. Varying the pulse length and power, we revealed two regimes of Raman modulations: a linear regime at low powers and a peak-power dependent regime that dominated above a certain peak power threshold. By running simulations and measuring dark-field scattering spectra of the system, we correlated the damage to the near-field response of the nanojunction. Based on this correlation and experimentally-retrieved timescale and power dependency, we eliminated gold lattice heating as the underlying mechanism, narrowing it down to a few likely ultrafast plasmon-mediated processes. The observed power dependency and our preliminary time-resolved data propose spontaneous Raman techniques as suitable for ultrafast measurements of photochemistry at metallic surfaces.

Lastly, in chapter 6 we summarise the findings of this thesis within the context of both, its contribution to the fundamental understanding of the natural world, as well as towards practical applications and suggest possible directions for further research.

2 Theory

In this chapter, we cover the theoretical concepts that will allow the reader to understand the work presented in this thesis. We outline a few simple, yet important microscopy considerations specific to single-molecule methods. We then cover the basic principles of two light-driven molecular processes studied in this thesis: fluorescence and Raman scattering. Furthermore, we describe in detail the mechanism of plasmonic enhancement that lies at the heart of the experiments in this thesis. Outlining the properties of metals that give rise to plasmonic behaviour, we cover plasmon-polaritons at metallic surfaces and their localised counterpart in metallic nanoantennas. We finish by describing the interaction of molecules with the nanoantennas in the context of fluorescence and Raman scattering.

2.1 Single-molecule considerations in microscopy and spectroscopy

Optical experiments interrogate the interaction of light with molecules to address scientific questions. In a typical experiment "in a cuvette", many molecules are probed at the same time. For example, 1 mL of water contains ~ 10^{22} molecules. Such a measurement thus reports on the average value of properties within the probed ensemble of molecules. A more fundamental insight may be obtained from single-molecule (SM) experiments. For instance, the SM approach is sensitive to different molecular isomers, conformation states and variations in the local environment.[12,14] By measuring an observable one molecule at a time, one can also reconstruct its underlying distribution that contains much more detailed information than the averaged value. For example, the number of distribution peaks can identify different subpopulations within the sample and the distribution width reports on the heterogeneity among the molecules. Furthermore, if multiple observables are measured one molecule at a time, they can be correlated, elucidating their interplay at the most fundamental SM limit. Finally, SM experiments can yield entirely new insights unavailable in ensemble measurements such as uncovering the quantum emission statistics of a molecule by recording both the number and the timestamp of photons emitted by the molecule. We describe this technique in detail in chapter 3.

The valuable SM insight comes at a cost of several experimental challenges that must be overcome. The vanishingly small signal of single molecules requires a high sensitivity that is often achieved by using a microscope in combination with the equipment specific to the technique of choice. The minimum beam spot at the focus of a microscope is fundamentally limited by light diffraction resulting in an Airy pattern where 86 % of the intensity is contained in a bright central spot that is surrounded by progressively dimmer concentric rings.[16] The diameter of the central spot is given by:

$$d = \frac{1.22\,\lambda}{NA} \qquad (2.1)$$

where λ is the wavelength of light and NA the numerical aperture of the objective. A high-NA objective can focus 800 nm light into a ~ 10^5 nm^2 spot that is 5 orders of magnitude larger than a typical absorption cross-section of a molecule, 1 nm^2. In other words, in a high-NA confocal microscope, the signal of a single molecule is 10^5 times weaker than the laser background. Consequently, the vast majority of

single-molecule techniques detect molecular signatures spectrally offset from the illumination where the laser background can be separated using a colour filter resulting in a background-free detection.[12,13,17] The SM detection can then be achieved by sufficient detector sensitivity and inter-molecular separation greater than the resolution of the microscope.

In the SM limit, the emitted photons represent a series of discrete independent events obeying a Poisson distribution. Thus, for a given number of detected photons, N, the measurement noise is equal to $\sqrt{N}$, and the signal to noise ratio, SNR, to:

$$SNR = \frac{N}{\sqrt{N}} = \sqrt{N} \qquad (2.2)$$

This relation dictates that for a 100-fold lower sampling, the SNR decreases 10 times. In other words, a SM measurement would yield 10^{11} times lower SNR compared to an ensemble experiment probing 10^{22} molecules under the same experimental conditions.

In practice, using detectors with high efficiency and extremely low noise allows recording signals as low as hundreds of photons per second. The SNR is then increased by long integration times by slowly building up the number of detected photons. However, the possible integration time is also fundamentally limited by the finite number of photons that a molecule emits before irreversibly photobleaching. The total number of photons emitted by a molecule is called a photon budget and varies depending on the molecular processes being induced by the laser light (section 2.2). Ultimately, the combination of low emission rate and finite photon budget sets a fundamental bound to the quantities observable at a SM level.

In summary, SM microscopy provides insight at the most fundamental level being sensitive to dependence of observables on nanoscopic variations in conformations and local environment. It can also probe properties inherent to single molecules such as the quantum nature of their emission available from recording the arrival time of each photon. The detected signals are many orders of magnitude weaker than the illumination background and thus most SM implementations rely on recording a spectrally-offset signal such as fluorescence and Raman scattering that can be separated from the incident illumination using optical filters. The signal strength and total length of the observation window are both fundamentally

limited, delimiting possible observables and their associated uncertainties. Below, we outline two types of molecular signatures probed in this thesis within the context of SM microscopy and strategies to amplify these signals using nanoscale metallic structures.

2.2 Fluorescence and Raman scattering of molecules

The most common spectrally-offset signals probed in SM microscopy are fluorescence and Raman scattering. Fluorescence involves a photon absorption that promotes an emitter in a ground state, S_0, into an excited electronic state, such as S_1. After an internal rearrangement of atoms called vibrational relaxation, this photon can be re-emitted with a slightly lower energy via fluorescence, bringing the molecule back into the electronic ground state (Figure 2.1).[18] Note that real electronic energy levels of the molecule are involved in fluorescence and therefore, energy of the incoming photon must match, in other words be resonant with, some electronic (or electronic and vibrational) transition of the molecule.

The S_0 - S_1 transitions are essentially instantaneous, but the total absorption and re-emission cycle occurs on a relatively long timescale of several nanoseconds. This is because the $S_0 \leftarrow S_1$ transition is a spontaneous radiative decay with probability given by the overlap of the vibrational wavefunctions of the electronic and vibrational states involved in the transitions.[19] Thus, on average, the molecule spends a few nanoseconds in a chemically-reactive excited state during each fluorescence cycle. Note that in section 2.3.4, we will outline how metallic nanoantennas enhance fluorescence of molecules by increasing the probability of radiative decay of the excited state by providing additional states into which the excited state can decay. Since fluorescence is a spontaneous decay process, the modification of the transition probability will shorten the average time the molecule spends in the excited state. We will use these concepts of fluorescence enhancement and lifetime shortening to interpret the experimental observations in chapter 3.

Raman scattering is an inelastic process where the incoming illumination is affected by molecular vibrations. When energy is imparted onto the molecule to excite a vibrational mode, the scattered light is redshifted from the laser by the characteristic frequency of the vibration resulting in “Stokes” scattering (Figure 2.1). If there is an excited vibration already present in the molecule, the reverse process can occur where the vibrational mode relaxes into the ground state by giving energy to the incident light resulting in blueshifted “anti-Stokes” scattering.[20]

Raman scattering is instantaneous in a sense that the absorption and following re-emission of a photon occur on a sub-picosecond timescale given by the vibrational coherence of the molecule. The process involves a "virtual state" (Figure 2.1), which results from the perturbation by the incident light and can be understood as a linear superposition of all eigenstates of the molecule.[21] For the purposes of this thesis, the important distinction is that the Raman process does not promote an electron into a real electronic excited state and hence does not require the incoming light to be resonant with an electronic transition of the molecule. Resonant illumination does however yield an enhancement in the Raman scattering efficiency of several orders of magnitude.[22]

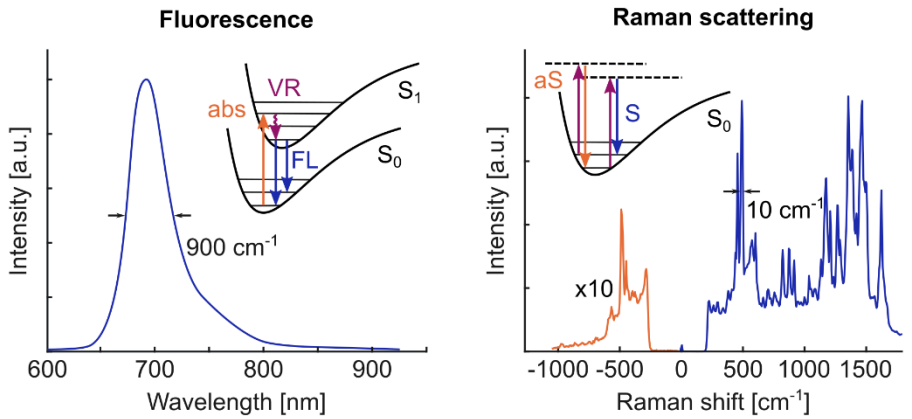

Figure 2.1 ***Fluorescence and Raman spectra of a methylene blue dye with corresponding full-width at half-maxima.*** *The underlying processes are depicted on potential energy diagrams. Fluorescence (FL) starts from a ground electronic state, S_0, with a photon absorption (abs) into an excited electronic state, S_1. Vibrational relaxation (VR) follows into the ground vibrational level of S_1 from which the system relaxes by emitting a photon. Raman scattering proceeds via a real or virtual state (dashed lines) where photons gain and lose momentum in the anti-Stokes (aS) and Stokes (S) process, respectively. The fluorescence spectrum was obtained from ref.*[23]

Understanding the molecular mechanisms of fluorescence and Raman scattering, we can outline the insight available from each technique. Typical fluorescence and Raman spectra at room temperature for a methylene blue dye molecule are shown in Figure 2.1. The fluorescence spectrum is taken from ref[23] and shows a main peak with a bandwidth of ~ 900 cm^{-1} and a sideband at ~ 760 nm. This vibronic sideband corresponds to excited state decay into a higher vibrational level of the electronic ground state (short "FL arrow" in Figure 2.1) and therefore, the overall spectrum reports on the structure of the electronic ground state of the molecule.[18] Raman spectra shed light on the nuclear motion of the molecule where different vibrations such as a C=C stretch or an O-H bend appear at a characteristic energy offset from the laser called the Raman shift.[20] The precise energy of each vibrational mode is

affected by neighbouring chemical groups making Raman signatures very specific for every molecular species. Thanks to typically ~ 2-3 orders of magnitude narrower bandwidth than fluorescence, Raman spectra provide a detailed chemical insight and the region of < 1900 cm^{-1} is often called the “fingerprint region” serving as a “molecular identification barcode”. Note that resolving the temporal evolution of the signal gives insight into the electronic excited state and vibrational relaxation for fluorescence and Raman scattering, respectively.

Both fluorescence and Raman scattering have specific advantages and disadvantages within the context of SM microscopy. Firstly, the photon budget in fluorescence is severely limited by irreversible photobleaching reactions stemming from the high reactivity of electronically-excited molecules. Among the most common is the reaction with molecular oxygen that occurs when a photoexcited molecule undergoes a singlet-triplet conversion followed by a very-efficient triplet-triplet annihilation with the ground triplet state of molecular oxygen.[24–26] The resulting singlet oxygen is highly reactive and can start irreversible chemical reactions that transform the fluorophore into a non-fluorescent species, thereby photobleaching it irreversibly. Depending on the singlet-triplet conversion and excited state lifetime, a typical photon budget of a molecule is within the range of one to a few million photons. In contrast to fluorescence, Raman scattering is virtually bleaching-free within linear illumination because the instantaneous scattering process does not promote the molecular species into a highly-reactive state. As such, possible observation times are in principle unlimited under weak illumination conditions in SM Raman experiments.

Another experimental difference between SM fluorescence and Raman scattering concerns the illumination wavelength. Whereas fluorescence requires a specific illumination wavelength given by the molecular resonance condition, the choice is flexible for Raman scattering.

Finally, the probability of each molecular process under the same illumination is vastly different. A typical fluorescence cross-section of a molecule is approximately 10^{-15} cm^2, up to 15 orders of magnitude larger than the Raman scattering cross-section of 10^{-30} - 10^{-26}.[27] In fact, fluorescence background can completely overwhelm the Raman scattering signal and an intelligent wavelength choice and amplification of the Raman scattering are crucial for SM Raman experiments.

To summarise, fluorescence is a multi-step process probing molecular properties related to electronic excitation whereas Raman scattering is instantaneous and reports on vibrations of the atomic nuclei. The main experimental advantage of

fluorescence detection in SM microscopy is 11-15 orders of magnitude higher brightness compared to the Raman signal, however, extra care must be taken to avoid irreversible photobleaching of the reactive excited state. If sufficient signal amplification is reached, Raman scattering can offer more chemically-rich information with virtually no photobleaching mechanism at low illumination intensities. Below, we outline how the abovementioned experimental requirements can be addressed by the use of nanoscale metallic antennas.

2.3 Plasmonic nanoantennas

2.3.1 Properties of metals

To understand the physics of nanoscale metallic objects, it is useful to outline some properties of bulk metals. The simplest, plasma, model describes metals as a cloud of free electrons moving against a constant background of positive ions. Developed before the structure of atoms was understood, the model only strictly applies to the conduction electrons. However, it still correctly describes macroscopic properties of metals relevant for this thesis and as such, serves as a useful framework for our understanding. Describing the metal via the plasma model, its interaction with light can be derived from the motion of electrons in the plasma sea, which is the basis for the Drude model developed in the 1900.[28] Instead of outlining the derivation thoroughly covered in textbooks,[29,30] we focus on its phenomenological implications. According to the Drude model, the natural oscillation frequency of electrons in the plasma, the plasma frequency ω_p, is given by the number of free electrons, n_e, electron charge, e, mass of the electrons, m, and the dielectric permittivity, ε_0:

$$\omega_p = \sqrt{\frac{n_e e}{m\,\varepsilon_0}} \tag{2.3}$$

Note that, ω_p is determined by the density of free electrons, which is a characteristic property of each metal. The interaction of the metal with light is fully-described by a frequency-dependent dielectric function of metals, $\varepsilon(\omega)$, that depends on the plasma frequency and the damping of the electron motion due to collisions, γ:

$$\varepsilon(\omega) = 1 - \frac{\omega_p^2}{\omega^2 + i\gamma\omega} \tag{2.4}$$

The real part of $\varepsilon(\omega)$ describes the phase velocity of light propagating through the material and the imaginary part the light absorption by the material.

Noting that the collision frequency is lower than the frequency of the light wave, we can identify frequency regions with interesting optical properties. When $\omega < \omega_p$, $Re\big(\varepsilon(\omega)\big) < 0$ and the metal is reflective as the free electrons screen the incoming electromagnetic field that consequently does not penetrate deep into the metal. At the same time, $Im\big(\varepsilon(\omega)\big)$ decreases with increasing ω and therefore, at ω just below the ω_p, the metal should be both reflective (non-transparent) and with little contribution from absorption.

The experimentally-determined[31] dielectric functions of the most commonly used metals in plasmonics, gold and silver, are plotted on a wavelength axis in Figure 2.2. The corresponding plasma frequencies (2.4 eV for Au[32] and 4.0 eV for Ag[33]) are marked by vertical dashed lines. At wavelengths above (frequencies below) the plasma frequency, the Drude model holds well showing a negative $Re\big(\varepsilon(\omega)\big)$ decreasing with increasing wavelength and a positive $Im\big(\varepsilon(\omega)\big)$ that increases with increasing wavelength. In the short wavelength region close to plasma frequency, Drude model breaks down because the incoming photons reach sufficient energies to promote bound electrons from the d-shell into the higher energy sp-band.[20,30] These inter-band electronic transitions result in an increased absorption as seen in the rise of $Im\big(\varepsilon(\omega)\big)$ that is not predicted by the Drude model. In this thesis, all experiments are conducted within 600-900 nm where the Drude model remains valid.

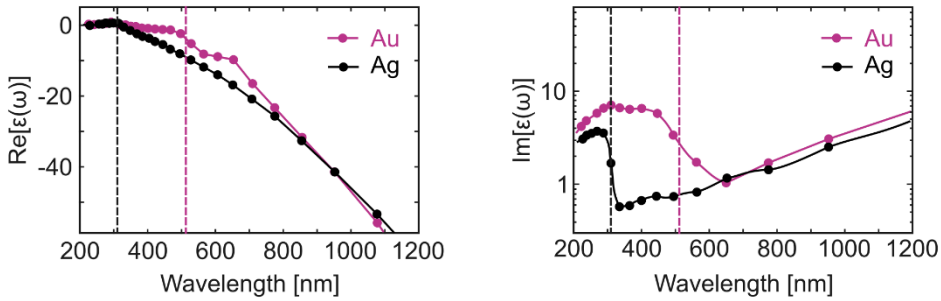

Figure 2.2 ***Wavelength-dependent dielectric function of silver and gold*** *from ref.[31] The plasma frequencies marking the onset of inter-band transitions are shown as vertical dashed lines.*

Comparing the dielectric function of Ag and Au, the main difference lies in the significantly blueshifted plasma frequency of silver. This is actually the reason for the more yellowish hue of bulk gold compared to silver. Furthermore, silver also yields slightly superior metallic properties of negative $Re\big(\varepsilon(\omega)\big)$ and low $Im\big(\varepsilon(\omega)\big)$.

Thus, in general but especially for experiments below 600 nm, it may be advantageous to employ silver. However, silver is prone to oxidation by molecular oxygen in air and must often be handled in inert atmosphere. Hence both gold and silver are widely-used nowadays and this thesis relies mostly on gold nanostructures with a few examples of silver-based platforms.

2.3.2 Surface plasmon-polaritons

The unique combination of high reflectivity and low absorbance is well-suited for light-driven modulation of the free electrons with high efficiencies, which lies at the heart of plasmonics. So far, we have not however explained what a plasmon was. Actually, the term plasmon strictly refers to collective electron oscillations inside the bulk metal at the plasma frequency.[20] This electric wave is longitudinal in nature and as such does not couple to photons that travel as a transverse electromagnetic wave. The optical modes related to light-driven electron oscillations are called surface plasmon-polaritons (SPPs). SPPs arise from coupling of the free electron oscillations at the surface of the metal to electromagnetic fields and the term plasmon-polariton highlights the part-plasmon and part-photon nature of the mode. The resulting electromagnetic wave propagates along the interface, but decays exponentially in the direction normal to the surface. Interestingly, stemming from Maxwell's equations, the presence of an interface is actually necessary to sustain SPP modes because of the condition:

$$\frac{k_2}{k_1} = -\frac{\varepsilon_1}{\varepsilon_2}$$

(2.5)

where the indices 1,2 refer to the two materials at the interface, k is the wavevector perpendicular to the interface and ε the dielectric function that can be expressed using the Drude model explained above. For the condition to be satisfied, the real part of the dielectric functions of the two materials must have opposite signs such as in the case for a metal and a dielectric. There are also two important properties that we can deduce from this condition. Firstly, since ε of metals is large, the wavevector in the dielectric medium is also large yielding a short effective wavelength of the SPP. Secondly, the properties of the plasmon-polaritons are affected not only by the properties of the metal, but also by the surrounding medium marking them as interesting local probes of nanoscopic environments.

The sub-diffraction spatial extent (both along and perpendicular to the surface) and sensitivity to the dielectric medium make SPPs powerful probes of local environment at the metallic surface. However, SPP-based sensing is complicated to

implement practically because it is not trivial to launch SPPs due to momentum and frequency requirements for the incoming photon stemming from momentum and energy conservation in the Maxwell's equations. The derivation of the conditions is thoroughly described in textbooks,[20,30] but briefly, the main practical obstacle stems from the fact that the plasmon-polariton mode has a momentum parallel to the surface larger than that of the propagating photons impinging on it. To overcome this issue, coupling schemes based on total internal reflection were devised by Otto[34] and Kretschmann[35] where the plasmon-polariton is launched using the evanescent wave produced during the total internal reflection.

The momentum conservation condition stems from translational symmetry of the infinite metal sheet discussed thus far. Engraving a grating onto the metallic surface or simply introducing random surface roughness or defects breaks the translational invariance creating local sources of the SPP when the surface is illuminated by free propagating waves.[36] An extreme case where the momentum conservation requirement is completely relaxed is for metallic nanostructures with multiple dimensions smaller than the wavelength of the electromagnetic radiation. The resulting plasmon-polariton mode is non-propagating due to its confinement by the nanostructure and is therefore called a localised surface plasmon-polariton (LSPP).[20,30] The LSPP can easily couple to propagating electromagnetic waves as its launching must only fulfil an energy conservation requirement that can be achieved by tuning the photon wavelength. This makes LSPPs a powerful and versatile tool that can be straightforwardly integrated into optical microscopy.

2.3.3 Localised surface plasmon-polaritons

Similarly to treating photons confined to dimensions comparable to their wavelengths as quantised cavity modes (as opposed to propagating waves), LSPPs occur at discrete values of ω. For nanoparticle dimensions significantly smaller than the wavelength of light in the surrounding medium, we can assume that the phase of the light wave is constant across the nanoparticle and use an uniform electrostatic description of the system. For the simplest geometry, a sphere, the analytical form of the polarizability, α, is given by the permittivity of the metal, ε_m, and the surrounding dielectric, ε_d, and the sphere radius, a:

$$\alpha(\omega) = 4\pi a^3 \frac{\varepsilon_m(\omega) - \varepsilon_d}{\varepsilon_m(\omega) + 2\varepsilon_d} \qquad (2.6)$$

The induced polarisation, $\boldsymbol{p}$, in an electromagnetic field, $\boldsymbol{E}_0$, is then given as:

$$\boldsymbol{p} = \varepsilon_d \varepsilon_0 \alpha \boldsymbol{E}_0$$

(2.7)

The strongest response occurs for minimal denominator of α when Re(ε_m) = -2ε_d, which is known as the Fröhlich resonance condition[37] and the resulting LSPP mode has a dipolar nature. Note that similarly to the SPPs, the resonance frequency depends on the dielectric permittivity of both, the metal and the surrounding dielectric.

For larger particles, the uniform electrostatic field approximation is no longer valid and electrodynamic treatment using Mie theory gives LSPP modes as a spherical harmonic series.[20,38] The expression for the polarizability, α, is more complex introducing additional dependence of the resonance energy on the nanoparticle size. Specifically, increasing nanoparticle size red shifts the resonance, which can be understood in terms of a decrease in restoring force due to larger charge separations in larger particles. Note that the same is true for elongated nanoparticles where the LSPP mode along the long axis is redshifted with respect to the transverse resonance. In other words, light polarised along the long axis of elongated nanoparticles will drive the redshifted LSPP and vice versa.[39]

The size-dependence is often exploited experimentally to tune the LSPP resonance to the illumination or a molecule of interest. We also employ it in this thesis in chapter 3 where we sweep the resonance of gold nanorods across the electronic transition of the photosynthetic complex under study by varying the nanorod lengths and in chapter 5, in which we tune the resonance of gold plasmonic nanojunctions by varying the size of the constituent nanoparticles. The conceptual visualisation of LSPPs and the size and shape dependence of the resonances are summarised in Figure 2.3.

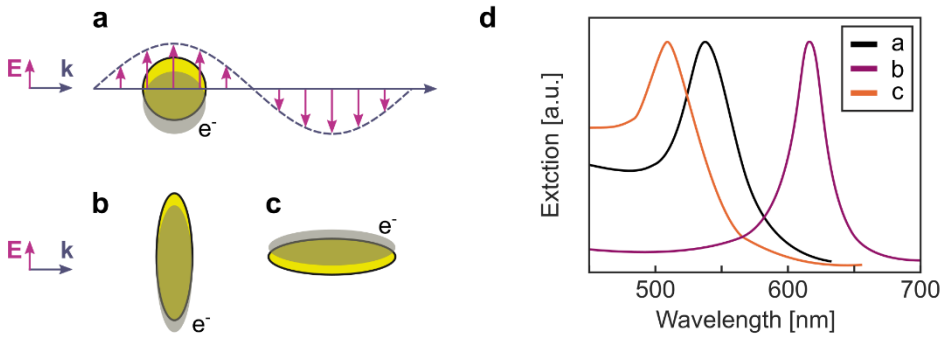

Figure 2.3 ***Localised surface plasmon-polaritons in gold nanoparticles****. a) Schematic representation of a light wave propagating along the wavevector,* ***k****, with electric field oscillating along* ***E*** *inducing a plasmonic response in a spherical gold nanoparticle. The negative refractive index of gold manifests as out of phase oscillations of conduction electrons marked in grey. b,c) Same as a) but for an elongated nanoparticle showing oscillations along and perpendicular to the long nanoparticle axis. d) Extinction spectra for nanoparticles in a-c) showing enhanced optical scattering at the LSSP resonance that scales with the nanoparticle size and shape. The spectra are adapted from ref.* [39]

So far, we described the dipolar LSPP mode under electrostatic and electrodynamic treatment. The latter approach also gives rise to higher order modes, such as quadrupoles that are blueshifted with respect to the dipole resonance. The quadrupole modes are often referred to as "dark", because their symmetry results in negative interference of the induced LSPP electric field with the incoming radiation. The electrons in the metal however do not respond to the incoming field instantaneously, introducing a small phase shift between the electromagnetic wave and the electron response called the retardation effect. Thus, in nanoarchitectures with high retardation, higher order modes can couple moderately to travelling electromagnetic waves. For example, in chapter 5, we observe increased coupling of quadrupolar modes to the far field upon changing the refractive index of the environment surrounding the gold nanostructure, which has been attributed to increased retardation with respect to air.[40]

Having outlined the light-coupling and resonance conditions of the discrete modes of LSPP in metallic nanostructures, we can discuss the optical properties of the nanoparticles under illumination. The total optical response is characterised by the extinction cross-section, $\sigma_{ext}(\omega)$, defined as a sum of absorption and scattering cross sections, $\sigma_{ext}(\omega) = \sigma_{abs}(\omega) + \sigma_{scat}(\omega)$. As the underlying mathematical expressions within the electrodynamic treatment are unnecessarily complicated for the background required for this thesis, we briefly return to the uniform electrostatic approximation. The absorption and scattering cross-sections for a spherical particle can be written as:

$$\sigma_{sca}(\omega) = \frac{k^4}{6\pi}|\alpha(\omega)|^2$$

(2.8)

$$\sigma_{abs}(\omega) = k\, Im(\alpha(\omega))$$

(2.9)

where k is the wavevector $k = 2\pi/\lambda$. Recall that $\alpha(\omega) \propto a^3$ and thus for small nanoparticle radii, a, the optical response is dominated by absorption whereas the faster scaling of scattering with size makes the process dominate in large nanoparticles. This size-dependent dominance of either absorption or scattering predicted within the uniform static field approximation is also observed experimentally.[41]

Aside from the optical properties of the nanoparticles themselves, the LSPP modes also influence the electric field in the surrounding medium. For a small sphere, the oscillations of the conduction electrons induced by the driving optical field can be approximated as a point dipole at the centre of the sphere that in turn induces electric field in the surrounding medium.[20,38] An analytical expression within the electrostatic approximation yields a non-propagating electric field decaying with distance, r, as $1/r^3$ which is characteristic for an electric dipole.[20] When time variation is added, a term proportional to $1/r$ appears, again typical for a dipole radiation that propagates into the far field. The point dipole approximation breaks for larger spheres and complex geometries and numerical calculations based on Maxwell's equations are commonly employed to determine the electric field distribution within and around more complicated nanoparticles. We also employ this strategy to find resonance energies of plasmonic nanostructures employed in chapter 5.

Importantly, the induced electric field varies across very short distances ($1/r^3$) creating local hotspots that can reach intensities several orders of magnitude higher than the incident radiation.[42] For example, strong fields are often induced on tips of nanoparticles due to a lightning rod effect.[43] Given that the nanoparticles are already smaller than the incident wavelength, the resulting hotspots are significantly smaller than the diffraction limit.[44] As such, metallic nanoparticles can serve as local probes of the surrounding dielectric medium, bridging the gap between the micro scale of the optical microscopy and the nano scale of single molecules. Below, we outline how plasmonic nanoparticles can be used to investigate single to few molecules at a time and how the intrinsic molecular

properties change inside the plasmonic hotspot in the context of fluorescence and Raman scattering.

2.3.4 Molecule-nanoantenna interactions

At resonance, the extinction cross-section of metallic nanoparticles can reach values thousand times larger than their geometrical cross-section. To highlight this efficient interaction with optical radiation, metallic nanoparticles are often referred to as nanoantennas. The interaction of molecules in nanoantenna hotspots with the far-field radiation is fully-mediated by the nanoantenna,[45] thus greatly enhancing the optical response of molecules.

Recall that fluorescence involves an absorption of a photon that electronically excites a molecule, followed by fast rearrangement of the atoms in the excited state and a subsequent emission of a slightly redshifted photon that brings the molecule back into its electronic ground state. Under linear illumination, fluorescence intensity, I_{FL}, is proportional[18] to the laser intensity, I_{las}, the molecular absorption cross-section, σ_{abs}, and the fluorescence quantum yield, Φ_{FL}:

$$I_{FL} = I_{las}\sigma_{abs}\Phi_{FL} \tag{2.10}$$

The fluorescence quantum yield defines the probability that an excited state decays radiatively and is defined by the radiative, k_r, and non-radiative, k_{nr}, decay rates from the excited state of the emitter as:

$$\Phi_{FL} = \frac{k_r}{k_r + k_{nr}} \tag{2.11}$$

In a proximity of a nanoantenna, the total fluorescence enhancement[20,30] is a product of the absorption enhancement and fluorescence quantum yield enhancement:

$$M_{FL} = M_{abs} \cdot M_{\Phi_{FL}} \tag{2.12}$$

The absorption enhancement stems from the increased electric field experienced by the molecule in a plasmonic hotspot and is equal to the local electric field enhancement, M_{loc}, scaled by a dipole-dipole coupling coefficient, T_{abs}:

$$M_{abs}(\omega, \boldsymbol{r}, \phi) = M_{loc}(\omega, \boldsymbol{r})\, T_{abs}(\phi)$$

(2.13)

The scaling factor, T_{abs}, depends on the mutual orientation of the electric dipole of the molecule and the local field polarisation, given by their unit vectors $\boldsymbol{e}_m$ and $\boldsymbol{e}_{loc}$, respectively: $T_{abs}(\phi) = |\boldsymbol{e}_m \cdot \boldsymbol{e}_{loc}|^2$. The antenna-molecule interaction is strongest when $\boldsymbol{e}_m$ and $\boldsymbol{e}_{loc}$ are parallel and zero when they are orthogonal. The local electric field enhancement is defined as:

$$M_{loc}(\omega, \boldsymbol{r}) = |\boldsymbol{E}_{loc}(\omega, \boldsymbol{r})|^2 / |E_0|^2$$

(2.14)

where $\boldsymbol{E}_{loc}$ is the local electric field dependent on the frequency of light and position and E_0 is the amplitude of the reference electric field without the nanoantenna. Maximum local field enhancement is achieved at light frequency resonant with an LSPP mode (yielding the strongest optical properties) at the position of highest electric field intensity within the plasmonic hotspot.

The fluorescence quantum yield enhancement occurs via increasing the local density of states into which the excited state of the molecule can decay, thereby modifying the radiative and non-radiative decay rates as $M_r = k_r / k_{r,0}$ and $M_{nr} = k_{nr} / k_{nr,0}$, respectively.[20,30,46] Similarly to M_{abs}, fluorescence quantum yield enhancement is defined as a ratio of the quantum yield with and without the nanoantenna. Expressing Φ_{FL} in terms of the excited state decay rates yields:

$$M_{\Phi_{FL}} = \frac{\Phi_{FL}}{\Phi_{FL,0}} = \frac{M_r\left(k_{r,0} + k_{nr,0}\right)}{M_r\, k_{r,0} + M_{nr}\, k_{nr,0}}$$

(2.15)

Maximising $M_{\Phi_{FL}}$ is more complicated than for the absorption enhancement because it involves increasing the radiative decay rate, while trying to leave the non-radiative counterpart unmodified.[18,20,30] The highest M_r is achieved by coupling of the molecule to radiative LSPP modes that is generally the lowest energy dipolar mode. Contrary, M_{nr} increases when the molecule couples to non-radiative modes, typically higher-order modes such as the quadrupole. As higher-order modes have smaller spatial extent, there is an optimal molecule-antenna separation, typically ~ 5-10 nm, which gives rise to the maximum overall fluorescence enhancement. Below this separation, non-radiative decay dominates quenching the fluorescence emission and above, the molecule-nanoantenna coupling decreases.[18,47,48] The non-radiative enhancement ultimately limits maximum possible fluorescence

enhancements to 1-2 orders of magnitude. A more precise uncoupling of radiative and non-radiative enhancement is extremely challenging, but not necessarily relevant as the fluorescence quenching at short distances is the most common limiting factor of $M_{\Phi_{FL}}$.[48–50] Note that the modest fluorescence enhancement factors allow their relatively straightforward experimental determination by measuring the fluorescence of a single molecule on and off a nanoantenna.

Finally, it is implicit that the LSPP dipole resonance of the antenna should match the electronic resonance of the molecule to maximise the overall fluorescence enhancement. We have shown above how LSPP resonance depends on the dielectric permittivity of the material (gold or silver), the nanoparticle shape and size. One of the most convenient nanoantenna geometries for a systematic resonance tuning is a nanorod whose dipole resonance along the long axis scales linearly with its length.[51] We employ this strategy experimentally in chapter 3.

Let us now consider Raman scattering of molecules next to metallic nanoantennas called the surface-enhanced Raman scattering (SERS). Recall that Raman scattering is a single-step process where an incoming photon loses or gains energy by coupling to molecular vibrations. There are two underlying mechanisms that yield the overall SERS enhancement: a dominant "plasmonic" contribution and a much weaker "chemical" enhancement.

The former mechanism relies on the increased electric field intensity inside the nanoantenna hotspot "experienced" by the molecule. We have already defined this local field enhancement for fluorescence as the ratio of the electric field intensity with and without a nanoantenna, $M_{loc} = |\boldsymbol{E}_{loc}(\omega, \boldsymbol{r})|^2/|E_0|^2$. Thanks to the optical reciprocity theorem (ORT), we can consider the out-coupling enhancement of the scattered photons as equivalent to the reverse process: photons incoming in exactly opposite direction (towards the molecule), under the same polarisation as the scattered light. Therefore, the plasmonic SERS enhancement of a given vibrational mode of a molecule close to a nanoantenna can be written as:

$$M_{SERS} = M_{loc}(\omega_i)\, M_{loc,ORT}(\omega_r)\, T(\hat{\alpha}_N, \boldsymbol{e}_{loc}(\omega_i), \boldsymbol{e}_{loc,ORT}(\omega_r)) \quad (2.16)$$

where M_{loc} is the local field enhancement at the incident frequency, ω_i, $M_{loc,ORT}$ is the local field enhancement at the frequency of the scattered light, ω_r, and T is a scaling factor that encodes the enhancement dependence on the orientation of the vibrational mode with respect to the nanoantenna.

T depends on the symmetry of the Raman mode given by the normalised Raman polarizability tensor, $\hat{\alpha}_N$ and, $\boldsymbol{e}_{loc}(\omega_i)$ and $\boldsymbol{e}_{loc,ORT}(\omega_r)$ the electric field unit vectors at the molecular position along the incident and scattering directions, respectively. Unless the scaling factor T tends to zero (for very specific molecular orientations), it can be neglected as the main contribution to the SERS enhancement stems from the local electric fields. T is mainly useful to explain variation of intensity among different Raman bands and is therefore called the surface selection rule factor.[20]

In practice, the LSPP resonances giving rise to the SERS enhancement tend to be spectrally broader than the Raman fingerprint region. Therefore, the frequency difference between the incident and scattered light is often neglected and the plasmonic SERS enhancement factor, M_{SERS}, is approximated as:

$$M_{SERS} \approx M_{loc}(\omega, \boldsymbol{r})^2 = |\boldsymbol{E}_{loc}(\omega, \boldsymbol{r})|^4 / |E_0|^4 \quad (2.17)$$

Typical plasmonic enhancements range up to 10^{10}. In contrast, the weaker chemical mechanism yields only up to 10^2 enhancement. This additional contribution stems from a formation of charge-transfer states of molecules adsorbed to the surface of the metal and the resulting change in the Raman polarizability tensor. Note that this change can yield both lower and higher SERS intensity.[20]

Overall SERS enhancements of > 10^{10} have been reported in literature and enabled SERS measurements down to a single-molecule level.[52,53] Note that unlike in fluorescence, precise experimental determination of SERS enhancement factors and decoupling of the plasmonic and chemical contribution are challenging as a single-molecule Raman scattering reference cannot be measured. Yet, it is quite remarkable that the initial 11-15 orders of magnitude difference between fluorescence and Raman scattering molecular cross-sections was successfully bridged via enhancement by metallic nanoantennas. As such, both SM fluorescence and Raman scattering make part of the available experimental toolkit to probe systems at their most fundamental nanoscale level.

To summarise the theoretical background of this thesis, single-molecule microscopy uncovers physical phenomena beyond the observables averaged over an ensemble of molecules. Molecular signatures shifted from the illumination wavelength enormously facilitate single-molecule detection by allowing spectral filtering of the overwhelming background from the incident light. Two processes are typically studied: fluorescence and Raman scattering. The former is a multi-step process

involving an absorption and emission of a photon whereas the latter is an instantaneous inelastic scattering. Both processes can be can be enhanced using metallic nanoantennas. Laser wavelength, nanoantenna material, size and shape and antenna-molecule distance and orientation dictate the strength of the coupling between the antenna and the molecule. Both in- and out-coupling of photons can be enhanced. In fluorescence, competing enhancement of the radiative and non-radiative decay of the excited state limit the achievable enhancement factors to 1-2 orders of magnitude. Conversely, the 4^{th} power dependence on local electric field of SERS enhancements yields SERS enhancements of over 10 orders of magnitude, bridging the gap between the molecular fluorescence and Raman cross-sections, ultimately enabling single-molecule SERS experiments.

3 Energy Transfer in Single Enhanced Photosynthetic Complexes

Over millions of years, energy transfer during photosynthesis was optimised to almost unity efficiency. Despite decades of investigation, the structure-function relationship of the molecules that form the photosynthetic chain is not yet fully understood. In this chapter, we investigate excitation energy transfer in one of the most studied photosynthetic building blocks, the Fenna-Matthews-Olson complex. To gain fundamental insight into the energy transfer within the complex, we combine plasmonic nanoantennas and a home-built confocal cryomicroscope that allow us to detect Fenna-Matthews-Olson complexes at a single-complex level, for the first time at room temperature and 77 K. By recording fluorescence photon statistics that inform on energy transfer within the complex, we show that the entire system, which contains 24 pigment molecules, behaves as a single quantum emitter. Furthermore, we show that the plasmonic enhancement can be used to tune the fluorescence photon statistics of the complex, making it appear as multiple independent emitters when energy transfer to the nanoantenna occurs on timescales comparable to that between the pigments within the complex. These results provide new fundamental insights into the energy transfer between individual pigments of the Fenna-Matthews-Olson complex suggesting that excitation annihilations that give rise to the single-emitter character play a regulatory role in photosynthesis.

3.1 Introduction

3.1.1 Principles of photosynthesis

Photosynthesis is the process of using light to power conversion of carbon dioxide and water into sugars as a form of chemical energy storage. It is the reverse of cellular respiration cycle that produces water and carbon dioxide by burning sugars. As such, photosynthesis prevents all life from eventually turning into carbonated water. The process starts with harvesting a photon, whose energy is funnelled to a reaction centre where it fuels a charge separation converting the electronic excitation into chemical redox energy. The separated charges then drive a sugar synthesis reaction resulting in a long-term chemical energy storage.[54]

The energy transfer to the reaction centre occurs with almost unity quantum efficiency.[55] This sparked a strong fundamental interest into how, over the course of billions of years of evolution, nature optimised the molecular machinery of photosynthesis for light harvesting. Understanding this process all the way down to the nanoscale is not only interesting fundamentally, but also crucial for better design of artificial photosynthetic devices and organic photovoltaics. These applications are ever more important in the pressing need to switch to clean sources of energy.

In the early stages of photosynthesis, photon absorption and energy transport to the reaction centre are facilitated by pigment-protein complexes that consist of light-sensitive chromophores embedded in a protein matrix. The first crystallographic structure of a chlorophyll-containing photosynthetic complex was measured in 1975 for the Fenna-Matthews-Olson (FMO) complex found in green sulphur bacteria.[56–58] In 1986, improved structure with a 1.9 Å resolution[59] provided a detailed insight into the arrangement of the photosynthetic pigments within the complex, allowing extensive support of experimental research by theoretical calculations. Therefore, FMO complex became a model system for energy transfer in photosynthesis.

Despite of almost 50 years of research efforts to understand energy transfer through the FMO complex, the specific pathway and the structure-function relationship have not been established unequivocally.[60] Below, we summarise the current scientific consensus on the mechanism of energy transfer via the FMO complex and outline how single-molecule experiments can address some of the fundamental nanoscale questions that remain unsolved.

3.1.2 Excitation energy transfer within FMO monomers

The function of the FMO complex in photosynthesis is to channel excitation energy from a light-harvesting antenna, chlorosome, into the reaction centre where charge separation takes place.[54,61] The FMO complex consists of three identical monomers arranged in a C_3 symmetry (Figure 3.1).[62] Each monomer contains 7 closely spaced bacteriochlorophyll *a* (BChl *a*) pigments surrounded by a protein matrix. An additional 8th BChl *a* molecule occupies the intermonomer space facing the cholorosome giving a total of 24 BChls *a* per FMO trimer.

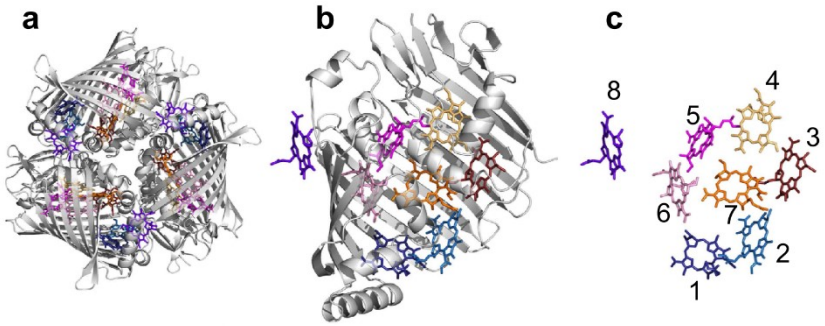

Figure 3.1 ***Structure of the FMO pigment-protein complex****. a) C_3 arrangement of the monomer subunits, b) FMO monomer showing 8 BChls a embedded in a protein matrix and c) relative orientation of the 8 BChls a inside one monomer and the BChl numbering used throughout this work. The phytyl tails of the BChls are not shown for clarity. Adapted from ref.*[63]

The BChls *a* inside the FMO monomer are chemically identical, however, each chromophore is bound to a different part of the protein matrix. This protein scaffold slightly modifies the electronic transition energies of the individual pigments, redshifting BChls close to the reaction centre with respect to those facing the chlorosome antenna. As such, the FMO complex acts as a directional energy funnel.

The individual site energies of BChls *a* lie very close to each other and cannot be distinguished spectroscopically. At room temperature, the Qy absorption band of FMO consist of one broad peak at 805 nm (Figure 3.2), slightly redshifted from the absorption maximum of free BChl *a* at 780 nm.[64] This band splits partially at low temperature, but only into 3-4 bands and hence the site energies of all 8 BChls *a* must be determined using simulations from the crystallographic data in combination with benchmarking against the optical spectra.

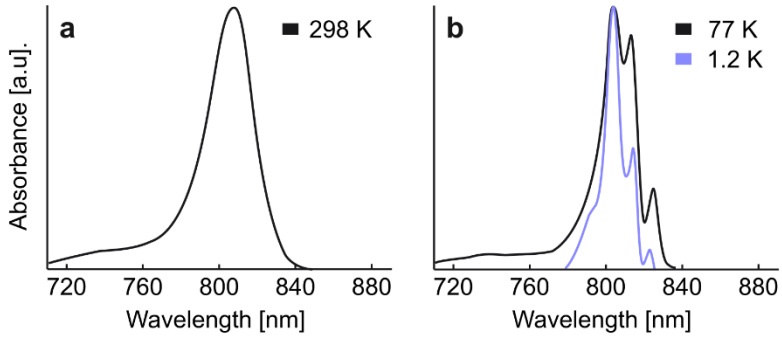

Figure 3.2 ***FMO complex spectra****. a) Room temperature absorption spectrum showing a broad band at 805 nm. b) Absorption spectrum at 77 K and fluorescence excitation spectrum at 1.2 K showing 3 and 4 distinct bands, respectively. The absorption and fluorescence excitation spectra were taken from ref*[82] *and ref,*[63] *respectively.*

Even today, it is not entirely known how excitation energy travels along the FMO monomer.[65–68] Do the 8 BChls *a* operate independently or are they organised into a transport chain as suggested by their gradual redshift and if so, what are the energy transfer pathways? Or could they be all electronically coupled together to form a new quantum state upon photoexcitation? The latter mechanism was proposed based on a 2-dimensional electronic spectroscopy experiment that was interpreted as evidence of a quantum coherent energy transfer across the FMO monomer where the energy was delocalised across the BChl *a* pigments.[65] This sparked intensive research into the role of electronic coupling between the individual pigments in the high efficiency of energy transfer to the reaction centre. Although this wave-like energy transport across has been later experimentally refuted,[66] some weak energy delocalisation over few BChls *a* within the monomer does seem to take place.[69,70]

The current consensus on excitation energy transfer (EET) in the FMO monomer obtained through the synergy of optical and theoretical research can be summarised as follows. Multiple BChls *a* were proposed as entry points for the excitation energy, namely the higher energy BChls 1, 6 and BChl 8 for its proximity to the light-harvesting antenna.[71–73] The subsequent energy pathways are not yet understood, but there is a consensus that the energy is funnelled to the lowest energy site located primarily on the BChl 3 pigment with a minor contribution of BChl 4 (12 %).[69,70] The intramonomer EET onto BChl 3 is very fast with a sub-picosecond lifetime,[74] facilitated by short distances of 4-11 Å[62] between the individual BChls *a* within the monomer. This pigment arrangement also gives rise to weak to an intermediate coupling between the BChls *a* calculated to be ~ 10-60 cm^{-1}.[69]

3.1.3 Intermonomer excitation energy transfer

After the energy reaches BChl 3, it is funnelled along the photosynthetic chain. However, a question remains whether each FMO monomer operates individually, or whether they are coupled and the entire trimer functions as a single unit. There is ample indirect evidence of the latter case.[60] Firstly, the distances between symmetry-related BChls of different monomers are 25-46 Å[62] and based on the Förster theory, a weak dipole-dipole electronic coupling of a few wavenumbers could be present.[75] Secondly, a 825 nm band in non-resonant hole-burning spectra has been successfully modelled by including a downward EET among the lowest energy sites of the three monomers.[76,77] Lastly, 2D electron spectroscopy revealed a decay component with lifetime of 29 ps consistent with expected timescale of Förster resonance energy transfer between the monomers.[73] Consistent with this finding, singlet-singlet annihilation studies[78]s found a 26 ps decay component assigned by computational modelling to incoherent energy thermalisation among the FMO monomers.[60]

Despite all this indirect evidence, intermonomer EET is far from generally accepted as evidenced for example by computational studies of EET in FMO considering only the monomer subunit of the FMO complex.[79,80] Therefore, an experiment addressing the intermonomer EET directly is needed to unequivocally verify whether the three subunits of FMO complex are coupled and intermonomer energy transfer plays a role in the photosynthetic process of green bacteria.

The spectroscopic studies on FMO to date relied mostly on transient absorption and fluorescence. The former technique was able to track ultrafast phenomena down to 200 fs.[81] However, due to the sensitivity of transient absorption to radiative and non-radiative processes of both ground and excited states and the complex nature of the FMO system, the resulting data can be difficult to interpret. Namely, finding a kinetic model that correctly assigns observed decays to underlying processes is not straightforward. Therefore, time-resolved fluorescence can be advantageous as it yields the decay lifetime of the excited state only, which is easier to interpret. A biexponential fluorescence decay of the FMO complex with constants of 60-260 ps and 900-1500 ps was found at 77 K[81,82] where the short component was assigned to a quenching pathway by a cysteine residue[83] on the protein scaffolding and the longer lifetime to the native decay of BChl *a* in FMO. With increasing temperature, the fast pathway becomes more prominent.[82,83]

The main energy transfer steps in an FMO complex are summarised in Figure 3.3. The sub-picosecond energy relaxation towards BChl 3 (blue) can be followed by a Förster resonance energy transfer (FRET) between the monomers (green) and

eventually, the energy is transferred via the cysteine-mediated quenching pathway (orange) or the inherent decay pathway of the FMO complex (pink).

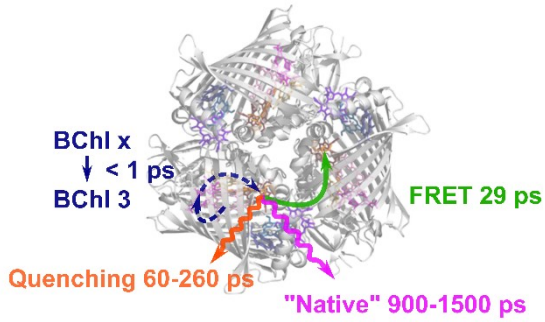

Figure 3.3 ***Schematic representation of energy transfer in an FMO trimer****. Ultrafast excitation energy transfer onto BChl 3 (blue) and possible subsequent pathways: Förster resonant energy transfer (FRET) between monomers (green), quenching by a cysteine residue (orange) and native BChl a energy transfer (pink). The FMO complex structure is taken from Ref.*[63]

3.1.4 Single-molecule photon statistics as a probe of excitation energy transfer between FMO monomers

All of the experiments mentioned above examined bulk FMO samples. As we outlined in section 2.1, bulk experiments probe averaged properties over millions of molecules at a time. In contrast, single-molecule measurements offer a much deeper insight thanks to their sensitivity to different molecular conformations and variations of the local environment. In the case of FMO, the single-molecule approach offers two additional advantages.

Firstly, probing each trimer separately removes any contribution from energy transfer between different FMO complexes, yielding a direct insight into the energy transfer within the fundamental building block of photosynthetic energy transfer. Note that avoiding interactions of multiple FMO trimers could also be achieved by bulk spectroscopy under low FMO complex concentration, in other words, observing multiple non-interacting complexes at a time. More importantly, studying the FMO complex at a single-trimer level unlocks new insights that cannot be obtained by bulk measurements. Specifically, photon statistics of fluorescence emission from a diffraction-limited spot reveal the number of independent quantum emitters in the spot through a measurement called fluorescence antibunching.[84] The method is described in detail in section 3.2.4, but briefly, fluorescence photons are split between two identical detectors, each recording individual fluorescence photons as well as their arrival time. A single quantum emitter emits only one photon at a time and thus the detectors do not record any photons at zero-time delay. More generally, the probability of recording multiple photons at the same

time scales with the number of emitters in the focal spot. Therefore, recording fluorescence photon statistics on single FMO trimers can directly experimentally verify whether they act at a single emitter (and by extension prove the presence of coupling between the monomers), three emitters (uncoupled monomers), or even 24 emitters which is unlikely, but theoretically possible as there are 24 BChl *a* pigments in each FMO trimer.

Recall that the main two experimental challenges of single-molecule fluorescence are low emission intensity and limited number of photons prior to irreversible photobleaching (section 2.1). This issue is exacerbated by the evolutionary optimisation of the FMO complex to maximise non-radiative energy transfer along the photosynthetic chain. Whereas the typical fluorescence quantum yield, Φ_{FL}, of fluorescent dyes is > 90 %, for free BChl *a* it is only 18 %,[85] which decreases even more when the pigments are embedded in a protein matrix of the FMO complex, all the way down to 2 %.[82] Therefore, we will employ two strategies that will allow us to probe the FMO complex fluorescence at a single-molecule level: fluorescence enhancement by plasmonic nanonatennas and a fluorescence "stabilisation" by cryogenic conditions.

The plasmonic enhancement of fluorescence consists of increasing Φ_{FL} and photon absorption and is strongest when the plasmon resonance of the nanoantenna matches the electronic resonance of the molecule (section 2.3.4). Note that experimentally, resonant plasmonic nanoantennas have also been shown to increase the total number of fluorescent photons emitted by a molecule, the photon budget.[86]

The fluorescence quantum yield enhancement occurs via modifications of the radiative and non-radiative decay rates from the excited state (section 2.3.4). However, the intrinsic dynamics between the monomers of FMO should remain unchanged as the plasmonic enhancement across the entire trimer is expected to be uniform based on a much larger size of the nanorod hotspot (~ 50 nm based on numerical simulations) compared to the FMO trimer (< 4 nm based on its weight of 142 kDa).[87] In fact, there is experimental evidence that plasmonic nanoantennas do preserve intrinsic coupling between pigments in a similar system, light-harvesting complex 2. It contains 9 weakly and 18 intermediately-coupled BChls *a* arranged in two concentric rings of 6.8 and 3.6 nm diameter, respectively,[88] and both native and plasmonically-enhanced single-molecule fluorescence studies yielded similar emission statistics.[89,90] Therefore, gold nanorods should be suitable to enhance single-FMO trimer fluorescence without influencing its intermonomer dynamics.

Further improvement in fluorescence can be gained by conducting experiments in vacuum, with an additional possibility to decrease the temperature by using a cryostat. Firstly, the vacuum removes molecular oxygen that is an efficient fluorescence quencher[24] and thus increases the overall photon budget. Furthermore, cooling the sample down increases the fluorescence quantum yield and photon budget by lowering the probability of vibrationally-mediated decay transitions and improves the fluorescence signal to background ratio through spectral narrowing of the absorption spectrum that leads to improved overlap of excitation laser with the electronic transition (more details in section 3.3.4).[91] In fact, the only single-molecule study of FMO published to date used cryogenic conditions at the liquid helium temperature of 1.2 K.[63] As this temperature is not biologically relevant, we focus on room temperature measurements under vacuum and extend our dataset by additional experiments at 77 K that allow a more complete characterisation on the single-molecule photon statistics of FMO.

In summary, the energy transfer during photosynthesis is mediated by pigment-protein complexes. One of the most studied systems is the FMO complex formed by three identical monomers each containing 8 pigments. To date, it is unclear how the excitation energy from light travels across the FMO trimer and whether the individual monomers are coupled, or operate as independent subunits. Here, we employ single-molecule fluorescence photon statistics on single FMO trimers to directly probe the number of independent quantum emitters in a focal spot and thus experimentally determine whether the FMO trimer functions as a single, or multiple separate systems. Since the fluorescence quantum yield of the FMO complex is extremely low at only 2 %, we employ plasmonic nanorod antennas for fluorescence enhancement and a cryostat to prevent fluorescence photobleaching by molecular oxygen. For some measurements, we lower the temperature of the system to provide additional fluorescence increase by improving overlap of the molecular absorption with the excitation laser and decreasing the probability of non-radiative decay. Thanks to the plasmonic enhancement and fluorescence stabilisation, we manage to detect single FMO trimers and record sufficient photon statistics to determine that the trimer can operate as a single quantum emitter.

3.2 Methods

3.2.1 Plasmonic nanorods

The plasmonic enhancement of FMO fluorescence was provided by gold nanorod dipole antennas produced by nanolithography. This technique uses a combination of gold evaporation and electron beam lithography that utilises electrons to create nanopatterns with resolution down to 10 nm.[92] The main advantage of the technique lies in its ability to produce large arrays of mutually-aligned nanorods with the possibility of systematic sweeps of geometric parameters such as the nanorod length. Since the resonance wavelength of the plasmon mode along the long axis of the nanorod scales linearly with their length,[51] this approach enables probing single-molecule fluorescence as a function of systematically tuned molecule-nanorod resonance overlap. The arrays of gold nanorods used in this work were fabricated by Johann Osmond at ICFO. The width and height of the nanorods was kept constant at 50 nm and the length was varied from 90 to 180 nm in steps of 10 nm to scan across the 805-825 nm range of FMO absorption and fluorescence (section 3.3.1). The nanorods were deposited directly on top of a solid immersion lens (SIL) to increase the effective numerical aperture of the microscope (Figure 3.4).

3.2.2 Sample preparation

FMO complexes from *Chlorobaculum tepidum* were kindly provided by the Blankenship group and purified as described elsewhere.[62,82] FMO solution was diluted in a pH 10.5 CAPS buffer (20 mM) or sodium carbonate/bicarbonate (100 mM) buffer, Triton X-100 detergent (0.1 % v/v) and polyvinyl alcohol (0.8 % v/v; Mowiol 20–98, Mw 125 kDa). Bulk FMO measurements were conducted with ~ 300 nM FMO solution referred to as “high concentration” and for single-molecule experiments ≤ 3 nM, ‘’low concentration” was used. The solution was spin coated on the nanopatterned SIL at 2000 rpm for 30 s (G3P-8, Specialty Coating Systems) producing films of ~ 30 nm thickness as measured by a profilometer (Alpha-Step IQ). This yielded on average ≤ 0.03 FMO trimers per a diffraction limited spot (966 nm diameter).

3.2.3 Time-resolved confocal cryomicroscope

The optical setup combines a confocal cryomicroscope used in a reflection geometry with time-correlated single photon counting (TCSPC) electronics (Figure 3.4). The sample was mounted inside a continuous flow cryostat (ST-500 Jannis) under vacuum at room temperature or 77 K. The excitation light was generated by a Ti:Sapphire laser (Octavius 85M, Menlo Systems) and linearly polarised along the

long axis of the nanorods. The spectral band of 805 ± 2 nm FWHM was selected (tunable 887 SP & tunable 887 LP, Semrock) to match the maximum in the FMO complex absorption spectrum measured by a commercial spectrometer (Lambda 950, Perkin Elmer).

The excitation beam was focused by a 0.5 NA air objective (LMPLFL50x, Olympus) placed outside the cryostat, onto a half-ball SIL inside the cryostat. The refractive index of the SIL glass was $n = 2$, increasing the effective NA of the objective according to the relationship $NA_{eff} = n\,NA_{obj}$[93,94] to $NA_{eff} = 1$. Hence the excitation beam at 805 nm was focused to a diffraction-limited spot with a 966 nm diameter at the sample.

To locate single FMO trimers, the air-piece of the objective was scanned over the sample by a 3D piezo stage (Nano F3D, Mad City Labs). FMO complex fluorescence at 810+ nm (2x 808 LP, Semrock) was detected through the same objective using single-photon avalanche diodes (SPADs), pre-processed by a fast electronics system ADwin (ADwin Gold II, Jäger GmbH) and stored in a personal computer. Two-photon photoluminescence of the nanorod arrays was detected at 770- nm (770 SP & tunable 790 SP, Semrock).

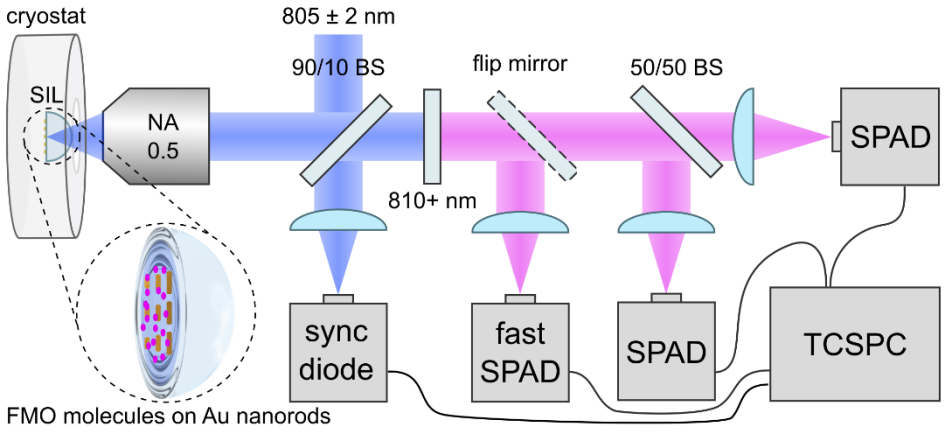

Figure 3.4 ***Confocal cryomicroscope in a reflection geometry used to measure single FMO trimer photon statistics.*** *The inset shows nanopatterned SIL with a spin-coated polyvinyl alcohol film (blue) containing FMO complexes (pink). The fluorescence signal is recorded by SPADs. The fast SPAD and two identical sensitive SPADs are used for lifetime and antibunching measurements, respectively.*

3.2.4 Fluorescence antibunching measurement

Fluorescence was split by a 50/50 beam splitter onto two identical sensitive SPADs (SPCM-AQRH series, Excellitas) in a Hanbury Brown–Twiss configuration. The counts and the arrival time of the fluorescence photons were recorded with respect to the

beginning of the measurement by a time-correlated single photon counting TCSPC module (PicoHarp 300, PicoQuant). The second order correlation function, $g^2(t)$, of the photon counts at each detector with respect to the arrival delay between the two detectors, t, was determined (QuCoa software, PicoQuant).

In a pulsed excitation measurement, $g^2(t)$ takes form of peaks spaced by the laser pulse period. For a single emitter, at most one photon can be emitted at a time. Thus, the peak at zero time delay must be zero and we say that the fluorescence photons antibunch. In general, the second order correlation function at zero time delay is normalised to the average value of non-zero delay peaks. Such normalised $g^2(t=0)$ depends on the number of independent emitters, N, as:

$$g^2(t=0) = 1 - 1/N \qquad (3.1)$$

For two emitters, $N = 2$, the second order correlation function would be $g^2(t=0) = 0.5$, and thus any $g^2(t=0)$ value below 0.5 is considered a signature of fewer than two emitters, in other words, a single quantum emitter.

Note that fitting the slope of the $g^2(t)$ peaks would yield the excited state lifetime equivalently to the lifetime measurement described above. The reason we split the lifetime and photon statistics measurements is the trade-off between the detectors' efficiency and timing. To measure short lifetimes of tens of picoseconds, a fast detector is required (instrument response function of 52 ps). For the antibunching measurements, the minimum required time resolution is given by the laser pulse period of 12 ns and is not a limiting factor. The critical aspect of the detector is the quantum efficiency because the quantity of interest is a second order correlation function of the two detectors. The SPADS used for antibunching offer ~ 5 times higher quantum efficiency than the fast SPAD, which translates into 25 times shorter measurement time to obtain equivalent information. Since irreversible photobleaching is the main limitation of single-molecule experiments, long measurement times are not possible and the slow but efficient SPAD is crucial to measure the fluorescence antibunching.

3.2.5 Excited state lifetime measurement

Fluorescence was detected by a fast SPAD (PDM series, MPD) and a reference signal was detected by a sync diode (TDA 200, PicoQuant). The arrival of each fluorescence photon with respect to the reference pulse was recorded and histogrammed by the TCSPC electronics. The timing resolution of the lifetime measurement was given by the instrument response function of the fast SPAD detector: 52 ps at the FWHM. For

the measurement of the unenhanced FMO complex lifetime, we used a supercontinuum white light laser at 805 ± 2 nm (superK laser, NKT photonics) as the excitation source because the TCSPC histogram did not decay fully within the 12 ns pulse period of the Ti:Sapphire laser used in the measurements on the enhanced FMO complexes.

To yield the fluorescence lifetime of the excited state of the molecule in focus, The TCSPC histogram was fitted with a sum of exponentials,

$$\sum_i \alpha_i \exp(-t/\tau_i)$$

(3.2)

where α_i is the amplitude and τ_i is the excited state lifetime of the ith component. Both 77 K and room temperature histograms required three exponentials resulting in many fitting parameters. Therefore, we employed a variable projection algorithm that ensures a robust fit by allowing to analytically calculate the amplitude, α_i, for each lifetime, τ_i, obtained from a non-linear least-squares fit.[95] The proportion of the fluorescence photons of each component of the nth-exponential lifetime, the fractional contribution f_i, was calculated as:

$$f_i = \frac{\alpha_i \tau_i}{\sum_j^n \alpha_j \tau_j}$$

(3.3)

To facilitate comparison between measurements, we also calculated the average lifetime $\langle \tau \rangle$ as the sum of the individual exponentials, τ_i, weighted by their fractional contribution to the total number of photons in the histogram, f_i:

$$\langle \tau \rangle = \sum_i^n f_i \tau_i$$

(3.4)

3.3 Results and Discussion

3.3.1 Resonant fluorescence enhancement of FMO complex

The absorption and fluorescence maxima of the FMO complex lie at 805 and 825 nm, respectively.[68] In section 2.3.4, we outlined that the maximum overall fluorescence enhancement is expected for antenna resonances between the absorption and fluorescence maxima to yield simultaneously high absorption and fluorescence quantum yield enhancement.

To verify this prediction experimentally, we determined the nanorod resonances by recording two-photon photoluminescence (TPPL) at both the excitation (805 ± 2 nm at FWHM, Figure 3.5a) and emission wavelength (825 ± 2 nm at FWHM, Figure 3.5b). The advantage of TPPL is its sharp response due to its quadratic scaling with the near-field intensity at the hotspot and its background-free nature. To determine the overall fluorescence enhancement of the FMO complex, we spin coated a high concentration (300 µM) FMO solution onto the nanorod array and recorded confocal fluorescence scans at room temperature (Figure 3.5c).

A first glance at Figure 3.5 confirms a healthy behaviour of the antenna array as the strongest TPPL response shifts to longer antennas with increasing excitation wavelength. The maximum fluorescence is achieved for nanorod lengths resonant with the excitation and emission wavelengths. To quantify the enhancement, we averaged the nanorod response of multiple antenna arrays removing outliers such as the five extremely bright antennas in Figure 3.5a, b.

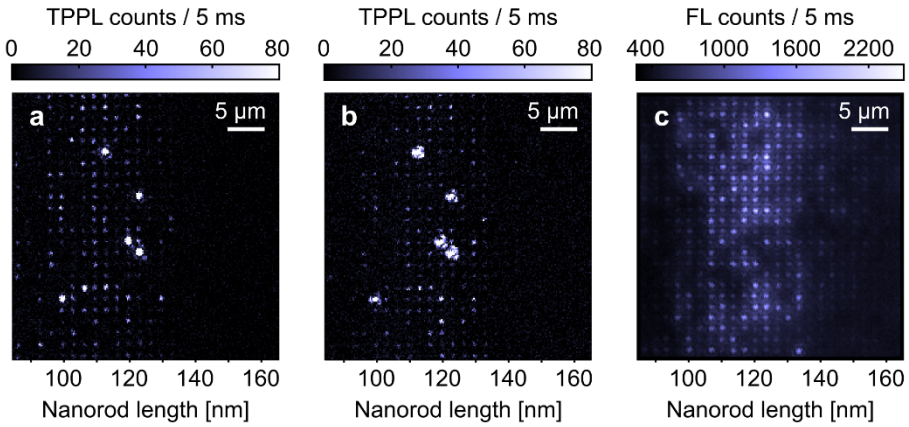

Figure 3.5 ***Resonant plasmonic enhancement of FMO trimers.*** *TPPL confocal scans of an antenna array with nanorod lengths of 90-160 nm excited at a) the FMO excitation wavelength (805 ± 2 nm) and b) FMO emission wavelength (825 ± 2 nm). c) Fluorescence confocal scan of FMO complexes spin coated on top of a nanorod array. The intensity bar was capped to show more nanorods.*

Figure 3.6 reveals the nanorod resonances averaged over 6 arrays sampling over 3000 nanorods. The absorption enhancement is maximised for 110 and 120 nm nanorods and the emission enhancement for slightly longer nanorods of 120 and 130 nm. In agreement with these results, the maximum fluorescence enhancement is reached at the overlap of the excitation and emission, at 120 nm nanorod length.

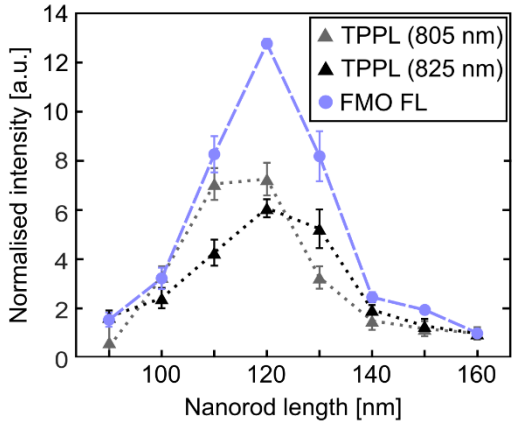

Figure 3.6 ***Gold nanorod resonances at excitation (805 nm) and emission (825 nm) maxima and overall fluorescence enhancement of the FMO complex****. Each point is averaged over 100+ nanorods and the error bars show the standard deviation. All data are normalised to the value for 160 nm nanorods.*

To quantify the fluorescence enhancement, we would ideally measure many single FMO complexes on and off nanorods and divide the corresponding fluorescence intensities, $M_{FL} = I_{FL}(nanorods)/I_{FL}(unenhanced)$. The unenhanced FMO complex is however beyond the sensitivity of our setup as the fluorescence quantum yield of the FMO complex is only 2 %.[82] Therefore, we define the lower threshold of the fluorescence enhancement, $M_{FL,lower} = I_{FL}/I_{FL}(160\ nm)$, where we normalise by the fluorescence intensity of FMO trimers on off-resonant 160 nm nanorods. This yields the minimum resonant fluorescence enhancement of 13.

3.3.2 Fluorescence of single FMO trimers and its fragments at room temperature

Having quantified the lower bound of the fluorescence enhancement from nanorod length-dependent fluorescence of many FMO complexes, we move on to detecting single trimers. We spin coated a low concentration FMO stock solution that should yield sparsely distributed single FMO trimers (section 3.2.2) and recorded 2D confocal scans of the sample (Figure 3.7a,c).

Recall that one FMO trimer consists of three monomers each containing 8 pigments that can all theoretically fluoresce. Therefore, we also verified their possible signal

contribution in our experiments. To extract any FMO fragments from the stock solution, we used a 50 kDa molecular weight-based centrifuge filter that traps FMO trimers while letting through dimers and smaller subunits. We spin coated the fragment solution onto the gold nanorod array and recorded 2D confocal scans of the sample (Figure 3.7b,d). Note that to avoid missing any fluorescent fragments due to excessive dilution, we used 100 times higher concentration than in the single trimer measurements.

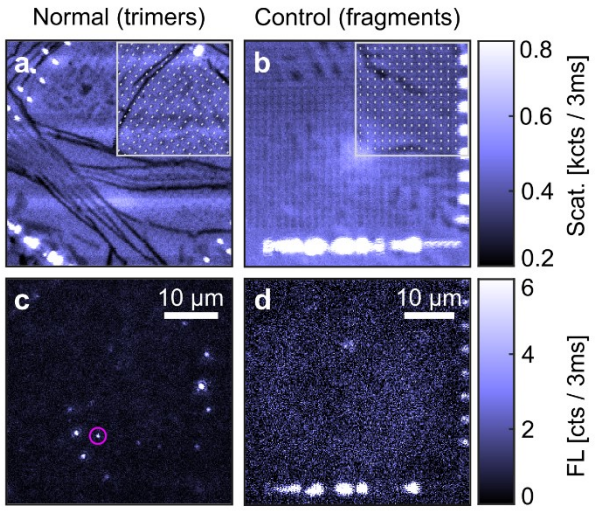

Figure 3.7 ***2D confocal scans of a gold nanorod array covered with FMO complexes and FMO fragments.*** *a,b) Scans without the long-pass filter in the detection path showing nanorods as dark spots with the array design (grey) overlaid in the top right corner as a guide for the eye. c,d) Fluorescence scans showing sparse bright spots for the normal sample containing FMO trimers and a featureless weak background for the control sample containing FMO fragments. The pink circle indicates a fluorescence spot that gives rise to the antibunching trace in Figure 3.8.*

The top row shows scattering scans with the gold nanorods visible as dark spots, a bright nanofabrication label at the bottom of the array and bright antenna length markers spaced every three nanorod rows along the side of the array. The array on the left is rotated as the orientation of the sample was fixed once mounted inside the cryostat. The dark lines across the nanorod arrays originate from the gaps in the spin-coated polymer film.

The bottom row of Figure 3.7 shows fluorescence scans of the same area. Understanding the map of the sample, we can compare the fluorescence signal of the FMO fragments and single trimers within the nanorod area delimited by the array label and nanoantenna length markers. The normal sample primarily made up of FMO trimers shows bright, sparsely spaced diffraction-limited spots that yield over 8 fluorescent counts per 3 ms (the maximum counts are capped to show several trimers). The 100x more concentrated fragment sample shows a uniform

fluorescence background across the entire nanorod array of 3-4 cts /3 ms. Thus, the 100-fold more concentrated fragment sample shows both, clearly lower signal and different spatial characteristic and hence we conclude that FMO fragments are either not present in our samples or they do not significantly contribute to the fluorescence in the FMO samples used in this work.

There are several indications that the bright fluorescence spots in the normal sample in Figure 3.7 correspond to single FMO trimers. Firstly, the low concentration and spin coating parameters should yield fewer than 0.03 trimers per diffraction-limited spot (section 3.2.2) that is corroborated by the sparse distribution of the fluorescence spots in Figure 3.7. In fact, this sample preparation has already been successfully used to yield single, well-dispersed light-harvesting complexes in the past.[89] Moreover, the only previous experiment on single FMO complexes[63] reported using similar concentrations that also yielded sparse fluorescence spots assigned to single trimers without any indication of aggregation tendencies of the FMO complex. Thus, we are confident that we do observe single FMO trimer fluorescence. Since the aforementioned study on single FMO complexes was conducted at 1.2 K, this constitutes the first single FMO trimer observation at the room temperature and is only possible thanks to the plasmonic enhancement by the gold nanorods.

3.3.3 FMO trimer antibunching at room temperature

Reaching sufficient sensitivity to probe fluorescence of single FMO trimers allowed us to record their photon statistics to shed light on the energy transfer within the complex. Experimentally, we followed the same preparation as for the “normal” sample in Figure 3.7: on top of the gold nanorod array, we spin coated a low concentration FMO solution. We recorded 2D fluorescence sample scans that yielded sparse diffraction-limited fluorescence spots indicative of single FMO trimers. Selecting one spot at a time, we measured time-tagged fluorescence time trace on two identical detectors and evaluated the fluorescence antibunching statistics of each FMO trimer. We illustrate the measurement process for the fluorescence spot circled in pink in Figure 3.7 that corresponds to an FMO trimer coupled to a resonant 130 nm nanorod. The corresponding fluorescence time trace and antibunching curve are shown in Figure 3.8.

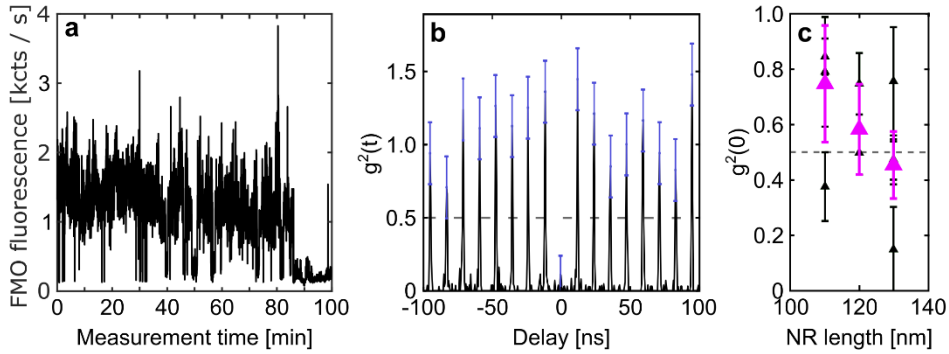

Figure 3.8 ***FMO complex antibunching at room temperature****. a) Fluorescence time trace of an FMO trimer on a 130 nm nanorod. The signal is a sum of the detected counts on two identical detectors. b) Second order correlation function of detector 1 to detector 2 retrieved from the time trace in a). The error bars are the standard deviation of the t≠0 peak height and indicate completeness of the measurement (smaller error bars mean sufficient number of photons was recorded to calculate a precise $g^2(t)$). c) Second order correlation at zero time delay of single FMO trimer candidates measured at different nanorod lengths. The error bars are the same as in b). The uncertainty-weighted average $g^2(t=0)$ for each nanorod length is shown in pink with the corresponding error scaled by the Student's t distribution 95 % confidence interval. The single-molecule threshold of 0.5 is marked by a dashed line.*

Even prior to the antibunching analysis, we can observe several important hints of single-molecule behaviour of the FMO trimer from the time trace in Figure 3.8a. Firstly, the signal irreversibly decays in a single step down to the background level at ~ 85 minutes as opposed to a step-wise bleaching that would be expected for multiple emitters. Moreover, before the irreversible single-step bleaching, the signal intermittently drops down to the background level for tens of milliseconds to a few seconds. These jumps are a result of the fluorophore temporarily entering a non-emissive state such as a triplet, radical or a dark conformation state.[18] Therefore, such fluorescence blinking strongly suggests a presence of a single emitter.

For a direct verification of the single-emitter character of the trimer, we calculated the second order correlation function between fluorescence photons from Figure 3.8a. Figure 3.8b shows the corresponding antibunching trace. Recall, that $g^2(t)$ takes the form of peaks separated by the laser pulse period. The error bars were calculated as the standard deviation of the $g^2(t \neq 0)$ peak height and indicate how well the non-zero time delays are sampled before the molecule photobleached and hence the uncertainty in the $g^2(t)$ normalisation (section 3.2.4).

The experimental threshold for a single emitter is $g^2(0) < 0.5$. Visually, the zero time delay peak in Figure 3.8b is clearly missing and the $g^2(0) = 0.14$ also fulfils the single-emitter condition. The deviation from 0 is likely due to noise in the $g^2(t)$

stemming from the low fluorescence intensity of single FMO trimers. As fragments of the FMO trimer do not give rise to any appreciable fluorescence, this constitutes the first experimental evidence of the single-emitter character of the FMO trimer and therefore, the "synchronisation" of all 24 BChls *a* pigments within the trimer.

However, the situation is more complicated as repeated measurements yield both, single- and multiple-emitter results (Figure 3.8c). Specifically, all antibunching measurements show a reduced $g^2(0)$. Estimating the antibunching baseline due to the low fluorescence intensity as $g^2_{base}(0) \approx 0.14$, the measured $g^2(0)$ values fit within the expected values for a single trimer with all monomers coupled ($g^2(0) < 0.5$) and all monomers independent ($g^2(0) = 1 - 1/3$). This result confirms that the BChls *a* within one monomer subunit are coupled forming an energy funnel to common low-energy state. However, the role of the excitation energy transfer between the monomers remains unclear. It is possible that the antibunching observed in Figure 3.8b is not a robust feature of the FMO complex and hence does not play a significant role in the energy transfer. Conversely, the variability between a single and three emitters could be caused by the resonant plasmonic enhancement itself. Even after enhancement, the fluorescence of single FMO trimers is very weak: one antibunching trace requires over 1 h integration time and over 80 % of molecules photobleach before emitting enough photons to calculate $g^2(t)$). Thus, we only measure the most enhanced trimers. To try to decouple the resonant plasmonic enhancement from the antibunching behaviour, we repeated the measurements at 77 K, which should yield additional fluorescence enhancement and allow antibunching measurements on off-resonant antennas (section 3.1.4).

3.3.4 Temperature effect on FMO trimer fluorescence

As outlined in section 3.1.4, reducing the temperature to 77 K will enhance the fluorescence by reducing temperature broadening of the absorption spectrum improving the overlap with the excitation laser and reducing vibration-mediated non-radiative decay, in other words increasing the fluorescence quantum yield. The latter is especially important in the FMO complex that undergoes significant fluorescence quenching likely by a cysteine residue in the protein matrix.[83,96]

To estimate the fluorescence enhancement thanks to cryogenic conditions, we recorded 2D fluorescence scans of six nanorod arrays covered by low-concentration FMO complexes embedded in a polymer matrix at both, room temperature and 77 K. An example array (Figure 3.9) shows a significantly brighter emission at 77 K

and the average fluorescence SBR improvement due to the decrease in temperature to 77 K across the six nanorod arrays is 2.48 ± 0.09 times.

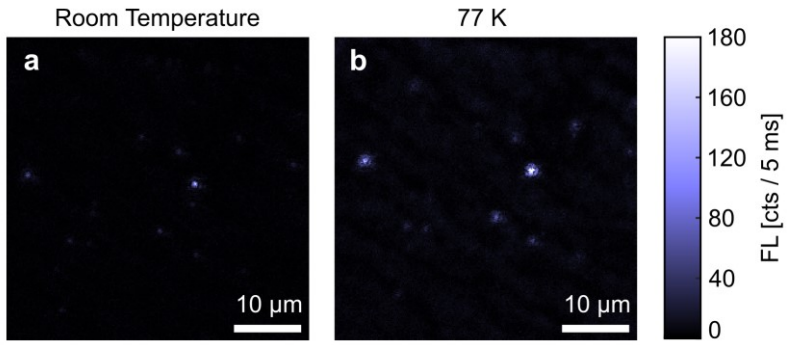

Figure 3.9 ***2D fluorescence scans of FMO trimer film spin coated on top of the same nanorod array.*** *The scans are recorded at a) room temperature and b) 77 K. The intensity bar is capped at the same value for both scans.*

Recalling that the antibunching trace is a second order correlation function, the fluorescence SBR increase of 2.48 results in 2.48^2 = 6-fold reduction in measurement time to obtain equivalent information as at room temperature. This is further illustrated in Figure 3.10 for two antibunching measurements on an FMO trimer coupled to a non-resonant, 150 nm nanorod.

The fluorescence time traces (top) show a SBR difference of ~ 3. Both traces exhibit blinking to the background level indicative of a single-emitter character, but the room temperature trace shows more intensity jumps and longer dark periods. The antibunching trace at room temperature was calculated from ~ 4000 s time trace (only the first 400 s shown) and the 77 K antibunching was calculated from the 350 s trace shown in Figure 3.10b.

Both $g^2(t)$ traces yield a reduced zero time delay peak. The stark difference is in the number of detected photons for every non-zero time delay combination. For 77 K, the antibunching trace shows clearly defined peaks separated by the laser pulse period that allow to establish the average non-zero peak $g^2(t \neq 0)$ with a small corresponding standard deviation (blue error bars). The zero time delay value can therefore be normalised by the average $g^2(t \neq 0)$ yielding $g^2(0) \approx 0.3$ that fulfils the single-emitter criterion of $g^2(0) < 0.5$. For the off-resonant room temperature case, very few photons are detected for each time delay. For example, the g^2 peak at -36 ps is buried within the noise and consequently, the variation in $g^2(t \neq 0)$ exceeds its mean value (error bars not shown for clarity). Thus, even though it is possible to calculate the normalised $g^2(t)$ as shown in Figure 3.10c, the associated uncertainty is too high to allow drawing any meaningful conclusions

about the number of emitters in the collection spot. This example illustrates the enormous benefit of the small improvement in the stability and fluorescence SBR of 2-3 times for recording fluorescence antibunching on single FMO trimers.

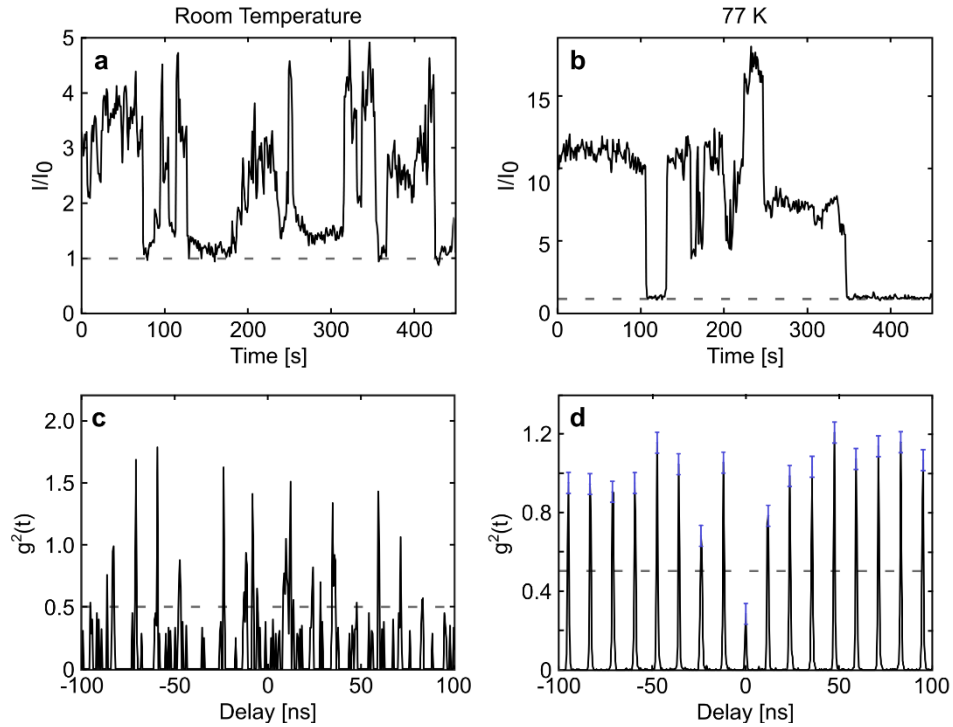

Figure 3.10 ***FMO complex antibunching at room temperature and 77 K for an off-resonant 150 nm nanorod.*** *a,b) Fluorescence time traces normalised to the background level and c,d) corresponding antibunching traces. The increased width of the ± 12 ns peaks in c) is due to back reflections between the two detectors.*

3.3.5 FMO trimer antibunching at 77 K

Having demonstrated the capability of studying non-resonantly enhanced FMO trimers by reducing the temperature to 77 K, we recorded 15 antibunching traces at nanorod lengths of 90-150 nm and calculated the second order correlation function at zero time delay for each measurement (Figure 3.11).

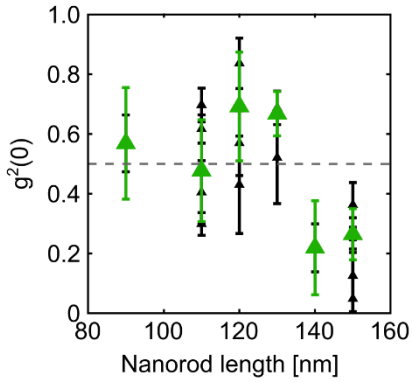

Figure 3.11 ***Antibunching of FMO trimers at 77 K for nanorod lengths of 90-150 nm****. The error bars represent the standard deviation of the non-zero peak counts of each antibunching trace. The uncertainty-weighted average $g^2(t=0)$ for each nanorod length is shown in green with the corresponding error scaled by the Student's t distribution 95 % confidence interval. The single-molecule threshold of 0.5 is marked by a dashed line.*

The error bars of individual measurements are smaller than in the room temperature data showing a more complete sampling of FMO fluorescence at non-zero time delays. For the resonant nanorods (110-130 nm), we see both single- and up to three-emitter photon statistics, similarly to the room temperature data. Out of six measurements on off-resonant antennas, only one (90 nm) shows a multiple-emitter fluorescence. This suggest that the native FMO trimers do behave as single emitters and the strong resonant fluorescence enhancement may effectively decouple them. In the following section, we explore the possibility of plasmonic enhancement influence on the photon statistics of FMO.

3.3.6 Excited state lifetime of the FMO complex

In section 2.3.4, we outlined that plasmoic nanoantennas enhance fluorescence by increasing the absorption rate by concentrating the incoming light into tight hotspots and increasing the outcoupling efficiency via fluorescence quantum yield enhancement. Recall that the fluorescence quantum yield depends on the radiative and non-radiative decay rates from the excited state according to Equation (2.11):

$$\Phi_{FL} = \frac{k_r}{k_r + k_{nr}}$$

Therefore, the outcoupling enhancement occurs by modifying the decay rates of the excited state, which can be probed experimentally by fluorescence lifetime measurements. Fluorescence lifetime, τ, is the average time that a molecule spends in its excited state[18] and is defined as the inverse of the sum of all decay rates from the excited state:

$$\tau = \frac{1}{k_r + k_{nr}}$$

(3.5)

Therefore, faster excited state decay due to a presence of a nanoantenna will appear as fluorescence lifetime shortening.[89,97]

Recall that the bulk FMO fluorescence lifetimes in the literature revealed a cysteine-mediated quenching pathway with a lifetime of 60-260 ps and a native BChl decay pathway with a 900-1500 ps lifetime.[81,82] The quenching pathway occurs on a similar timescale as the putative lifetime of the energy transfer between the FMO monomers of 29 ps[73] (Figure 3.8). Thus, it could be possible for a plasmonic nanoantenna to enhance the radiative decay rate of the FMO complex into a regime where fluorescence efficiently competes with the excitation energy hopping between the monomers. In a case where the energy transfer and subsequent radiation by the nanoantenna are faster than the intermonomer transfer, a single FMO trimer unit would appear as effective three emitters, which would agree with the antibunching data recorded at room temperature and 77 K. Here, we probe this possibility by measuring the fluorescence lifetime shortening of the FMO complex upon coupling to the gold nanorods.

As a reference, we first measured the bulk unenhanced fluorescence lifetime of the FMO complex embedded in the polymer matrix. We spin coated a high concentration FMO sample on a clean solid immersion lens (section 3.2.2) and recorded a time-correlated single photon counting (TCSPC) histogram of bulk FMO at room temperature and 77 K (Figure 3.12).

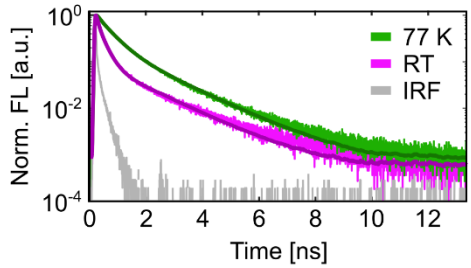

Figure 3.12 ***Fluorescence lifetime of bulk unenhanced FMO complex****. The multiexponential fits are shown as dark lines and the 52 ps instrument response function is shown in grey.*

Recall that we retrieve the fluorescence lifetimes by fitting the TCSPC histograms with a sum of exponentials with lifetimes τ_i with amplitudes, α_i and fractional contributions to the overall lifetime, f_i (section 3.2.5). We also calculated an

intensity (fractional contribution) weighted average lifetime, $\langle\tau\rangle$, to facilitate comparison between different measurements. The τ_i, α_i, f_i and $\langle\tau\rangle$ values obtained from the fit to the ensemble unenhanced FMO lifetimes in Figure 3.12 are summarised in Table 3.1 along with the literature values for comparison.[82]

Table 3.1 ***Exponential fit coefficient for fluorescence decay histograms of bulk unenhanced FMO complex at room temperature and 77 K.*** *The measured histograms were fitted with a sum of three exponentials with lifetimes τ_i and amplitudes α_i. The fractional contribution, f_i, of each lifetime component was used to calculate the average lifetime, $\langle\tau\rangle$, of the unenhanced FMO complex. The reference literature lifetimes (lit.)[82] are also show in parentheses.*

	RT			77 K		
$\boldsymbol{\tau_i}$ **/** $\boldsymbol{ps}$ **(lit.)**	67 (65)	229 -	1496 -	105 (118)	475 -	1521 (1490)
$\boldsymbol{\alpha_i}$	0.585	0.368	0.047	0.331	0.504	0.165
$\boldsymbol{f_i}$	0.202	0.435	0.363	0.066	0.456	0.477
$\langle\boldsymbol{\tau}\rangle$ **/** $\boldsymbol{ps}$	**656**			**950**		

At both temperatures, three exponentials were necessary to describe the FMO complex decay. The room temperature lifetime was fitted with a 67, 229 and 1496 ps component where the shortest component matches the monoexponential lifetime of 65 ps found in literature.[82] At 77 K, the excited state decayed with three components, 105, 475 and 1521 ps, where the shortest and the longest components also agree with literature (118 and 1490 ps).[82] The difference in relative contributions and the additional third component likely arise from the differences in the embedding medium. Specifically, polymer matrices have been shown to form charge transfer states[98] with the embedded fluorophores that could result in an additional decay pathway and hence the third lifetime component not seen in literature. The intensity-weighted average excited state lifetime that will serve as an unenhanced FMO complex reference is 656 ps and 950 ps at room temperature and 77 K, respectively. Note that the observed average lifetime shortening with increasing temperature has been attributed to increasingly higher contribution of the fast quenching pathway to the excited state decay of FMO complex.[83,96]

For single-molecule lifetime measurements, of plasmonically-enhanced FMO trimers, we followed the same sample preparation procedure as for antibunching experiments (low-concentration solution spin coated on a gold nanorod array, section 3.2.2). Examples of two enhanced FMO TCSPC histograms at room temperature and 77 K are shown in Figure 3.13 along with the unenhanced bulk data from Figure 3.12 as a reference.

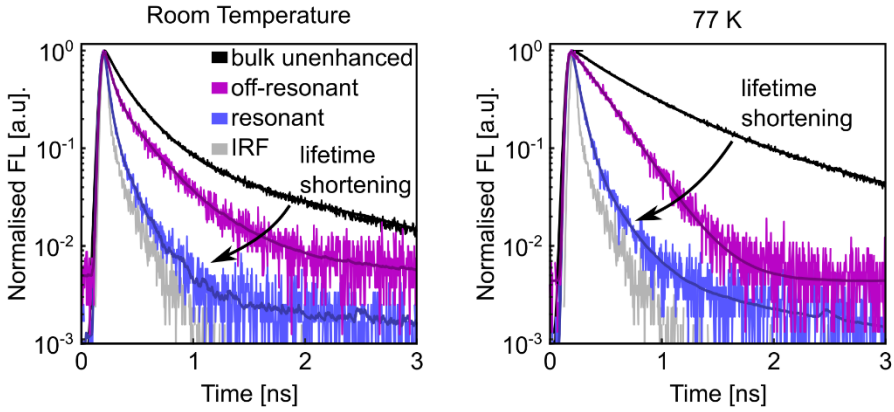

Figure 3.13 ***Fluorescence lifetime of enhanced FMO trimers****. The resonantly enhanced examples are measured on a 120 nm nanorod and the off-resonant data are measured on a 160 nm and a 150 nm nanorod at room temperature and 77 K, respectively.*

At both temperatures, FMO shows lifetime shortening upon coupling to the nanorods. For the resonant nanorods of 120 nm, the lifetime shortening is more pronounced as expected for a stronger plasmonic modification of the excited state decay rates. The exponential fitting parameters of the plots in Figure 3.13 are summarised in Table 3.2. All TCSPC histograms were fitted with a sum of three exponentials except for the non-resonant case at 77 K where two exponentials were sufficient. In all cases, the shortest lifetime ranges around a few tens of ps, being shorter than the instrument response function of 52 ps and comparable to the intermonomer energy transfer timescale of 29 ps.

Table 3.2 ***Exponential fit coefficients for fluorescence lifetime of enhanced FMO trimers at room temperature and 77 K.*** *The measured decay histogram was fitted with a sum of three exponentials with lifetimes τ_i and amplitudes α_i, except for non-resonant data at 77 K where two components described the decay well. The fractional contribution, f_i, of each lifetime component was used to calculate the average lifetime, $\langle\tau\rangle$, of the enhanced FMO complex. Average lifetime shortening with respect to bulk unenhanced FMO is shown in parentheses. The resonantly enhanced examples were measured on a 120 nm nanorod and the off-resonant data were measured on a 160 nm and a 150 nm nanorod at room temperature and 77 K, respectively.*

	RT			**77 K**		
$\boldsymbol{\tau_{i,res}/\ ps}$	25	100	1830	48	238	1445
$\boldsymbol{\tau_{i,non\text{-}res}/\ ps}$	42	215	581	36	232	-
$\boldsymbol{\alpha_{i,res}}$	0.958	0.001	0.041	0.992	0.006	0.002
$\boldsymbol{\alpha_{i,non\text{-}res}}$	0.824	0.146	0.029	0.288	0.712	-
$\boldsymbol{f_{i,res}}$	0.815	0.138	0.047	0.915	0.027	0.058
$\boldsymbol{f_{i,non\text{-}res}}$	0.418	0.378	0.205	0.059	0.941	-
$\boldsymbol{\langle\tau\rangle_{res}\ /\ ps}$	**121 (5-fold)**			**134 (7-fold)**		
$\boldsymbol{\langle\tau\rangle_{non\text{-}res}/\langle\tau\rangle}$	**218 (3-fold)**			**221 (4-fold)**		

Similarly, to the bulk unenhanced data, the shortest lifetime is more dominant at higher temperature as can be seen in the non-resonant single enhanced FMO trimers. Interestingly, resonant enhancement further increases the contribution of the short lifetime component and the excited state decay of FMO coupled to a resonant 120 nm nanorod is almost fully dominated ($f_i > 0.8$) by sub-50 ps lifetime at both temperatures. This indicates a very efficient energy transfer from the FMO complex to the nanorod. We quantified the lifetime shortening with respect to bulk unenhanced FMO complexes through average lifetimes, $\langle\tau\rangle$, that do not depend on the number of fitted exponents. The lifetime shortening on resonant nanorods is almost twice as strong as on off-resonant 160 and 150 nm nanorods in the room temperature and 77 K cases, respectively. Therefore, we experimentally confirmed both requirements for a plasmonic enhancement modulation of the antibunching behaviour of single FMO trimers: an energy transfer to the nanorod on a similar timescale as the intermonomer transfer and a significant difference between resonant and non-resonant enhancement.

3.3.7 Effect of plasmonic lifetime shortening on fluorescence antibunching and the implications for energy transfer in the FMO complex

For a direct insight into the relationship between the plasmonic lifetime shortening and fluorescence antibunching measurements, we conducted both measurements on the same single FMO trimers. This approach is crucial as slight variation in the antenna-molecule distance and orientation can have a dramatic influence on the plasmonic enhancement as outlined in section 2.3.4 and evidenced by the large range of $g^2(0)$ values for a given nanorod length (Figure 3.8c and Figure 3.11). Due to the limited photon budget, over 75 % of measured trimers photobleached before both measurements were completed. However, we did manage to record fluorescence lifetime and antibunching for 23 FMO trimers. Out of these, 20 showed fluorescence lifetime components below 30 ps, on the same or faster timescale than the energy transfer between the monomer subunits. We plotted their normalised second order correlation at zero time delay, $g^2(0)$, against the fractional contribution (section 3.2.5) of the sub-30 ps lifetime to the overall decay of the FMO trimer, $f_{<30\,ps}$ (Figure 3.14).

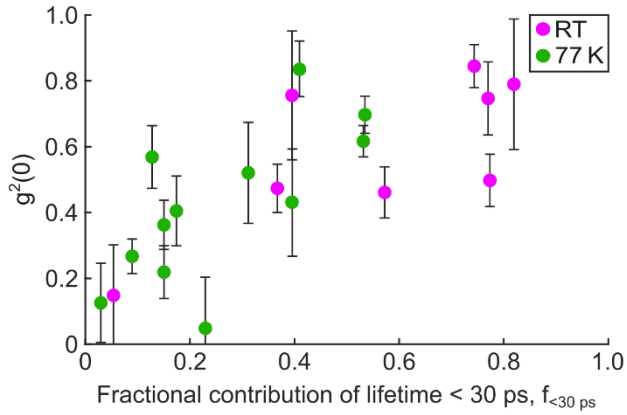

Figure 3.14 ***Relationship between fluorescence antibunching and lifetime shortening of plasmonically-enhanced FMO trimers.*** *Second order correlation at zero time delay of single plasmonically-enhanced FMO trimers plotted against the corresponding fractional contribution of fluorescence lifetime component shorter than 30 ps. The antibunching errors correspond to the standard deviation of antibunching peaks at non-zero time delay. The data was measured on FMO trimers coupled to 90-150 nm nanorods.*

The single-trimer data in Figure 3.14 show that FMO trimers with more dominant sub-30 ps lifetime components do yield increased $g^2(0)$, supporting the hypothesis of competition between energy transfer to the nanorod and the neighbouring monomer subunits. By correlating the two variables directly instead of rationalising the observations in terms of nanorod resonances, we take into account both, the plasmonic properties of the nanorod as well as the coupling of the FMO trimer to it. In other words, we effectively cancel out the hotspot variability, provided that both fluorescence lifetime and antibunching are affected by the same hotspot properties, which our data do suggest.

For example, as the room temperature data was measured on resonant nanorods with stronger plasmonic enhancement, they also show multiple emitter character for the FMO trimer ($g^2(0) > 0.5$) already seen previously. However, Figure 3.14 also shows that the only clear single-emitter FMO trimer at room temperature does also exhibit significantly lower excited state decay contribution from the sub-30 ps component, suggesting a weaker plasmonic enhancement and rationalising the single-emitter character $g^2(0) = 0.14$.

Overall, plasmonically-enhanced FMO trimers can behave effectively as single- or up to three emitters as determined by fluorescence antibunching measurements. The single-trimer $g^2(0)$ values increase with increasing excited state decay contribution from a sub-30 ps lifetime component, which is comparable to the timescale of the excitation energy transfer between the monomers. This suggests that coupling to plasmonic nanorods can modify the native radiative and

non-radiative decay rates of the FMO complex to the extent that energy transfer to the nanorod (short lifetime dominates excited state decay) can outcompete the excitation energy exchange between the monomers, effectively decoupling the three subunits and resulting in an antibunching signature of three independent emitters.

Note that fluorescence lifetime can also be used to extract the efficiency of resonance energy transfer, E_{FRET}, using the lifetime of the donor in the absence, τ_D, and presence of an acceptor, τ_{DA},[18] as:

$$E_{FRET} = 1 - \frac{\tau_{DA}}{\tau_D} \quad (3.6)$$

In this case, the FMO monomers do not fluoresce (section 3.3.2), but it would be interesting to study plasmonically-enhanced systems with fluorescing subcomponents and the relationship between the antibunching and fluorescence lifetimes to gain a deeper insight into the competing molecule-molecule and molecule-nanoantenna energy transfers.

Our findings have several important implications for the excitation energy transfer in the FMO complex. Firstly, the single-emitter character of the FMO trimer directly proves the existence of the intermonomer energy transfer and the entire complex operating as a single unit in photosynthesis. This is not surprising because the complex has evolved as a homotrimer (three identical subunits) indicating some advantage over a separate monomer arrangement. Recall that role of the FMO complex is to channel the energy harvested by the antenna towards the reaction centre. In case the photosynthetic antenna harvests too many photons, the intermonomer energy transfer provides a regulatory mechanism in terms of singlet-singlet annihilation,[99] protecting the reaction centre from excessive energy flux.

Secondly, the dramatic enhancement of the excited state decay rates upon resonant enhancement to the point of outcompeting energy transfer between monomers underlines the efficiency of the FMO complex for energy funnelling. It would be interesting to shed more light on the specific property of FMO that allows such efficient energy transfer for example by repeating the single-molecule measurements on different FMO mutants.

We expect that the distance and orientation of the BChls within a monomer ensure efficient energy transfer to the lowest energy site and the orientation and

separation between the lowest energy BChls of different monomers regulate the extent of excitation annihilation. For example, a similar light-harvesting complex 2 (LH2) contains 27 BChl *a* molecules, but shows a robust fluorescence antibunching even under resonant plasmonic enhancement.[89] Interestingly, the fluorescence lifetimes of plasmonically-enhanced LH2 are also short, 10s of ps. However, the lowest energy BChls are arranged in a closely-spaced ring[55] allowing an efficient singlet-singlet annihilation which explains the persistence of antibunching. Repeating the lifetime and antibunching measurements on more light-harvesting complexes with BChl *a* could further elucidate the effect of different pigment arrangement into the energy transfer regulation in photosynthesis.

3.4 Conclusions and future outlook

We studied plasmonically-enhanced FMO pigment-protein complexes by fluorescence cryomicroscopy. Using gold nanorod antennas, we achieved plasmonic enhancement of 13+ times, maximised for nanorod length of 120 nm resonant with the FMO complex absorption and fluorescence transitions. Combining the plasmonic enhancement and vacuum conditions allowed us to detect fluorescence of single FMO trimers, for the first time at 77 K and room temperature. Recording fluorescence photon statistics of single FMO trimers, we observed photon antibunching below the threshold for multiple emitters at both temperatures showing that the entire FMO trimer behaves as a single quantum emitter. This is the first direct experimental proof of the energy transfer between the monomer subunits of FMO and we believe it serves as a regulation of energy transfer during photosynthesis via annihilation of excessive excitations.

On resonant nanoantennas, the FMO complex can also behave as two to three emitters consistent with an independent operation of the individual monomers. By measuring both, fluorescence lifetime and antibunching for each FMO trimer, we showed that increasing dominance of lifetime component comparable to the timescale of the intermonomer energy transfer was correlated to the multiple-emitter character of the fluorescence photon statistics. This suggests that energy transfer to the nanoantenna outcompetes that between the monomers for the highest enhancements achieved here by the resonant nanorods of 110-130 nm. In other words, by tuning the resonance of the nanorods, we managed to modulate the amount of excitation annihilations effectively decoupling the individual monomers of the FMO complex.

Our measurement setup reaches excellent sensitivity by combining cryomicroscopy with plasmonic enhancement and single photon counting detection. The main drawback of the current experiment is its low throughput (a few molecules per day) due to the extremely weak emission from the FMO complex. Since acquiring a statistically-significant dataset is unrealistic, measurement conditions must be carefully controlled or uncontrolled degrees of freedom cancelled out during the analysis such as by correlating the fluorescence lifetime to the antibunching when both depend on the same plasmonic enhancement. Therefore, to gain further insight into the role of the pigment arrangement in the energy transfer during photosynthesis, it would be interesting to repeat the measurements on FMO mutants or other light-harvesting complexes whose geometries are well known or can be carefully controlled using DNA editing.

4 Automated Microscope for Statistical Screening of Single SERS Nanoparticles

Plasmonic nanoparticles can enhance Raman scattering of molecules at their surface over 10^{12} times. This surface-enhanced Raman scattering (SERS) has even reached sensitivities down to a single molecule opening up possibilities for chemically-specific ultrasensitive sensing applications. However, the extreme enhancements are difficult to reproduce on a particle-to-particle basis, which represents a major hurdle towards quantitative SERS required for sensing applications. A typical development of new SERS nanoparticles involves their bulk synthesis, nanoscale plasmonic simulations and SERS performance testing in bulk, making it difficult to correctly link real nanoscale properties to the SERS sensing potential.

In this chapter, we present a home-built microscope for nanoscale SERS nanoparticle screening tested on ten nanoparticle types functionalised with a standard SERS reporter, 2-naphthalenethiol at two illumination wavelengths. We probe the effects of sample morphology on the SERS response and measure SERS traces for a statistically-significant number of discrete spots across the sample. This single-spot data collection allows correlating various SERS parameters such as intensity, signal to background ratio and temporal stability, yielding a detailed nanoscale insight into the sample performance. For example, measurements at nanoparticle resonance tend to yield increased SERS background that results in overall lower SERS reproducibility. Furthermore, we employ dark-field scattering imaging that allows us to identify the number of nanoparticles in the SERS collection spot. By sorting the SERS measurements into single and multiple particles, we uncover SERS intensity variations among single nanoparticles, which is the most important parameter for quantitative SERS sensing. Overall, our nanoparticle screening platform provides a detailed nanoscale insight into the SERS performance of nanoparticles beyond the capabilities of bulk measurement techniques. As such, our approach can accelerate the rational design of new SERS nanoparticles for quantitative sensing applications.

4.1 Introduction

In the previous chapter, we explored the use of plasmonic nanoantennas to enhance molecular fluorescence allowing observations of even the poorest emitters like photosynthetic complexes at an unprecedented single-molecule level. This enabled us to probe energy transfer in photosynthesis at its fundamental single-molecule level and directly confirm electronic coupling between subunits of the photosynthetic complex. We also identified the main experimental limitation as an irreversible photo bleaching of the molecule after a given number of excitation-fluorescence cycles. By employing vacuum and cryogenic conditions, we did manage to record photon statistics at a single-molecule level for a wide range of measurement conditions until hitting the fundamental photon budget limit again. In addition to the experimental hurdle, statistical undersampling complicated the interpretation of the results. In this chapter, we build on these lessons and develop a platform for a multi-parameter characterisation of plasmonic nanoparticles for surface-enhanced Raman scattering (SERS) at a statistically-significant level and a single-particle sensitivity.

4.1.1 State of the art of SERS applications

SERS was first reported in 1974 for pyridine adsorbed on a roughened silver electrode.[10] Twenty four years later, single-molecule SERS was achieved,[52,53] which stimulated a lot of interest because of the implication of extremely high plasmonic enhancements being present and the resulting possibilities for practical applications of SERS as ultrasensitive probes. In the past two decades, a myriad of SERS platforms has been developed for detecting trace amounts of target molecules (Figure 4.1).

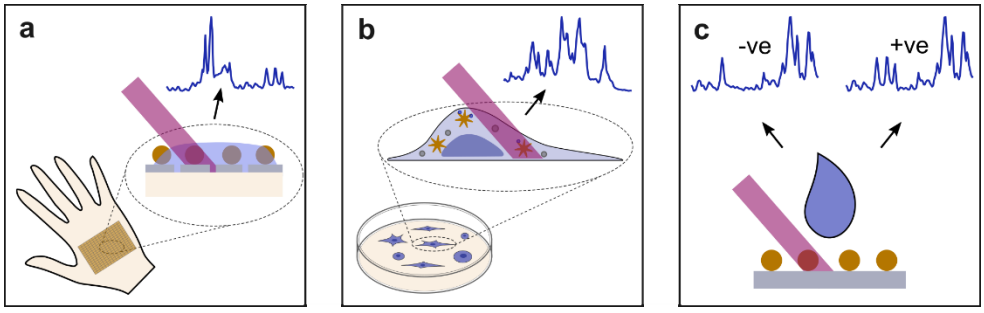

Figure 4.1 ***Schematic representations of SERS-based sensing platforms.*** *a) Wearable flexible SERS substrates for monitoring of biomarkers in sweat, b) in-vivo monitoring of cell metabolism suing SERS nanoparticles and c) SERS sensor for testing for trace amounts of substances from soil, blood or food.*

Environmental applications include detection of pollutants in soil[100,101] and nicotine in tobacco smoke.[102] In food safety, SERS was implemented to detect toxic

substances in crops[103] and processed food.[104] In-vivo biomedical applications include monitoring of cell metabolism[105–107] and cell differentiation.[108,109] In-vitro efforts focus on early diagnosis of diseases by identifying target molecules in body fluids,[110–114] some of them even wearable on the skin[115,116] or proposed to be integrated into everyday devices such as an intelligent toilet.[117] SERS can also be incorporated into a powerful diagnostic imaging.[118,119]

Despite the demonstrated utility of SERS in virtually any field, industrial-scale implementation of quantitative SERS sensors is still hindered by practical considerations.[117] Whereas previous efforts focused on maximising the sensitivity of SERS devices through highest possible enhancements, current targets involve improving the reproducibility and stability of SERS substrates and developing protocols to ensure repeatability of the measurements. The main challenge stems from the fact that the highest enhancement, therefore the highest sensor sensitivity, is available in the most extreme plasmonic hotspots such as gaps between closely-spaced plasmonic nanoparticles or tips of metallic nanoparticles like nanostars.[120] Since the most common preparation method of SERS nanoparticles is colloidal chemistry, possibly followed by a self-assembly into a sensor, these extreme hotspots are also the least reproducible while giving rise to a significant fraction of the total SERS signal in a sample. For example, an experiment on benzenethiolate molecules adsorbed on silver nanoparticles showed that 24 % of the overall SERS was generated by only 64 hotspots in 1 000 000.[121] In addition to the substrate variability, analyte molecules distribution within these extreme hotspots may differ between individual measurements. As such, different sample batches or even repeated measurements can produce signals varying by orders of magnitude.[122]

4.1.2 Optimisation strategies towards SERS sensing

Some successful strategies to improve reproducibility involve nanoparticle functionalisation with molecular ligands and antibodies to control the position of the nanoparticles and/or analytes.[123–126] Measurement repeatability strategies and protocols compatible with international diagnostic standards are also being developed.[127,128] A typical optimisation workflow towards a quantitative SERS platform involves synthesis and bulk characterisations of the SERS nanoparticles by absorption spectroscopy that probes the plasmon resonance of the nanoparticles. Experimental determination of a small fraction of nanoparticles is also done by electron microscopy. The measured nanoparticle geometries and plasmon resonance are used to build and validate, respectively, a computational simulation of the nanoparticles that can give a deeper insight into their plasmonic response. All

this supporting data is then used in combination with the actual SERS measurement with an analyte of interest to rationalise the design of nanoparticles with improved properties such as signal, stability and specificity for a desired molecule. New nanoparticles are synthesised and the process is repeated.

The ability of this optimisation strategy to converge to better SERS platforms is severely hindered by the gap between the SERS sensing experiment and the supporting measurements. Specifically, recall that the bulk SERS response of a sample can be dominated by few extreme hotspots. In contrast, the absorption, electron microscopy and modelling information reports on the average hotspots. Therefore, single-particle SERS measurements are highly desired to properly correlate experimental parameters such as particle resonance, laser wavelength and power, to the SERS response such as SERS counts, spectral stability and SERS to background, for each nanoparticle separately.

Commercial Raman microscopes are already capable of acquiring hyperspectral Raman images that, combined with some nanoparticle identification algorithm, can analyse single SERS nanoparticles at a high throughput. Their cost is however somewhat prohibitive and more importantly, their customisation complicated. Some novel SERS platforms for nanoparticle screening combining Raman and Rayleigh scattering have recently been developed,[129] but a high-throughput was achieved by sacrificing the spectral resolution and limiting the types of samples that can be addressed to sparsely-distributed nanoparticles that inherently limits the maximum achievable throughput. Here, we present a versatile setup to screen SERS nanoparticles using multiparameter correlation of properties influencing the SERS response. Using a library of ten different types of typical SERS nanoparticles at two illumination wavelengths, we record wide-field SERS or dark-field (DF) scattering images and single-spot SERS spectral traces to retrieve SERS intensities, time fluctuations and signal-to-background (SBR) ratios of single- to few-nanoparticles at a time. By revealing the underlying nanoparticle distributions across this multiparameter space, we uncover SERS performance differences of different nanoparticle types obscured in typical ensemble measurements. We also discuss a non-trivial relationship between SERS and DF scattering signal showing that SERS signal itself cannot be used to discriminate between single and multiple nanoparticles probed here in the context of SERS sensing. Our results form basis for a rational design of new SERS nanoparticles for quantitative SERS sensing.

4.2 Methods

4.2.1 Sample preparation

All SERS nanoparticles were synthesised by metal reduction from a solution assisted by stabilising agents by the group of Prof Ramón Álvarez Puebla in Tarragona. The same group also kindly provided the transmission electron microscopy (TEM) images in Figure 4.2a. Ten different nanoparticle samples were used divided into five types: silver nanospheres (Ag NSs), gold nanorods (Au NRs), gold-silver nanorods (AA NRs), gold round nanostar (Au rNSt) and gold nanostars (Au NSts). Nanoparticles were received as colloidal suspensions in ethanol or water. Stocks in ethanol were centrifuged and redispersed in Milli-Q water to produce one comparable set of SERS nanoparticles.

Table 4.1 ***List of sample codes used through this work and the corresponding basic properties and sample preparation parameters.***

Sample ID	Nanoparticle shape	Absorbance max in Milli-Q / nm	Solvent Exchange: rpm + min
Ag NS 405	nanosphere	405	-
Ag NS 425	nanosphere	425	-
Au NR 635	nanorod	635	3x 3000 rpm, 10 min
Au NR 780	nanorod	780	3x 4000 rpm, 10 min
AA NR 635	nanorod	635	2x 6000 rpm, 10 min
AA NR 780	nanorod	780	2x 4800 rpm, 10 min
Au rNSt 590	nanostar	590+	4400 rpm, 10 min
Au NSt 760	nanostar	760	3000 rpm, 10 min
Au NSt 810	nanostar	810	2500 rpm, 10 min
Au NSt 910	nanostar	910	2500 rpm, 10 min

The integrity of the nanoparticles was checked by absorption spectroscopy (Lambda 950, PerkinElmer), where only one sample, Au rNSt 590, showed a redshifted shoulder attributed to a fraction of particles that aggregated[20] during the solvent exchange (Figure 4.2b). Note that the sample code consists of the nanoparticle type followed by its absorption maximum wavelength in the milli-Q water to simplify the interpretation of results within the context of the nanoparticle resonance. For all samples, the solvent exchange was performed on the day of the SERS measurement. This prevented significant particle aggregation before the measurement due to removal of surfactant molecules present in the stock solution.

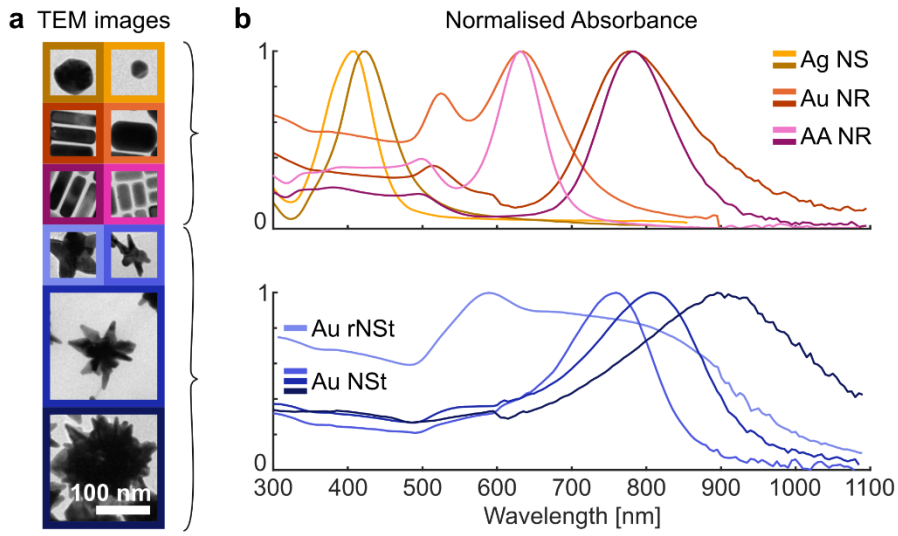

Figure 4.2 ***Transmission electron microscope (TEM) images of SERS nanoparticles and absorption spectra of the corresponding suspensions in Milli-Q water.*** *a) TEM images showing geometries spanning nanospheres (NSs), nanorods (NRs), a round nanostar (rNSt) and nanostars (NSts). b) Absorption spectra of particles in a) showing healthy narrow peaks except for the rNSt resonant at 590 nm where a broad redshifted shoulder suggests aggregation of a fraction of the nanoparticles.*

Nanoparticles suspended in Milli-Q water were functionalised with 2-naphthalenethiol (2-NT) used as a common SERS reporter due to its strong Raman response from the aromatic bonds and its ability to bind to gold and silver via the thiol group. Unless stated otherwise, nanoparticle suspension (~ 0.1 mM in Milli-Q water) was mixed with 2-NT (0.05 mM in EtOH) in a 9:1 ratio and deposited on a clean glass cover slip (~ 4 µL per 22x22 mm area). In this work, we refer to this procedure as the "mix and drop" method.

The glass cover slips were cleaned prior to nanoparticle deposition by sonicating in acetone (15 min) and Milli-Q water (15 min). Drop-casting functionalised nanoparticles on a cover slip at this stage produced mostly clusters as verified by scanning electron microscope (Inspect F, FEI company). An example image is shown for Au NRs resonant at 635 nm (Figure 4.3a). Therefore, we additionally treated the cover slips with oxygen plasma (5 min). In addition to removing organic contaminants from the cover slip, the oxygen plasma charged the glass surface aiding in quick solvent and hence nanoparticle dispersion across the whole surface of the cover slip. Combining the surface charging with a small volume of sample solution yielded a thin uniform layer or nanoparticle suspension that evaporated within a few seconds yielding a sparse nanoparticle distribution on the cover slip (Figure 4.3b).

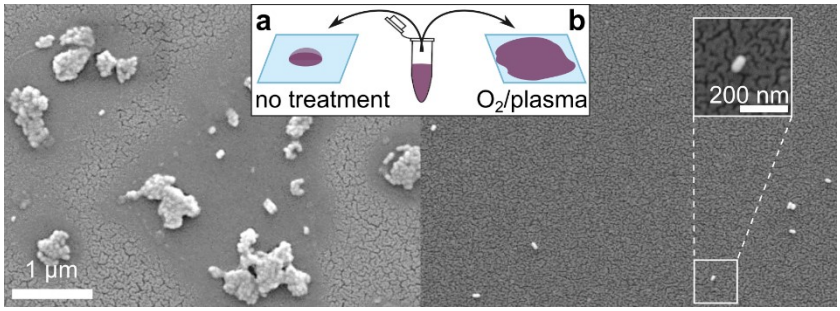

Figure 4.3 ***Scanning electron microscope images of 2-NT functionalised Au nanorods deposited on a cover slip*** *cleaned by a) sonicating in solvents and b) additionally treated by oxygen plasma. The oxygen plasma treatment changes the surface properties of the glass aiding in solvent dispersion and evaporation yielding sparsely-distributed nanorods that otherwise clump together.*

4.2.2 SERS measurements

Automated scanning Raman microscope guided by wide-field imaging

All measurements were performed on a home-built automated Raman microscope (Figure 4.4). Illumination at 633 nm was generated by a HeNe laser cleaned up with a 633/10 bandpass filter (ThorLabs) or at 781 nm using a laser diode (Micro Laser Systems) passing through a 780 nm laser line filter (Semrock). The incoming light was focused onto the edge of the back focal plane of an NA 1.49 TIRF oil-immersion objective (APON 60XOTIRF, Olympus) by translating a rod mirror away from the centre of the objective just before the light intensity transmitted through the objective started decreasing. This yielded a wide-field illumination spot of ~ 5 µm diameter at the sample.

The scattered (full NA) and reflected (high NA) light was collected by the same objective. Note that Figure 4.4 only shows the high-NA fraction of the collected light, but full NA range is detected except for the light blocked by the rod mirror and, in DF measurements, the additional DF mask. Approximately 5 % of the collected light was focused onto an EMCCD camera (ImagEM X2, Hamamatsu) to record the sample image. In SERS configuration, this image was recorded by spectrally selecting a portion of the Stokes-shifted light with respect to the illumination laser (647 LP + 692/40, Semrock for 633 nm laser and 808 LP + 832/37, Semrock for 781 nm laser). In dark-field (DF) configuration, the size of each nanoparticle was inferred from the Rayleigh scattering intensity. Thanks to the side illumination facilitated by the off-centred rod mirror, the light reflected from the sample was easily blocked mechanically, spatially selecting the DF-scattered photons. The DF scattering was then focused onto the EMCCD camera to yield a wide-field image. Note that the DF scattering is overwhelmingly dominated by the Rayleigh photons so the terms are used interchangeably here.

The collected light not sent into the imaging path was spectrally filtered through two notch filters matching the laser wavelength (633 nm or 785 nm, Semrock). The reflected light was focused into a webcam used in an autofocusing feedback loop. The transmitted light was sent into a home-built fibre-coupled Raman spectrometer and detected on an EMCCD camera (Newton, Andor). The spectrometer resolution was 0.16 nm. The fibre also served as a pinhole selecting a 1.5 µm diameter spot on the sample which, with a sufficiently sparse coverage, selected a single nanoparticle at a time. The sample was mounted on a 2D motorised stage (8MTF-200, Standa) programmed for raster-scanning. A z-piezo stage (PU 100, piezosystem Jena) controlled by ADwin system (ADwin Gold II, Jäger GmbH) maintained the sample in focus using a feedback loop based on the lateral spot position of the reflected light on the webcam.

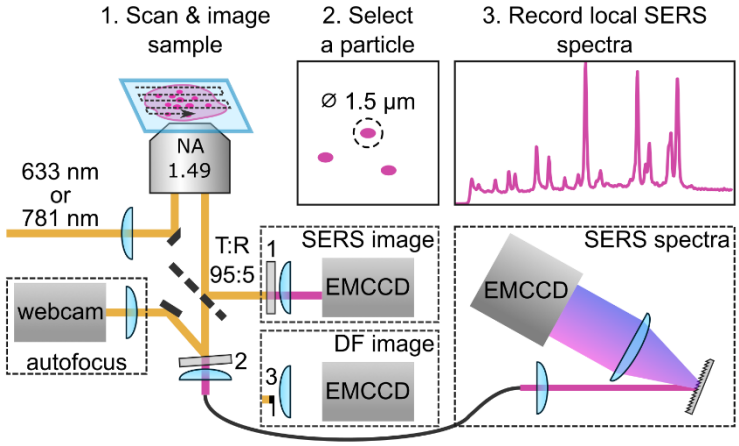

Figure 4.4 ***Automated microscope for quantitative single-particle SERS measurements.*** *A CW laser is focused onto the back-focal plane of an oil-immersion objective yielding a collimated beam at the sample. Reflected and scattered light is collected through the same objective and a small fraction is sent onto an EMCCD camera to yield a sample image. In SERS configuration, Stokes band is selected (1= 647 LP + 692/40 for 633 nm laser and 808 LP + 832/37 for 781 nm laser) and in dark-field configuration, reflected light is blocked mechanically (3). 95 % of the collected light is sent into a fibre-coupled spectrometer (2= 2x 633 nm notch or 2x 785 nm notch) where the fibre acts as pinhole yielding a 1.5 µm collection spot at the sample plane. The back-reflected light from the notch filters is focused onto a webcam for autofocusing feedback facilitating a fully automatized operation consisting of scanning across the sample, identifying single SERS spots in each field of view and measuring the corresponding SERS spectra.*

Measurement workflow

The sample was raster scanned using the 2D motorised translation stage and imaged on an EMCCD camera. Unless stated otherwise, Stokes photons were spectrally filtered yielding a SERS image. For measurements explicitly probing the nanoparticle size, a DF mask was used to yield a Rayleigh scattering image of the sample. For each field of view, a single bright spot was selected at random and then moved by the 2D

motorised stage into the collection spot given by the spectrometer fibre. Sixteen SERS spectra were recorded for each spot as well as one sample image before and after to ensure the sample had not drifted during the measurement. The stage then moved the sample by several micrometres (~ 1 field of view) to previously unilluminated nanoparticles and the process was repeated, until sufficient single-spot statistics was built up. Note that in the SERS imaging configuration, the pre-selection of nanoparticles based on Stokes SERS made the measurements insensitive to non-enhanced sample features such as dirt, increasing the duty cycle of the SERS measurement. Conversely, in the dark-field imaging configuration, sub-diffraction size of the nanoparticles in the collection spot could be inferred from the intensity of the Rayleigh scattering, allowing identification of single SERS nanoparticles.

4.2.3 SERS spectra analysis

The wavelength axis was mapped onto the spectrometer camera pixels by recording emission from a mercury argon calibration lamp (HG-1, Ocean Optics) followed by a linear fit of the detected peaks across the pixel range (Figure 4.5a). Raw SERS spectra were scaled by a wavelength-dependent instrument efficiency so that SERS counts under 633 and 785 nm illumination could be compared quantitatively. Additionally, the spectra were corrected for etaloning, an interference pattern of incoming and back-reflected photons from the camera. This was especially critical for the 781 nm illumination where the quantum efficiency of the camera and hence the fraction of absorbed photons tails off.

Experimentally, the scaling factor for the SERS spectra was determined by recording a spectrum of a tungsten-halogen lamp (HL-2000, Ocean Optics) with a smooth and well-defined spectrum. An example for 781 nm illumination is shown in Figure 4.5b. The fringes on top of the spectrum result from the etaloning and the decreasing intensity towards the high pixel number stems from the wavelength-dependent efficiency of the spectrometer – mostly due to the camera and the grating. The “real” spectrum of the same lamp was measured and scaled on a spectrometer with known efficiency. This “real” spectrum was then divided by the measured data from Figure 4.5b, yielding the efficiency correction curve for the spectrometer. To account for the wavelength-dependent transmission of the objective, the efficiency correction was divided by the objective transmission obtained from manufacturer specifications (Figure 4.5, purple). Repeating the process at 633 nm ensured a correct wavelength scaling and quantitative comparison at different illumination wavelengths.

Lastly, the absolute magnitude of the correction factor was determined to ensure the reported SERS counts corresponded to the number of emitted photons. Specifically, a purely specifications-based correction factor was calculated as an inverse of transmission curves for the camera, grating and objective (Figure 4.5c, black curve). The measured correction factor was then scaled to the same average (Figure 4.5c, yellow). Note that the measured (yellow) and specifications-derived (black) correction curves match well, verifying that wavelength dependence of the spectrometer is almost fully dictated by the camera and the grating.

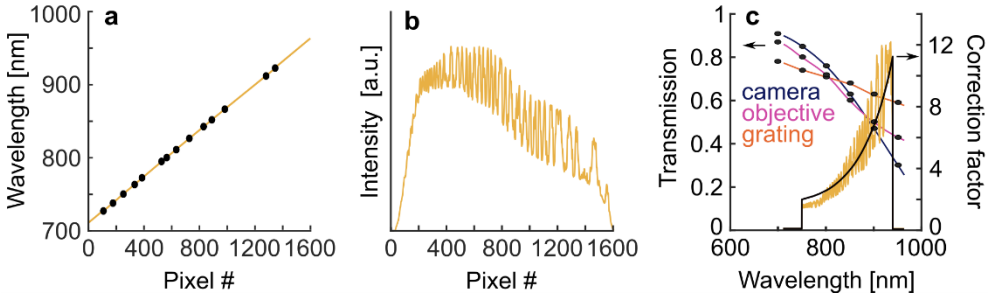

Figure 4.5 ***SERS data analysis workflow example for 781 nm illumination****. a) Pixel to wavelength curve fitted to a calibration lamp (black dots). b) Measured emission of a thermal light source for etaloning correction. c) Transmission data from specifications (black dots) interpolated and multiplied to give a smooth correction factor for wavelength-dependent detection efficiency (black curve). Dividing the correction factor by the curve in b) (normalised to one) yields the overall correction factor (yellow*

An example of a raw SERS spectrum of 2-NT linked to Au NR 785 (Figure 4.6) shows oscillatory modulation that could be mistaken for SERS bands (680, 950 and 1200 cm^{-1}). This modulation was removed by applying the correction factor from Figure 4.5. Additionally, the correction normalised the relative intensity of SERS bands for instrument response allowing for a quantitative analysis at different wavelengths. Note that for clean SERS spectra with low background, the correction does not change the results dramatically, however, for spectra with significant background contribution, it is crucial (Figure 5.9).

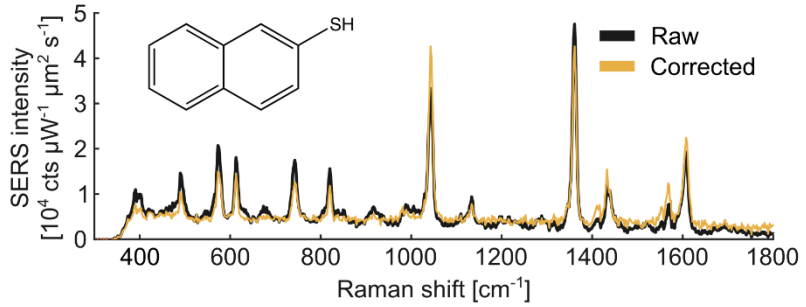

Figure 4.6 ***SERS spectrum of 2-naphthalenethiol measured at 781 nm on Au nanorods resonant at 780 nm****. The raw spectrum (black) is scaled by the correction factor from Figure 4.5 to yield the final spectrum (yellow). The Raman reporter molecule is shown in the inset.*

4.3 Results and Discussion

4.3.1 Single-spot SERS spectra

A characteristic SERS spectrum of 2-naphthalenethiol (2-NT) from a single SERS spot is shown in Figure 4.7a. This example is recorded at 633 nm using Ag nanospheres resonant at 405 nm (Ag NS 405), however, it applies to all samples as the same Raman reporter is used in all measurements. The total Stokes signal is composed of SERS signal (blue) on top of a broad background (grey) calculated by interpolating the signal between handpicked regions with no Raman bands. The broad background is typical for SERS measurements and can stem from inelastic scattering from the conduction electrons of the metal,[130] photoluminescence of the metal[131] and metal-molecule coupling.[132] The SERS-to-background ratio (SBR) of ~ 10 allows us to identify fifteen Raman bands.

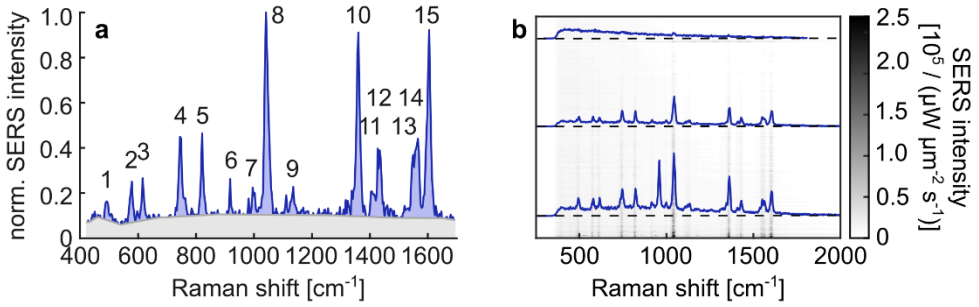

Figure 4.7 ***Characteristic single-spot SERS spectra of 2-naphthalenethiol****. a) One single-spot spectrum measured at 633 nm on Ag nanospheres resonant at 405 nm. Broad background (grey) is calculated by interpolating signal at Raman-inactive frequencies and subtracted from the total signal to yield SERS signal (blue). Fifteen peaks can be distinguished above the background level. b) 1370 SERS spectra recorded at 781 nm on Au nanorod resonant at 780 nm, plotted as an intensity map where each horizontal line corresponds to a single spectrum. The spectra are sorted by the SERS to background ratio and the 10th, 50th and 90th percentile spectra are also plotted on top (blue) to highlight the SBR range within the sample.*

Recording SERS spectra one spot at a time allows sorting and thresholding the data to gain a deeper insight into the sample distribution as well as to reject poorly performing nanoparticles. The latter ability makes this setup robust against sample contamination making it suitable not only for nanoparticle screening, but also for measurements on “real” samples. Figure 4.7b shows an example measurement set recorded at 781 nm illumination on Au NR 780. The 1370 single-spot SERS spectra are plotted as an intensity map. The SERS intensity is normalised to illumination intensity and wavelength-dependence of the setup to allow quantitative comparison among all samples and measurement conditions.

The spectra are sorted by increasing SBR and the top 10th, 50th and 90th percentile spectra are shown in blue. The 10 % of spectra with the lowest SBR are dominated by the broad background with little information about the Raman reporter and can be separated from the healthy spectra for further analysis. Interestingly, probing 1000+ SERS spots of a sample allows us to capture uncommon events such as a disproportionate enhancement of certain Raman bands due to the underlying SERS surface selection rules stemming from some uncommon hotspot geometry (section 2.3.4). For example, the top 10th percentile SBR spectrum in Figure 4.7b features an extremely intense peak 6 compared to the rest of the spectra in the intensity trace.

4.3.2 Sample morphology effects

In section 4.2.2, we outlined how SERS images guide an automated microscope to record single-spot SERS spectral traces. Now, we combine both, the spectral information and the corresponding SERS images to explore the effect of sample morphology on its SERS response. Using silver nanospheres resonant at 405 nm (Ag NS 405), we followed two typical SERS sample preparations use in the literature. In a “drop-dry-drop” method, we deposited the nanoparticle suspension onto a cover slip, let it dry and repeated the process with the Raman reporter solution (Figure 4.8a). For “mix & drop” samples, we mixed the nanoparticles with 2-NT prior to deposition on an oxygen plasma-treated cover slip (Figure 4.8b). Raster-scanning the sample, we recorded ~ 500 SERS images and single-spot spectra for each sample preparation method. After ten weeks, we repeated the measurement on a new mix & drop sample to establish the baseline of random variability in the sample preparation and measurement conditions.

The SERS images in Figure 4.8 consist of 4x4 arrays of randomly-chosen fields of view (each 5x5 µm) for each preparation method. The fibre image corresponding to the spectrum collection region of 1.5 µm diameter is marked in orange. The SERS counts were normalised to the illumination intensity profile and the intensity colour scale is capped at 50 % of the maximum SERS counts to visualise particles of different brightness.

The sample prepared by the drop-dry-drop process shows many closely-spaced bright spots whereas the pre-mixed sample shows sparser SERS spots. These observations are in line with the scanning electron microscope images of plasma-treated and normal cover slip samples (Figure 4.3) showing that the oxygen plasma treatment is crucial for nanoparticle dispersion on the cover slip. Note that for the drop-dry-drop deposition, charging the glass surface is not effective for

dispersing the nanoparticles because they are not bound to the glass after drying and the deposition of the dye solutions redisperses them again and ultimately, they dry in a similar pattern as on an untreated cover slip.

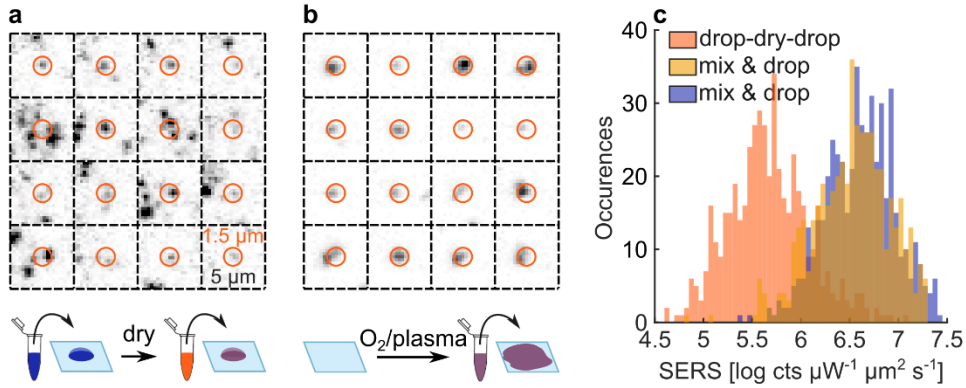

Figure 4.8 ***SERS images and intensity histograms for different sample preparation methods.*** *4 by 4 grids of representative wide-field SERS images of silver nanospheres resonant at 405 nm functionalised with 2-NT by a) sequential deposition procedure and b) functionalisation followed by deposition. c) Background-subtracted SERS intensity distributions from single-spot measurements for the samples in a) and b), and one repeated measurement on a fresh sample as a reproducibility reference.*

To verify the effect of the sample preparation on SERS signal, we plotted the distribution of background-subtracted single-spot SERS intensities (Figure 4.8c) for the drop-dry-drop sample and two mix & drop samples. The counts are plotted on a log scale, because SERS enhancement distributions tend to have a long tail towards high enhancements[133] which is another way of understanding that a few particles in extreme hotspots can contribute to the majority of the bulk SERS counts.[121] The drop-dry-drop sample preparation yields over an order of magnitude lower SERS signal than the, otherwise identical, sample prepared by the mix & drop method. This difference is statistically significant as repeating the same mix & drop measurement 10 weeks later shows matching SERS distributions with only ~ 10% difference between the mode counts.

As such, we have demonstrated that the measurement setup, spectral normalisations and mix & drop sample preparations are reproducible and the mix & drop method yields ~ 10-fold stronger SERS signal than sequential deposition of nanoparticles followed by the Raman molecule. In all subsequent measurements, we use the mix & drop sample preparation. Note that as the difference between the two samples is also obvious from the wide-field images, SERS images without the full spectral resolution are also a useful tool to rapidly screen large areas of the sample and verify its preparation reproducibility prior to the more detailed single-spot measurements.

4.3.3 SERS nanoparticle screening with nanoscale resolution

SERS intensity distributions

To probe the potential of the setup as a SERS nanoparticle screening platform, we examined 10 common nanoparticle types under 2 illumination wavelengths recording over 1000 single-spot SERS traces for each set of conditions (Figure 4.9). We plotted the background-subtracted SERS intensity distributions as violin plots with the illumination wavelengths indicated by the fill transparency and the sample type encoded by colour and labelled at the bottom.

The shapes of the SERS distributions vary across the samples and hence applying a single statistical treatment such as fitting a Gaussian to yield a mean SERS intensity is not suitable for a meaningful comparison. Once again, this underlies the utility of single-spot measurements at a statistically-significant level that yield representative underlying distributions of the measured properties.

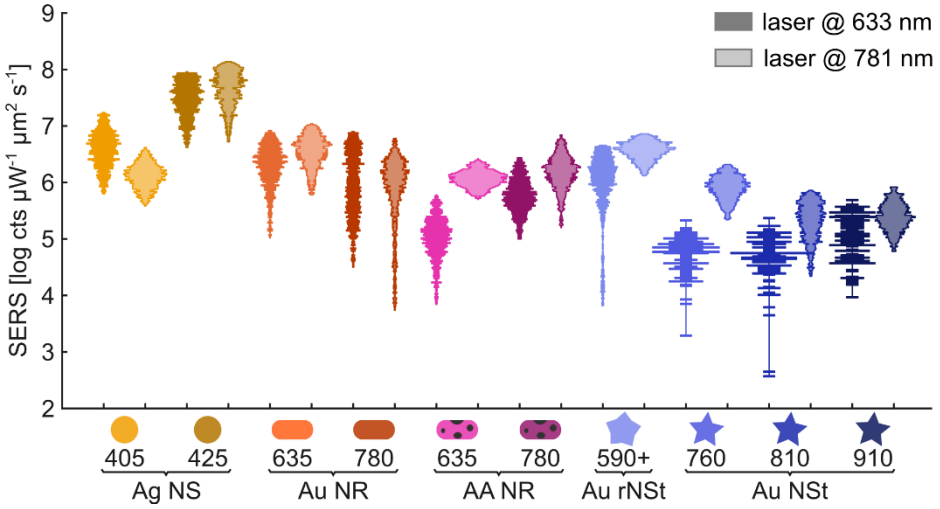

Figure 4.9 ***Single-spot intensity distributions of ten SERS nanoparticles functionalised by 2-NT measured under two illumination wavelengths.*** *Each violin plot is normalised to the same total area and consists of 1000+ measurements, except for Au nanostar samples measured at 633 nm that consist of ~ 100 points. Measurements were sorted by SBR and the lowest 1 % was rejected to avoid long tails of the distribution towards very few particles. The nanoparticle type and corresponding absorption resonance in Milli-Q suspension are marked at the bottom. The measurement wavelength is indicated by the fill transparency. The reported SERS intensities are corrected for wavelength-dependent detection efficiency for quantitative comparison. The real detected counts at 781 nm illumination are ~ 3-times lower.*

The highest SERS intensity is achieved for Ag NSs resonant at 425 nm at both laser wavelengths. Since the spheres are among the least engineered plasmonic shapes with no spikes to benefit from additional electric field concentration,[43,134] their superior performance reports on the superior plasmonic properties of the silver

metal itself (Figure 2.2). It is also interesting that the SERS response is strong far away from the plasmon resonance of the NSs suggesting NS aggregation that redshifts the plasmon.[20] Recall that the measurement (purposefully) pre-selects nanoparticles based on wide-field SERS images, to compare only SERS-active nanoparticles of each sample. Thus, the superior performance of Ag NS 425 at both wavelengths suggests that the sample forms a variety of aggregates where the SERS-images pre-select the most resonant ones for each wavelength. This makes Ag NSs a versatile platform with excellent SERS response and wavelength tuning, although not optimal for quantitative or single-particle SERS measurements.

Among the AA and Au substrates, Au NRs 635 and Au rNSt 590+ give the highest SERS enhancement with the latter sample showing a narrower distribution at 781 nm suggesting a better suitability for sensing applications. Interestingly, this round nanostar performs significantly better than the "pointy" nanostars. The subtle variations in structure (Figure 4.2a) likely explain the dramatic difference in SERS performance. Firstly, the rNSt has a significantly larger core allowing it to engage more electrons in the plasmonic response that is channelled towards the tips.[135] Moreover, the rounder tips actually lead to slightly higher field enhancements than in the pointy nanostars.[120]

Comparing the Aa and Au nanorods, we see that in general they give similar SERS enhancements except for the ~ 10-times lower SERS intensity by AA NRs 635 measured at 633 nm. Since all nanorods here were synthesised using surfactant molecules to achieve the desired aspect ratio, the SERS intensity is influenced by both, the SERS enhancements and the ability of 2-NT molecules to populate the hotspots and hence displace the surfactant. Disentangle the surface chemistry from the plasmonic response goes beyond the scope of this work, but we note this as an important consideration in SERS experiments.

Finally, tuning the laser wavelength to the nanoparticle resonance does not have a dramatic, "all or nothing", influence on their SERS intensities. For nanoparticle resonances blueshifted from the laser, this could be explained by the possibility of resonance redshift due to aggregation. For samples with redshifted resonance with respect to the laser, there is an overall decrease of SERS performance, but the only dramatic decrease occurs for the NSt samples that are known to be highly sensitive to the laser-resonance overlap.[120] The little observed SERS at 633 nm in Figure 4.9 is likely facilitated by plasmonic modes related to the core that are blueshifted and much weaker than the hotspots at the tips.[136]

In summary, the strongest SERS is obtained using Ag NSs thanks to the superior plasmonic properties of silver and likely the ability of the nanoparticles to form a wide range of aggregates with resonances including both 633 and 781 nm. Among all gold nanostars, rNSt shows the highest SERS intensity thanks to stronger plasmonic response facilitated by a large core and rounder tips. All nanoparticle types yield a decent SERS signal at both, 633 and 781 nm, except for Au NSts that are more sensitive to the overlap of the plasmon resonance with the laser to benefit from the strong electric field confinement at the tips.

Peak intensity correlation to the total Stokes signal

Having characterised the nanoscale distributions of the SERS intensity across all samples and wavelengths, we can gain more detailed insight into the sample performance by retrieving a multiparameter correlation from the single-spot measurements. Specifically, we investigate the relationship of background-subtracted SERS intensity of five individual 2-NT SERS bands to the total Stokes detected photons (SERS + broad background) at the Stokes side of the spectrum. This analysis allows us to distinguish subpopulations of nanoparticles with poor SERS performance and gain insight into the heterogeneity of the plasmonic hotspots and nanoantenna-molecule geometry that dictate the particle-to-particle SERS reproducibility, which is crucial for sensing applications. Six examples, each containing 1000+ single-spot measurements are shown in Figure 4.10.

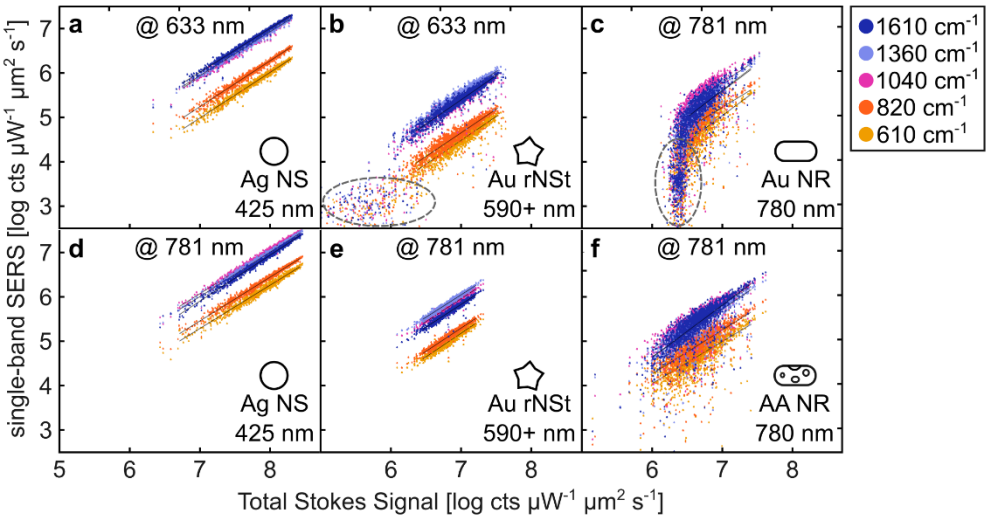

Figure 4.10 ***Single-spot correlations of background-subtracted SERS bands of 2-NT to the total Stokes-shifted signal.*** *Each plot consists of 1000+ measurements where a vertical line across the plot corresponds to one measurement. The laser wavelength is marked at the top of each plot and the nanoparticle type and its resonance in Milli-Q water suspension are indicated at the bottom right. Poorly-performing nanoparticles (grey dashed ellipses) are removed from the linear fits (black lines).*

All plots show a linear dependence of the background-subtracted peak counts on the SERS + background counts as visualised on a double logarithmic scale with a slope of 1. Recall that the broad background in SERS originates from nanoparticle luminescence,[131] electronic Raman scattering,[130] or metal-molecule coupling.[132] All of these processes depend on the plasmonic response of the nanoparticle that also governs the SERS intensity of the molecule at the surface.[20] Thus, the molecular SERS and the broad background intensities are fundamentally coupled and in fact, this limits the maximum achievable signal-to-background ratio in SERS.[132] Note that the fact that the individual peak "lines" are parallel to each other means that the entire SERS spectrum is enhanced equally among different nanoparticles. This is an important parameter for sensing applications where only a part of the Stokes range may be selected for detection.

The SERS to total Stokes signal correlation is also useful to distinguish poor or poorly-functionalised nanoparticles significantly deviating from the fitted lines (Figure 4.10, grey ellipses). These exhibit low SBR and weaker correlation between SERS and the total Stokes signal. Yet, they yield Stokes-shifted signal intensities comparable to healthy particles and are therefore falsely identified as SERS-active nanoparticles in the wide-field SERS images. Typical chemistry-based sensing platforms such as a home pregnancy test have false positive probabilities below 1 %.[137] The false positives in Figure 4.10b and c comprise 10 and 22 % of all measurements, respectively, and thus do not meet the criteria for SERS-based sensors.

Interestingly, false positives occur for measurements where laser wavelength matches the bulk plasmon resonance of the sample (see also long tails towards low SERS in Figure 4.9). This suggests that although the maximum SERS SBR is limited by similar scaling of the SERS signal and the background, the background itself can be enhanced at the plasmon resonance without a matching increase in the molecular SERS. Hence a small spectral offset from the plasmon resonance in SERS measurements may be advantageous to minimise the background and improve the particle-to-particle reproducibility.

Figure 4.10 also gives insight into the distribution of hotspot geometries and their sampling by the 2-NT molecule based on the deviations of the SERS scattering from the fitted lines. Zero deviation from the fit represents a perfect correlation between the total SERS, background and each individual SERS band intensities, hence reporting on the uniformness of the nanoparticle hotspot geometries and the molecule-nanoparticle distance and orientation. This can be seen best by the two NR samples (Figure 4.10c,f), that show a broad distribution of SERS counts for a

given total Stokes signal, except for the highest SERS intensities where the points group very close to the fit line. Consistently, there is a large number of antenna-molecule geometries that can give rise to intermediate SERS intensities, whereas the highest enhancement is only achieved for an ideal molecule position and orientation within the strongest hotspot at the tip of the nanoantenna.

This is further supported by the narrow distribution for the highly-symmetric silver nanospheres that in turn yield highly uniform hotspots. Similarly, the broader distribution for rNSt is measured at the bulk plasmon resonance where many spikes yield sufficient SERS enhancement as opposed to the measurement at 781 nm, which preselects only a fraction of longer spikes with sufficient redshift[138] to support a resonance at the laser wavelength. Hence we conclude for the second time that better repeatability among nanoparticles can be achieved by slight detuning the laser from the bulk plasmon resonance to pre-select a small fraction of hotspots (and nanoparticle-molecule geometries) that yield a strong SERS response.

Finally, to highlight the differences that may appear minor on the log-log plot in Figure 4.10, we plotted the full SERS spectra for the Au rNSt sample (Figure 4.11). The SBR of the average spectrum for the 1040 cm^{-1} peak are ~ 3 and ~ 13 under the 633 and 781 nm illumination, respectively. This would have a dramatic impact of a sensitivity of a SERS sensor where only the molecular SERS signature carries useful information. Similarly, the increased heterogeneity of the SERS hotspots and their occupancy at 633 nm is shown as a high SERS and background variability that strikingly contrasts with the reproducible spectra under the 781 nm illumination that likely pre-select a small fraction of the SERS hotspots.

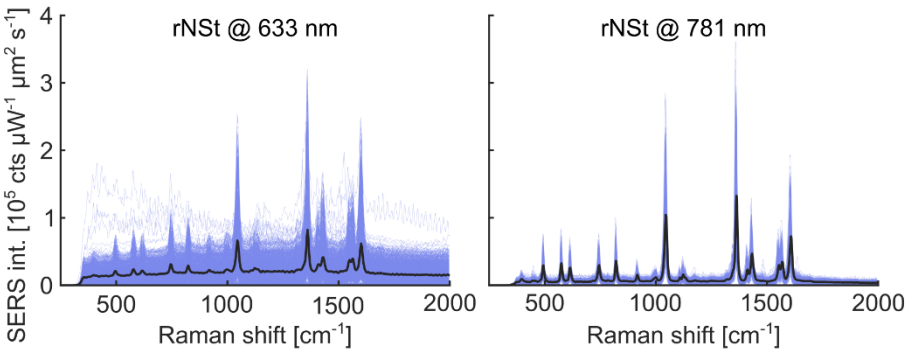

Figure 4.11 ***SERS spectra of round nanostars functionalised with 2-NT from 1000+ single-spot measurements at two illumination wavelengths.***

To summarise, intensities of the molecular SERS and broad background are directly proportional (Figure 4.10, black lines) limiting the maximum achievable SBR in SERS.

The background itself can however completely dominate the spectral response, especially when the laser matches the plasmonic resonance of the nanoparticles. Such single-spot spectra can show sufficient intensity at the Stokes range to be falsely classified as SERS-active nanoparticles. Measuring 1000+ single-spots per sample allows comparing how well the SERS and background intensities are correlated based on the deviations from the fitted lines. Narrow distributions report on homogeneous hotspots such as those formed between the highly-symmetric Ag nanospheres. Interestingly, the datasets for rNSt 590+ show that a slight offset of the laser from the plasmon resonance allows preselecting a fraction of hotspots, yielding a more reproducible SERS response. Therefore, conducting SERS experiments exactly at the plasmon resonance wavelength may counterintuitively decrease SERS performance by increasing the number of false positive identifications and probing a wider range of hotspots.

Temporal stability of the total Stokes signal

In all measurements in this chapter, we recorded a trace of 16 SERS spectra for each bright spot to yield the evolution of the SERS signal in time. The integration time was typically set to 50 ms with an additional processing time of the camera of ~ 30 ms for each spectrum, hence probing a time span over ~ 1.3 s. By taking the % standard deviation of the total detected Stokes counts within the trace of 16 spectra, we obtained the temporal fluctuation of the signal for each single-spot measurement. An example for the rNSts at two illumination wavelengths is shown in Figure 4.12.

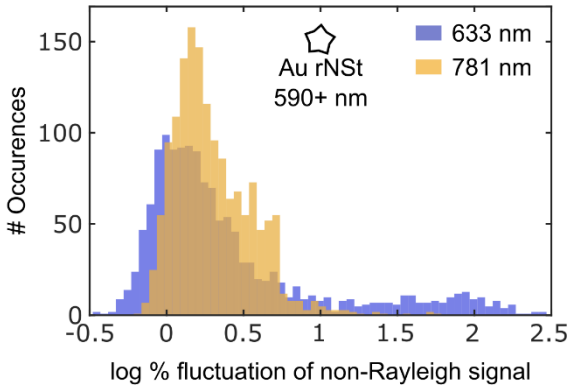

Figure 4.12 ***Temporal fluctuations of the total Stokes signal of round nanostars functionalised with 2-NT measured under 633 and 781 nm illumination.***

As expected for a commonly used SERS nanoparticle and a stable 2-NT Raman reporter, the vast majority of spots shows a stable SERS with less than 10 % (log (% fluct.) = 1) signal fluctuation in time. An exception is a subset of nanoparticles measured at 633 nm that show signal fluctuations sometimes

exceeding the mean counts (log (% fluct.) > 2). Interestingly, these are the same nanoparticles identified as outliers in Figure 4.10b giving the first hint on correlations between different parameters: background-dominated SERS is accompanied by extremely high signal fluctuation suggesting an origin from a metastable hotspot configuration. This is most likely caused by fluctuations of the dominant background characteristic for single gold nanoparticle luminescence[139] and is also consistent with the increase probability under resonant laser illumination.

4.3.4 Holistic nanoscale insight into SERS properties

So far, we have evaluated the SERS intensity, hotspot reproducibility among individual nanoparticles, SBR (by variation of peak and total Stokes counts), temporal stability of the SERS signal and fraction of falsely-identified SERS spots. Now, we combine all of the above parameters in a holistic evaluation of a selected subset of nanoparticles to gain deeper insight into the interplay of the individual metrics for SERS sensing suitability (Figure 4.13).

All single-spot distributions in Figure 4.13 were recorded at 781 nm and plotted such that values away from the centre represent good properties for SERS sensing. This allows a quick multiparameter comparison among the samples. The four sample examples were chosen as top-performing representatives of each nanoparticle geometry and the overall best among them is the Ag NS sample followed by Au rNSt. The AuNR and Au NSt perform poorly due to large variability and low SBR, respectively. Note that in a bulk measurement, the good rNSt and poor Au NR would give similar SERS intensity and SBR and would therefore incorrectly appear as similarly suitable SERS substrates.

Even more interestingly, the plot in Figure 4.13 allows finding connections between individual SERS parameters that can drive intelligent design of better nanoparticles. Firstly, the SBR is inversely correlated to the fraction of true positives as the two follow exactly opposite trends. For Stokes-signal preselection of spots, background-dominated nanoparticles still yield sufficient signal to incorrectly qualify as 2-NT functionalised SERS-active cases. Thus, background minimisation is a priority for good nanoparticle design. Secondly, a wide distribution of hotspot geometries (and occupancy) is linked to lower temporal stability that can be explained by lower stability of randomly-formed hotspots. For example, the activation energy of surface atom movement in gold is only ~ 0.9 eV,[140] and thus laser-induced hotspot rearrangement is likely for randomly-formed metastable geometries.

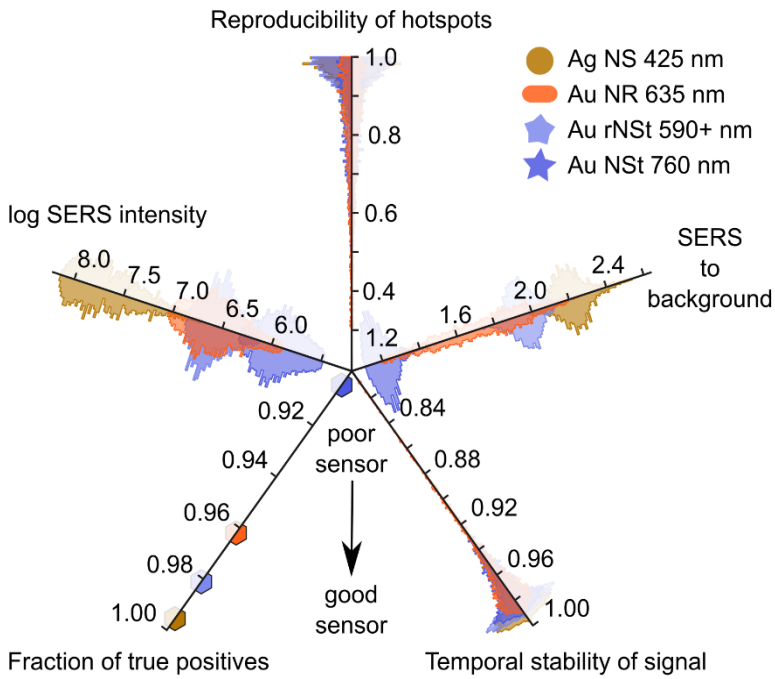

Figure 4.13 ***Multi-parameter comparison of four nanoparticle types functionalised with 2-NT.*** *Each dataset comprises 1000+ single-spot spectra measured under 781 nm illumination. The SERS intensity shows background-subtracted counts as reported in Figure 4.9. The hotspot reproducibility is shown as 1 – hotspot heterogeneity obtained as the relative standard deviation from the fit line (as in Figure 4.10) such that 1 marks perfect correlation of SERS and the background. The SBR was calculated as the ratio of the SERS intensity of the 15 Raman peaks to the broad background (as shown in Figure 4.7a). The temporal stability was obtained as 1 – fluctuations evaluated as relative standard deviations of the total Stokes counts (Figure 4.12). Lastly, the fraction of true positives was calculated as the number of measurements yielding SERS peak counts associated to the correlation lines (points outside grey circles in Figure 4.10) divided by the total number of measurements. The false positives were removed from the histogram plots.*

Here, the hotspot reproducibility and SERS stability are relatively high because we study well-established SERS nanoparticles with a stable 2-NT reporter covalently linked to the metal. However, the hotspot variability and temporal stability relationship would be an especially useful indicator to evaluate strategies aiming to improve the reproducibility of SERS to enable quantitative single-particle sensing. For example, a newly developed sensor made of a metallic nanoparticle functionalised with an analyte-specific ligand placed in specific positions within the plasmonic hotspots should yield hotspot homogeneity and temporal stability close to 1. If for example only the latter parameter was lower, it would signify a successful nanoparticle functionalisation with the ligands, but unsuccessful binding of the analyte.

Overall, the multiparameter evaluation enabled by single-spot measurements provides a deep insight into the SERS performance of the nanoparticles by revealing correlations between different parameters. Minimising the broad background is crucial for correct identification of nanoparticles and uniform hotspots and their occupancy facilitate the temporal stability of the signal, likely by avoiding metastable randomly-formed hotspots. This level of understanding can yield much faster convergence towards designing a quantitative SERS architecture than bulk measurements, in which the good Au rNSt and poor Au NR samples would yield similar SERS signatures. In the following section, we drive the experiment one step further and investigate how the SERS properties change between single and multiple particles by pre-selecting the nanoparticles through dark-field scattering images.

4.3.5 SERS variability among single nanoparticles

So far, we referred to the discrete measurements as single-spot, as strictly originating from a bright point on the SERS image that could result from a single up to hundreds of nanoparticles, depending on their size. Here, we adjust the imaging part of the microscope to yield a dark-field (DF) scattering image of the sample (Figure 4.4) that will allow us to classify the SERS spectra based on the number of particles in the collection spot. For nanoparticles much smaller than the wavelength of light, the scattering can be described by the Rayleigh regime where the scattering intensity is proportional to the square of the nanoparticle volume, $I_{DF} \propto V_{NP}^2$.[38] In the visible wavelengths, the maximum nanoparticle dimension for which this regime applies is ~ 100 nm and the Rayleigh (DF) scattering can be used as a very sensitive tool to determine the size of the nanoparticles.[141]

Here, we exploit the V_{NP}^2 scaling of the DF scattering intensity to determine the number of nanoparticles in each single-spot SERS measurement. Firstly, we determine the characteristic scattering signal of single nanoparticles using a control sample where nanoparticle dispersion is guaranteed by surfactant molecules. Then, we repeat the measurement on 2-NT functionalised nanoparticles, use the DF scattering to classify the measurements as originating from single or multiple nanoparticles and compare the SERS response of the two subcategories. As an example, we measured gold nanorods resonant at 635 nm with the 633 nm laser (Figure 4.14).

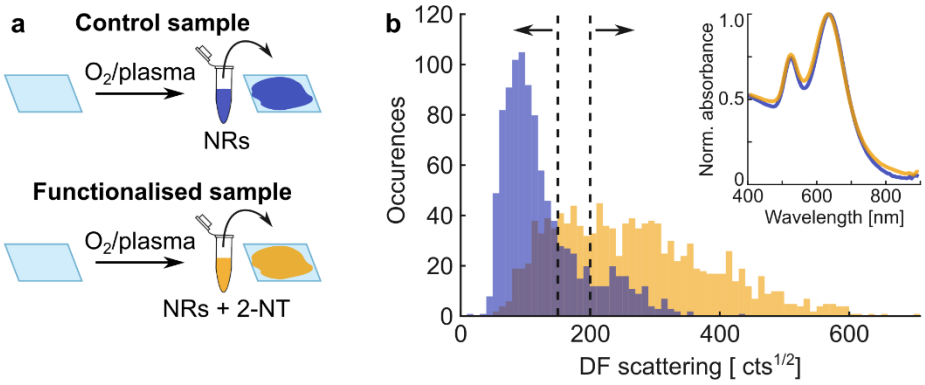

Figure 4.14 ***Dark-field scattering-based discrimination between single and multiple nanoparticles****. a) Sample preparation for a control (bare nanorods) and SERS-active (2-NT functionalised) Au nanorods resonant at 635nm. b) Dark-field scattering distributions of bare (blue) and functionalised (yellow) gold nanorods. Each distribution corresponds to 1000+ single-spot measurements and the vertical lines correspond to thresholds for "single" and "multiple" nanorod identification. The inset shows absorption spectra of the corresponding suspensions measured in a cuvette showing no aggregation (red shift) of the nanorods upon functionalisation with 2-NT.*

The sample was prepared by the "mix & drop" method as in all nanoparticle screening measurements. A control sample of the stock suspension drop-casted as received was also prepared to measure the DF scattering benchmark for single nanorods. This nanorod sample was chosen because the surfactant (Cetrimonium bromide) maintains individual nanoparticles well dispersed in the solution. The dispersion was also confirmed by the absorption spectra of the solution that lack redshifted side bands characteristic for aggregates (Figure 4.14b, inset). Following deposition on the cover slip, we expect the surfactant in the control sample to maintain the nanorods spatially dispersed while for the functionalised sample, we expect a distribution of single and multiple particles as shown in the scanning electron microscopy image of the same sample in Figure 4.3, right.

The DF scattering histograms in Figure 4.14b are plotted as a square root of the counts (DF $cts^{1/2}$), to give an x-axis linear with the nanoparticle volume and hence their number. The control sample (blue) yields a narrow peak centred at 100 DF $cts^{1/2}$ assigned to single-nanoparticle signal with a small sideband at higher DF counts assigned to multiple nanoparticles in the observation spot. Considering 100 DF $cts^{1/2}$ as a typical signal of a single NR, 200 DF $cts^{1/2}$ would correspond to two NRs, 300 DF $cts^{1/2}$ to three NRs and so on. Consistent with the scanning electron microscope image (Figure 4.3b), the functionalised sample (yellow) contains both single and multiple-particles up to ~ 4. To avoid incorrectly assigning borderline cases between single and multiple nanoparticles, we set 150 $cts^{1/2}$ as the upper limit for single nanoparticles and 200 $cts^{1/2}$ as the lower limit for multiple nanoparticles.

Using the single and multiple nanoparticle classification thresholds from the DF data, we sorted the corresponding single-spot SERS datasets measured on the bare and 2-NT functionalised samples to probe whether SERS signal gave insight into the number of nanoparticles in the collection spot. For a deep insight into the interplay of 2-NT specific SERS and total signal, we plotted the intensity of the five brightest 2-NT SERS bands against the total Stokes-shifted signal (Figure 4.15a-d).

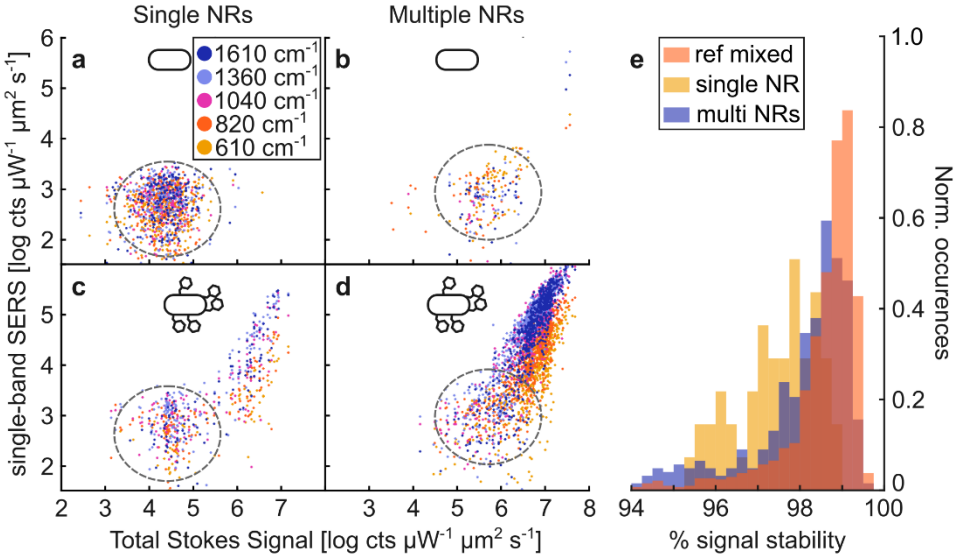

Figure 4.15 ***SERS statistics for single and multiple gold nanorods****. a-d) SERS band intensities plotted against total Stokes-shifted signal for bare nanorods (top) and nanorods functionalised with 2-NT (bottom). e) Distribution of SERS stability in time for SERS-active particles from c) and d) and a reference of an equivalent sample measured in the SERS configuration.*

For the control sample, both single and multiple NRs (Figure 4.15a,b) yield SERS peak intensities of less than 0.01 % of the overall signal. These stem from an integrated noise in the SERS spectra after background subtraction. As expected from a random SERS background, the peak counts are not correlated to the overall signal forming a "blob" (grey ellipses) on the plot. This serves as a reference for the intensity of Stokes emission from the bare nanorods. As a technical sidenote, there are two measurements with significant SERS counts (Figure 4.15b, top right) that likely stem from some contamination. Thus, we can also use this measurement to estimate our contamination level as less than 0.2 %.

In the functionalised sample, both single and multiple nanorods (Figure 4.15c,d) show two SERS populations: low SERS counts uncorrelated to the total Stokes signal (grey circles) and higher SERS counts that increase with the total signal. The former subset can be ascribed to bare nanorods as the SERS intensities match the

corresponding control samples of bare nanorods (Figure 4.15a,b). Note that the increased fraction of measured bare nanorods compared to the screening measurements stems from the particle selection based on DF Rayleigh scattering images instead of Stokes-shifted scattering. The proportion of bare nanorods in the singles subset is ~ 75 % whereas for the multiples it is ~ 25 % pointing to a role of 2-NT in particle aggregation either directly, or by displacing the surfactant molecules.

The most important observation from Figure 4.15 is that both single and multiple NRs within the functionalised sample span a similar range of SERS signal strengths. This exemplifies the challenge to achieve quantitative detection in SERS by directly measuring the ~ 2 orders of magnitude range of peak SERS intensities among single NRs, which is ~ 100 times higher than linear SERS scaling with the number of nanoparticles required for quantitative sensing. In other words, based on the SERS signal, it is not possible to retrieve the number of NRs in the collection spot. This is not surprising as the NR sample was not optimised for quantitative sensing. Recall that the SERS enhancement scales with the fourth power of the electric field inside the hotspot (section 2.3.4). Therefore, an almost atomistic control of hotspots and their occupancy by the Raman reporter must be achieved to minimise the SERS enhancements variations below the linear SERS dependence on the number of nanoparticles required for sensing applications.

Aside from the magnitude of SERS, we also verified whether it was possible to infer the number of NRs based on increased signal fluctuations in single NRs where fewer molecules contribute to the SERS signal. Recall that for each spot we record 16 SERS spectra and calculate the temporal stability of the Stokes emission as 1 – the relative standard deviation of Stokes counts. We plotted the temporal stability distributions for the single and multiple nanoparticle subsets in Figure 4.15c and d and an equivalent sample of mixed singles and multiples recorded in the nanoparticle screening configuration as a reference (Figure 4.15e). All samples show emission stability over 95 % for over 90% of the measured spots and therefore, the stabilities lie too close to each other to serve as a useful parameter to discriminate single nanoparticles. This high stability is likely thanks to the covalent link between the Au NR and the 2-NT molecule and hence for SERS platforms based on weaker nanoparticle-molecule bonding, this analysis could perhaps yield more insight into the number of nanoparticles probed at a time.

Lastly, we note that lowering (increasing) the scattering threshold for single (multiple) NR identification (see Figure 4.14) gives equivalent observations to those

presented above: both single and multiple NRs yield similar SERS intensities spanning across ~ 2 orders of magnitude and similar temporal stability > 95 %.

As such, we conclude that for the Au NR 635 sample, the SERS itself does not report on the number of nanoparticles in the collection spot because the variability of SERS enhancements far exceeds the slow linear scaling with the number of nanoparticles. This result illustrates the difficulty to produce SERS enhancements (proportional to the fourth power of the electric field) sufficiently reproducible for quantitative SERS sensing where SERS signal scales linearly with the number of nanoparticles or analyte molecules. Yet, our automated Raman setup with the DF wide-field imaging extension demonstrated its capability to record and sort single-spot SERS spectra based on the number of nanoparticles contributing to the total signal. As such, this platform is suitable to evaluate SERS platforms engineered for quantitative sensing being able to provide a detailed insight thanks to the single-spot measurement approach at a relevant statistical sampling, as well classify the measurements based on the number of nanoparticles in the DF imaging mode. Integrating the DF measurements into the SERS setup instead of analysing the number of nanoparticles by traditional methods such as scanning electron microscopy enormously increases the measurement throughput, prevents sample degradation by electrons and ensures correct assignment of SERS properties to the nanoparticle number. By providing more accurate and faster feedback than the traditional bulk characterisation method our approach can greatly facilitate the iterative optimisation cycle of new SERS platforms for quantitative sensing that can lead to a new generation of sensors with sensitivities theoretically down to a single molecule.

4.4 Conclusions and future outlook

Plasmonic enhancements over 10^{10} enabled single-molecule SERS measurements stimulating research efforts to create ultrasensitive quantitative SERS sensors. The main hurdle towards quantitative SERS is achieving uniform SERS enhancements within the sensor with variations smaller than the linear signal variation reporting on the number of detected events. The SERS nanoparticle optimisation strategies are complicated by imperfect feedback from testing measurements that often includes experiments on bulk samples and computer simulations that may not capture the nanoscale variations among the SERS hotspots.

Our DF-SERS setup is a versatile platform for SERS nanoparticle screening that was tested on ten nanoparticle types under two illumination wavelengths. We obtained a detailed experimental insight into SERS performance of each substrate by recording thousands of single-spot spectra per hour. This single-spot approach allowed us to reveal correlations between the measured parameters such as the SERS intensity, hotspot reproducibility, signal to background ratio, temporal stability of the signal and fraction of falsely-identified SERS spots. We found that for most of the samples, measurements under laser illumination resonant with the nanoparticle yielded higher background contribution leading to increased false positive identification by the automated particle recognition and overall larger heterogeneities among the nanoparticles than off-resonant measurements. This suggests that resonant illumination may counterintuitively be disadvantageous for SERS sensing applications.

Furthermore, a dark-field modification of the wide-field imaging part of the microscope allowed classifying SERS measurements between single and multiple nanoparticles, revealing that for the nanoparticles probed here, the SERS intensity variation among single nanoparticles of over 2 orders of magnitude greatly exceeded the limits required to achieve linear scaling of the SERS intensity with the number of nanoparticles required quantitative sensing. Yet, our setup demonstrated its ability to resolve subtle differences in SERS performance unavailable in traditional bulk measurements with an option to distinguish between single and multiple nanoparticles at a fraction of time and sample damage as in traditional sizing techniques such as scanning electron microscopy.

In the future, our platform could screen SERS substrates under operating conditions to test strategies towards improving the reproducibility of SERS enhancements such as through advanced engineering of nanoparticle geometries or specific analyte-nanoparticle binding through surface functionalisation. By providing fast

and accurate nanoscale feedback, it can accelerate the convergence towards a quantitative sensing platform with respect to the current optimisation cycle that heavily relies on potentially inaccurate simulations and bulk measurements. Moreover, considering the wealth and nanoscale relevance of the information available in our technique, it would be interesting to use it as a training dataset for a neural network to predict SERS performance of new platforms. This machine learning strategy could save experimental time and resources and even reveal new design directions beyond the current trends in the scientific community.[142]

5 Few-molecule SERS Microscopy of Plasmon-induced Reactions in Gold Nanojunctions

Surface plasmons of metallic nanoparticles drive a multitude of processes that can be exploited for next-generation therapeutics, sustainable energy and chemical production. For example, heat generated after plasmon decay due to metallic losses has a potential in cancer treatment, the concentration of electromagnetic radiation into hotspots is being integrated into photovoltaics to increase their absorption efficiency and the field of heterogeneous catalysis is being revolutionised by development of plasmonic nanoreactors. It is difficult to control the plasmonic properties of the nanoantennas to maximise a particular parameter and in the field of plasmonic catalysis, it is often not even clear which is the underlying mechanism: lattice heating versus hot electrons being one of the most discussed topics in the field. Therefore, more detailed insight into molecule-nanoantenna interactions is needed.

Here, we use the automated Raman microscope introduced in chapter 4 to study methylene blue molecules inside a nanoparticle on a mirror cavity. We introduce a new sample assembly method compatible with oil immersion that yields 150-fold increased SERS signal compared to air-immersion configurations reported in literature. We thoroughly characterise the plasmonic resonances and SERS response of the system in the new oil-immersion configuration by linear SERS measurements, dark-field scattering and simulations. We then use pulsed laser to induce a chemical change in the methylene blue molecule that is monitored by its continuous wave SERS response and find two SERS loss regimes: a stepwise moderate SERS loss that stabilises at ~ 50 % and a non-linear regime with a peak power threshold and dependence. Our results indicate that lattice heating can be discarded as a driving mechanism of the observed chemical changes. Moreover, based on the measured peak power dependence, we suggest that spontaneous Raman measurements should be suitable for ultrafast interrogation of plasmonically-induced reactions.

5.1 Introduction

In the previous chapters, we have used plasmonic nanostructures that can boost fluorescence signal to the single-molecule level of extremely dim photosynthetic complexes. We also studied a library of different plasmonic nanoparticles engineered to quench fluorescence completely and give rise to strong and stable surface-enhanced Raman scattering (SERS). In this chapter, we will explore how we can exploit plasmonics to gain fundamental insight into ultrafast dynamics of molecules at metal surfaces. Specifically, we will lay grounds for excited-state time-resolved SERS experiments using a model system composed of methylene blue molecules inside self-assembled gold nanocavities.

Light-driven interactions of molecules with metallic surfaces lie at the heart of nanomedicine, photovoltaics and photocatalysis – the key areas of the next-generation therapeutics, sustainable energy and industry. For example, nanoparticles that convert incident light into heat are being developed for cancer treatment, metallic antennas are being employed to increase efficiency of solar cells and a heterogeneous catalysis is being revolutionised by the development of plasmonic nanoreactors for LED- and Sun-powered catalysis.

Illuminating plasmonic nanostructures starts a cascade of a wide range of physical processes, each suitable for a different practical application (Figure 5.1). Absorption of light followed by thermalisation and heat dissipation are desired for photothermal therapy. Plasmon excitation and energy transfer to an absorber molecule is preferred in solar cells. Catalysis can be driven by concentrating the incident light into sub-wavelength hotspots, light-induced generation of highly energetic charge carriers, heating and others. Fundamental understanding of the nanoscale light-molecule-metal interaction is crucial to engineer these nanoplasmonic systems. Experimentally, this means combining nanoscale resolution and extreme sensitivity to observe one or a few nanoparticles at a time, ultrafast time-resolution to track the system after it interacts with a photon and a spectral resolution to provide insight into the photochemical processes taking place. The associated experimental difficulty is further increased by low stability of plasmonic structures under intense laser irradiation typical for ultrafast time-resolved measurements.

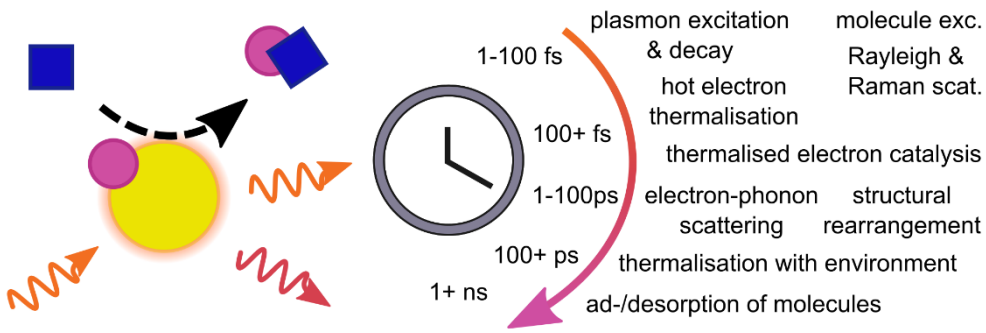

Figure 5.1 ***Schematic representation of evolution of a molecule-nanoantenna system following illumination by a photon.*** *Incoming illumination (orange arrow) launches a plasmon in the nanoparticle that can decay radiatively by scattering, or non-radiatively by absorption followed by heating of the nanoparticle (orange halo). These processes affect molecules adsorbed (pink circle) or diffusing (black arrow) close to the nanoparticle's surface (blue square) by either enhancing the molecular optical signals such as Raman scattering (red arrow) or inducing a chemical change. The typical timescales of the related physical processes are marked on the schematic time axis.*

In the previous chapters, we explored how combining microscopy with plasmonic enhancement allows studying few to a single molecule near plasmonic surfaces at a time. We also showed the advantages of Raman scattering as opposed to fluorescence detection in terms of chemically-rich spectral information and improved stability over time. Here, we take advantage of the ultrafast, picosecond, timescale of the Raman process to get insight into the plasmonic processes contributing to photodamage at high laser powers, paving way to picosecond spontaneous Raman studies at a few-molecule level.

5.1.1 Raman scattering technique choice

Some of the most recently popular Raman techniques to study nanoscopic samples are stimulated Raman scattering and coherent anti-Stokes Raman scattering. These non-linear techniques employ two or more laser pulses with an energy difference matching molecular vibrations of interest to coherently drive these molecular vibrations. By minimising destructive interference of photons due to out-of-phase vibrations, signal enhancements with respect to spontaneous Raman scattering can reach up to 6 orders of magnitude.[143] This is comparable to the lower bound of typical enhancements at metallic surfaces of 10^6 - 10^{10}.

Although non-linear Raman techniques have been successfully combined with SERS,[144] they may not be the most suitable technique to study molecular dynamics at plasmonic interface in general. Firstly, the enhancements with respect to spontaneous SERS are 10^1-10^3 – lower than in bulk Raman.[144] In some cases, a non-linear surface-enhanced Raman process even yielded less signal than

spontaneous SERS.[145] Furthermore, due to the non-linear dependence of signal on laser power, the range of laser powers between the onset of a detectable signal and sample damage tends to be very narrow.[146] The issue of photodamage becomes even more critical for time-resolved and/or excited-state measurements where an additional laser pulse is necessary.

Therefore, we focus on picosecond time-resolved spontaneous Raman spectroscopy that uses a laser pulse to promote a system for example into an excited state and a second pulse to probe the spontaneous Raman scattering from that transient state. In combination with plasmonics, this technique was already used to probe the role of hot electrons and heating in chemical reactions in plasmonic junctions,[147,148] and the influence of orientation of molecules adsorbed on gold on their vibrational population decay.[149] These studies were performed on many plasmonic hotspots at a time and our goal is to push this technique into a single-hotspot and possibly a single-molecule sensitivity to probe ultrafast processes at their fundamental limit.

5.1.2 Plasmonic platform choice

Having selected the most appropriate spectroscopic technique, we are now only missing to carefully choose the plasmonic system itself. In chapter 3, we employed gold nanorods fabricated by electron beam lithography. The antennas had to be hundreds of nanometres long for resonances in the visible and NIR spectrum yielding hotspots with diameters of tens of nanometres depending on the curvature.[150] A typical nanorod yields a 100-1000 nm^3 plasmonic hotspot at either end of the rod (Figure 5.2). Assuming a molecule size of 1 nm^3, a single nanorod can enhance up to 1 000 molecules.

Chemically synthesised metallic nanoparticles such as the ones employed in chapter 4 can reach smaller dimensions resulting in hotspot diameters of a few nanometres. This reduces the maximum number of molecules that fit into a hotspot to approximately a hundred, depending on the molecular size and nanoparticle shape. Note than on top of smaller hotspots, synthesised nanoparticles also yield improved plasmonic response stemming from their crystalline structure.[151]

Bringing two nanoparticles close together creates an even tighter confinement and higher enhancement of the electromagnetic field inside the gap between the nanoparticles (Figure 5.2).[152–154] This effect appears at a particle separation comparable to their diameter and gets more pronounced as the particles approach. The coupling of nanoantennas can be understood as a hybridisation of the plasmonic modes of individual nanoparticles, analogous to the molecular orbital theory in chemistry.[155,156] As the plasmonic modes of the nanoparticles couple, they

form new bonding (redshifted) and anti-bonding (blueshifted) modes. For a simplest example of two nanospheres separated by a small gap, these new modes can be excited with light polarised along the long-axis of the dimer.[157,158]

In addition to more efficient concentration of the incoming illumination, the gapped antennas exhibit extremely high out-coupling efficiencies of 90 %.[159] As the hybridisation occurs even for modes with different symmetry, non-radiative modes such as quadrupoles can couple to a radiative dipole mode of the neighbouring nanoparticle, yielding modes with favourable symmetry for radiative out-coupling.

The main challenge in nanoparticle assemblies is reproducibility[160] because the plasmonic response changes dramatically with the gap distance that typically spans one to few nanometres. In molecular applications, the challenge is exacerbated by the additional step of controlling the position and orientation with respect to the cavity. Existing strategies with sub-nm precision include using DNA origami that bind both nanoparticles and the molecule,[161] or performing electron microscopy on many individual nanoantennas to pre-select structures with the desired gap size.[146,162]

A more elegant approach to reproducibly assemble a gapped nanoantenna is substituting one of the nanoparticles for a flat metallic slab (Figure 5.2). Upon illumination, the remaining nanoparticle induces a “mirror” electric field in the bulk metal, yielding a plasmonic response analogous to that of the nanoparticle dimer. In this nanoparticle-on-a-mirror (NPoM) geometry, the gap can be formed by depositing a thin dielectric layer onto the metallic surface followed by drop casting the nanoparticles. The dielectric spacer is often a self-assembled monolayer of molecules that are then probed spectroscopically. The resulting plasmonic nanojunction is defined with a sub-nm precision, ranging between 1-2 nm depending on the size of the molecules. The plasmonic hotspot spans a few nm^3 hosting typically tens of molecules per NPoM. Note that using the bulk “mirror” as opposed to two nanoparticles also improves heat dissipation of the system, reducing sample photodegradation at higher laser fluences. Overall, the NPoM platform yields a highly-reproducible nanojunction with well-defined and extremely small hotspots ideally-suited to study fundamental molecular processes under extreme plasmonic enhancement.

To further reduce the number of simultaneously enhanced molecules by a single NPoM, a guest-host chemistry can be used within the dielectric layer (Figure 5.2). Specifically, cucurbituril molecules are macrocycles capable of encapsulating smaller molecules.[163] These atomically-defined molecular “buckets” contain carbonyl groups with a partial negative charge that also bind to the metallic surfaces

of both, the nanoparticle and the mirror. An NPoM with a cucurbituril spacer therefore contains a gap given by the height of the bucket, 0.9 nm, and a maximum of 10-20 reporter molecules per hotspot assuming full surface coverage by the cucurbituril molecules (1-2 nm diameter) where each bucket hosts a single reporter molecule. [164] In this chapter, we will investigate a model system composed of methylene blue (MB) dye molecule encapsulated by cucurbit[7]uril (CB7) in a gold NPoM cavity. The MB molecule is an important industrially used dye with additional applications in medicine and cell staining.[165,166] The spectral signatures of MB are thus well known.[167–169] Moreover, MB has an electronic transition resonant with the HeNe laser allowing to probe both resonant and off-resonant behaviour with the common laser wavelengths of 633 and 785 nm, respectively. Overall, these features make the MB-CB7 system within the NPoM cavity a suitable model system to study ultrafast plasmonic effects on few molecules at a time.

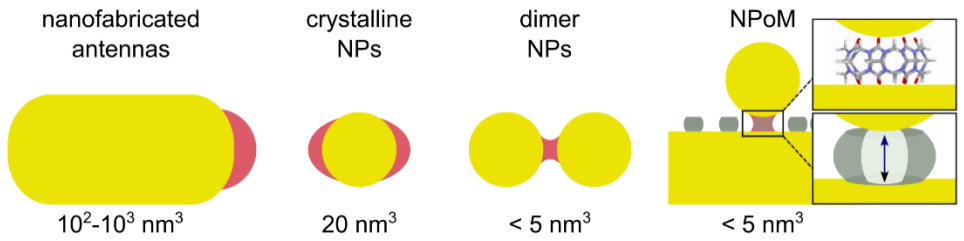

Figure 5.2 ***Various nanoantenna geometries and their typical hotspot volumes****. Top-down nanofabricated antennas yield large hotspots as their minimum size is dictated by the precision of lithography machines. Bottom-up synthesised nanoparticles support smaller hotspots that can be further reduced by employing a dimer configuration. A dimer-like configuration is also achieved by replacing one of the nanoparticles with a "mirror" where the spacing between the two metals is controlled by a molecular "bucket" (cucurbituril, grey) that hosts a Raman reporter molecule in a specific orientation with respect to the plasmonic nanoantenna (methylene blue, blue arrow).*

In summary, we will investigate methylene blue molecules coupled to the NPoM nanoantenna by CW and picosecond SERS to elucidate photochemical processes at the molecule-metal interface. Our results will lay grounds for picosecond spontaneous Raman at a few-molecule limit as well as open new exciting possibilities for driving chemical reactions by consecutive vibrational excitations and multi-photon physics in extreme electric fields generated inside the NPoM hotspot.

5.2 Methods

5.2.1 Sample preparation

Glass cover slips were sonicated in acetone (15 min), Milli-Q water (15 min) and blown dry by nitrogen gas. Titanium adhesion layer (3 nm) was deposited on the cover slip by electron-beam evaporation followed by a gold layer evaporated thermally (70 nm, 0.5 Å/s; PRO Line PVD 75, Kurt J. Lesker) by Saurabh Borkar at ICFO. These gold cover slips were used without further cleaning as the "mirror" substrate of the nanoparticle on a mirror samples. The roughness of the gold surface was 2 nm as measured by an atomic force microscope.

Cucurbit[7]uril and methylene blue powders were purchased from Merck. Stock solutions of CB7 (1 mM in Milli-Q water) and MB (1 mM in Milli-Q water) were prepared monthly to avoid contamination. Note that for a complete dissolution of CB7 in Milli-Q water, the solution was sonicated for a few seconds and used earliest on the following day. Incubation solutions were prepared weekly by diluting each stock solution 10 times and mixing them in a 1:1 ratio. The combined solution was sonicated (5 min) to ensure MB encapsulation by the CB7 host molecule. This incubation solution (500 µL) was dropped onto a gold cover slip and left overnight (16-24 h). The cover slip was then rinsed with Milli-Q water and dried by nitrogen gas. Gold nanoparticle solutions (BBI solutions, OD 1) were diluted in Milli-Q water 100 times and dropped (500 µL) onto the functionalised gold cover slide (5 min). Excess nanoparticles were rinsed off by Milli-Q water and the sample dried by nitrogen gas giving rise to a nanoparticle on a mirror sample.

For high NA measurements, an additional glass cover slip was cleaned by the same method as for gold evaporation. A drop of immersion oil (type F, Leica) was deposited on a glass cover slip that was then placed on top of the functionalised gold mirror creating a "sandwich" with a thin layer of immersion oil between the glass and the gold surfaces (Figure 5.3).

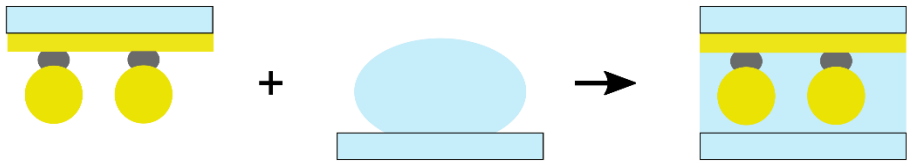

Figure 5.3 ***NPoM sample assembly for oil-immersion measurements.*** *An NPoM sample is prepared by self-assembly and dried. A small drop of microscopy immersion oil is deposited on another cover slip matching the objective specifications and placed on top of the dry NPoM sample. By capillary action, the oil creates an even thin layer across the entire cover slip.*

5.2.2 Simulations

To gain maximum insight from the experimental data, it must be interpreted within a detailed understanding of the plasmonic properties of the NPoM system. Since the oil-immersion configuration employed in this work has, to our knowledge, not been reported in literature, we characterised it using finite-difference time-domain (FDTD) simulations. Specifically, we retrieved the plasmon resonances and near-field maps of the electric field enhancement that allowed us to estimate the maximum number of MB molecules probed inside one NPoM hotspot and the specific cavity modes that participate in the plasmonic response under the measurement conditions used here.

Mie theory benchmark

The FDTD simulations were performed in the Lumerical software. The simulation parameters were firstly benchmarked using gold spheres of 40-80 nm diameters. The dielectric function of gold was chosen to match the experimental values measured by Johnson and Christy[170] and the refractive index of the simulation was set to 1.51 to match the type F microscopy immersion oil used in the experiment. The structures were illuminated using a total-field scattered-field (TFSF) source spanning 600-800 nm (grey box, Figure 5.4a). Absorption and scattering cross-sections were calculated using "box" monitors placed inside and outside the source borders, respectively (orange boxes, Figure 5.4a). Reference cross-sections were calculated using the Mie theory and the comparison for the 40 and 80 nm gold nanoparticles in plotted in Figure 5.4b,c.

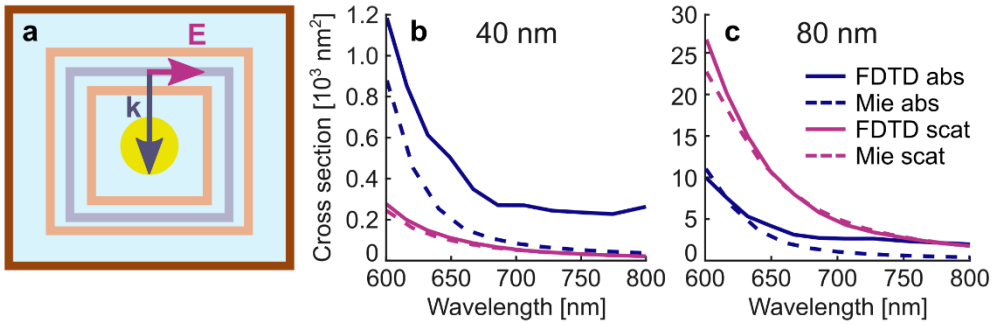

Figure 5.4 ***Benchmark of simulation parameters for a gold nanosphere in immersion oil****. a) Schematic setup of the simulation. b) 40 nm and c) 80 nm nanoparticle absorption and scattering cross-sections calculated using the finite-difference time-domain simulation and Mie theory.*

The FDTD results follow the cross-section trends calculated using the Mie theory. Both cross-sections increase with increasing nanoparticle diameter and the scattering process is more efficient for larger nanoparticles. The FDTD simulation overestimates the absorption cross-section at longer wavelengths and with decreasing nanoparticle diameter. This deviation is likely comparable to the sample

heterogeneity stemming from the distribution of the nanoparticle radii, surface roughness of the mirror and nanoparticle faceting and thus we do not allocate more computational resources to increase the simulation precision.

NPoM under experimental conditions

Moving on to modelling the NPoM sample, we added a 70 nm thick infinite gold mirror separated from the nanoparticle by a 0.9 nm gap matching the height of a CB7 molecule (Figure 5.5). No additional dielectric spacer was added to represent the molecules inside the gap as their refractive index is similar to that of the immersion oil.[164,171]

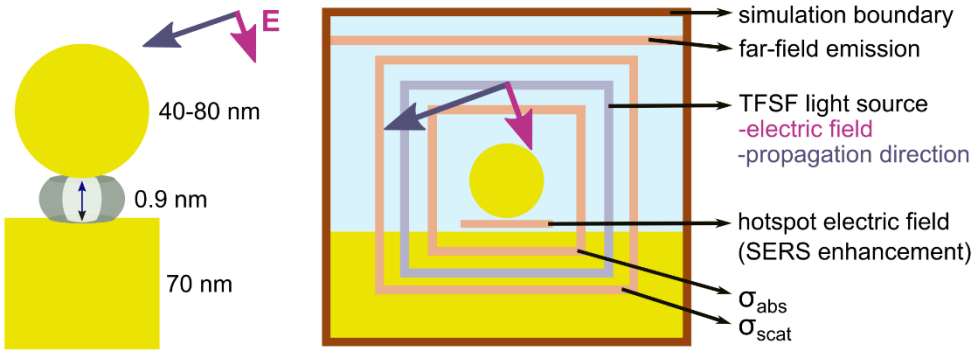

Figure 5.5 ***Schematic representation of an FDTD simulation of an NPoM****. The nanojunction is illuminated by a plane wave propagating at a 70 ° angle (grey arrow) with the electric field (purple arrow) oscillating along the long axis of the NPoM (p-polarisation). The orange rectangles and lines are "box" and planar simulation monitors, respectively, recording the electric field distribution used to extract the plasmonic properties indicated on the right.*

The main challenge to simulate the NPoM geometry lies in the requirement to resolve the electromagnetic propagation inside the gap at a reasonable computational cost. Therefore, simulation parameters from the benchmark example were used as a starting point and convergence tests were carefully performed on all relevant simulation parameters to identify the least computationally expensive setup that captured the underlying physics of the system. The most important parameters were the mesh size in the gap region of 0.15 nm vertically and 0.5 nm horizontally and the meshing algorithm affecting the gold-dielectric boundary set to conformal variant 1.

Absorption and scattering cross-sections at the experimental illumination wavelengths (633 nm and 785 nm) were simulated as before using the TFSF source. The illumination angle was changed to 70 ° with respect to the gold mirror surface normal. This represents the experimental configuration achieved by focusing the illumination light close to the edge of the back focal plane of the oil-immersion objective (NA 1.49, consider effective NA 1.42). The high incidence angle was chosen

to efficiently couple to the bonding dipole mode of the cavity by maximising the electric field component along the long axis of the NPoM.

Additional 2D monitors intersecting the centre of the gap allowed extracting the electric field distribution in the NPoM hotspot. Electric field enhancement maps were then calculated by normalising the electric field profiles to a reference simulation without the nanoparticle, $E_{enhancement} = E_{NPoM}/E_{ref}$. The hotspot diameter was calculated as the FWHM of the electric field intensity at the centre of the gap, also normalised to the reference simulation without the nanoparticle $d_{hotspot} = FWHM(|E|^2/|E_0|^2)$.

Resonance spectra

To determine the wavelength dependence of NPoM absorption and scattering cross-sections and enhancement, additional simulations were run across a range of ~ 500-1000 nm. The TFSF source is setup within the Lumerical software such that a combination of a non-normal incidence and multiple wavelengths yields simulation artifacts (Figure 5.6).[172] Specifically, the simulation keeps constant the k-vector component within the light injection plane for all wavelengths. Therefore, the actual injection angle must be varied for different wavelengths to yield the correct k-vector. For example, the user can select a 500-800 nm broadband source injected at 70 °, but only the 650 nm wavelength component will actually follow the user-selected incidence angle.

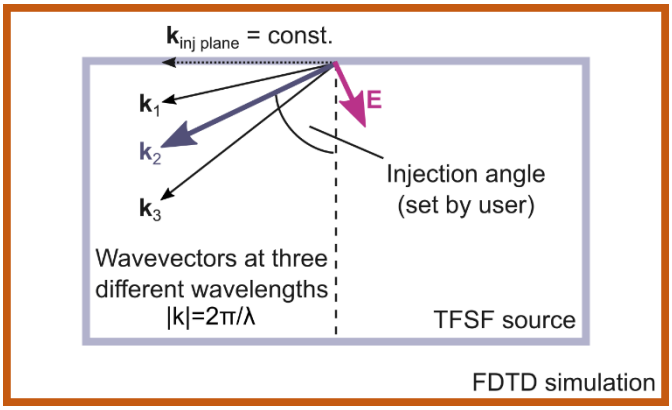

Figure 5.6 ***Lumerical software handling of injection angles for broadband total-field scatterred-field sources at a a non-normal incidence.***

The issue is exacerbated at increasing incidence angles yielding severe artifacts at 70 ° already within a few-nanometre wavelength change. Theoretically, it is possible to circumvent this issue by running multiple single-wavelength simulations (Figure 5.7, solid line). For a 500-1000 nm wavelength with 20 nm steps, 26 NPoM and an equal number of reference simulations are needed. At a sufficient resolution to

capture the gap-related physics, this takes approximately 500 + 150 simulation hours, which is highly impractical.

Noting that a 70 ° incidence is a combination of a 0 ° and 90 ° illumination, we ran broadband simulations at the two orthogonal incidences finding that the 70 ° simulations matched the 90 ° incidence with a small contribution from the normal incidence (Figure 5.7). Although the TFSF source typically does not support the 90 ° geometry, this benchmark shows it is appropriate to use for the NPoM system and in our case, yields over a 25-fold shorter simulation time. Therefore, while maintaining the experimental setup to yield quantitative properties of NPoMs at the 633 nm and 785 nm, all wavelength dependencies, in other words resonances, were simulated using the broadband approach outlined in Figure 5.7.

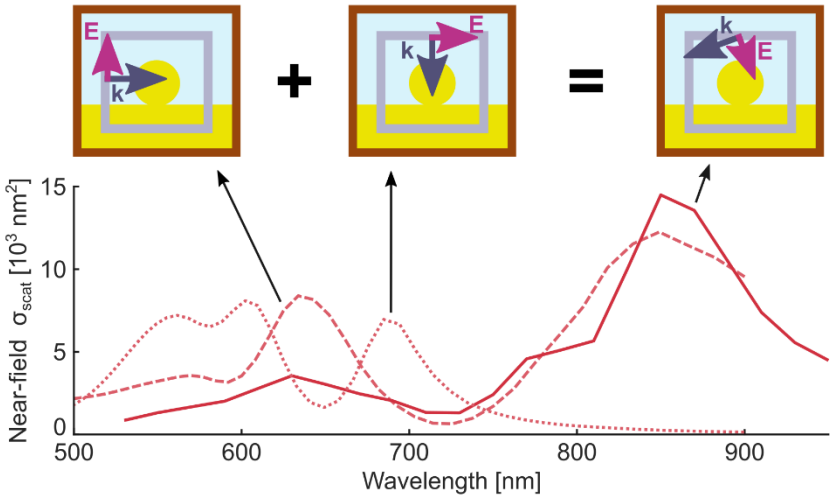

Figure 5.7 ***Near-field scattering cross-section of a 60 nm NPoM*** *calculated from an FDTD simulation as 22 single-wavelength simulations at 70 ° incidence matching the experimental configuration (solid line) and a single broadband simulation at a normal (dotted line) and 90 ° incidence (dashed line). The resonance positions simulated at the steep angle are well-reproduced by the 90 ° incidence simulation with a small contribution of the normal incidence simulation.*

5.2.3 SERS measurements

SERS spectra were measured on the custom Raman setup described in chapter 4. We briefly repeat the main features here and provide detailed description of new modifications for pulsed laser illumination and air-objective configuration.

SERS measurements under CW illumination were carried out with a HeNe laser cleaned up with a 633/10 bandpass filter (ThorLabs). A polariser (LPVIS050, ThorLabs) and a λ/2 waveplate (AHWP05M-630, ThorLabs) were used to align the electric field along the NPoM cavity long axis to maximise the SERS signal.

Pulsed illumination was generated by a Ti:Sapphire laser tuned to 785 nm (Mira, Coherent) pumped by a green diode laser (Verdi, Coherent). For pulsed measurements at 633 nm, the laser was tuned to 633 nm using an optical parametric oscillator (OPO, Inspire HF 100, Radiantis) and then spectrally filtered to a 10 cm^{-1} bandwidth using a grating stretcher and a mechanical slit. The narrowband pulsed light at 633 nm was then recombined with the CW path using a 50:50 beamsplitter cube (BS013, Thorlabs).

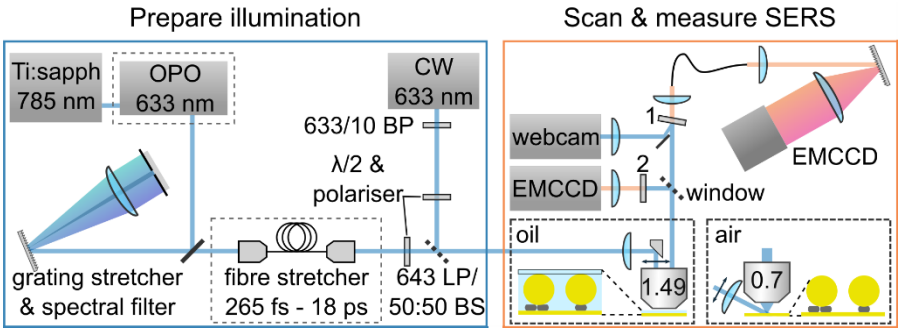

Figure 5.8 ***Experimental setup for SERS measurements****. The CW illumination is generated by a HeNe laser. Pulsed illumination is generated by a diode-pumped Ti:Sapphire laser and either tuned to a narrowband 633 nm light or chirped between 265 fs and 18 ps at full bandwidth at 785 nm. All light passes through a polariser and a λ/2 waveplate to ensure p-polarisation at the sample. For air configuration, the light is focused onto the sample by a lens and collected by an air objective. Otherwise, the light is focused onto the edge of the back-focal plane of an oil-immersion objective and collected using the same objective. The collected light in both cases is split between an EMCCD camera recording a SERS image of the sample (2: 647 LP + 692/40 BP or 808 LP + 832/37) and the fibre-coupled spectrometer recording SERS spectra (1: 2x 633 notch or 2x 785 notch). The reflection from filters 1 is focused on a webcam for autofocusing.*

For pulse duration-dependent measurements at 785 nm, the output of the Ti:Sapphire laser was sent directly onto the grating stretcher without the mechanical slit. By varying the grating distance from the lens and the back mirror, the laser pulses were chirped and hence compressed or stretched in time. Additional chirp could be added by propagating the light through a single mode fibre ("fibre stretcher"), yielding 265 fs – 18 ps pulse lengths as measured by an autocorrelator (Pulse Check, APE). This light was then sent through a set of a polariser (LPVIS050, ThorLabs) and a λ/2 waveplate (AHWP05M-950, ThorLabs) to ensure p-polarisation at the sample (along the long axis of the NPoM) and recombined with the CW path using a dichroic beamsplitter (F48-643, AHF Analysentechnik).

In all configurations, linearly polarised light was sent to the SERS microscope aligned along the long axis of the NPoM (double-headed arrows, Figure 5.8). For the benchmarking measurements in air, light was focused onto the sample in a dark-field fashion by a 50 mm lens placed at an angle to maximise the electric

polarisation component perpendicular to the mirror. The SERS photons were collected by an NA 0.7 objective (MY100X-806, Mitutoyo). In an oil-immersion configuration, the incoming light was focused onto the edge of the back focal plane of an NA 1.49 TIRF objective (APON 60XOTIRF, Olympus) by translating a rod mirror away from the centre of the objective just before the light intensity after the objective started decreasing. This yielded a wide-field high-angle illumination at ~ 70 ° capable of more efficient coupling to the longitudinal mode of the NPoM cavity than a confocal illumination where only a fraction of the light hit the sample at high angles. The scattered light was collected by the same objective.

The detection part of the setup is identical to the configuration in chapter 4. The collected light was split by a window directing ~ 5 % onto an EMCCD to yield a wide-field SERS image of the sample. The ~ 95 % of the light was sent into a fibre-coupled spectrometer coupled to an EMCCD camera. The fibre served as a pinhole corresponding to a 1.5 µm diameter spot on the sample which, with a sufficiently sparse coverage, selected a single NPoM at a time.

The sample was mounted on a 2D motorised translation stage for raster scanning and a piezoelectric stage to maintain a constant sample-objective distance. A focusing feedback loop for oil-immersion measurements was based on a lateral displacement of back-reflected light focused onto a webcam. The setup was then able to automatically raster-scan the sample recording a SERS image, identifying bright SERS spots within the image, randomly selecting and placing one of the spots into the fibre collection region and recording a trace of SERS spectra. Only one particle was measured per field of view to avoid modifying the sample by long laser exposure prior to the measurement. Approximately 1000 NPoMs spectral traces were measured per hour, depending on the length of the trace.

5.2.4 SERS spectra analysis

The spectral calibration and normalisation were also described in detail in chapter 4. Briefly, the wavelength axis of the spectrometer was calibrated using a mercury argon calibration lamp. Wavelength-dependent scaling factor of the instrument response was obtained from instrument specifications of the camera quantum efficiency, grating efficiency and objective transmission.

An interference pattern, etaloning, superimposed onto the SERS spectra due to back-reflection of unabsorbed photons from the camera detector was also removed by data post processing. A broad spectrum of a tungsten-halogen lamp was recorded and used to divide the real lamp spectrum without interference fringes. This correction curve was then scaled to the same average as the

specifications-based efficiency curve and then used to multiply the SERS spectra to give etaloning- and detection efficiency-corrected SERS spectra. Although the utility of the etaloning correction to smoothen out broad SERS background was already showed in chapter 4, here we underline its absolute necessity for systems with poor SERS to background ratio.

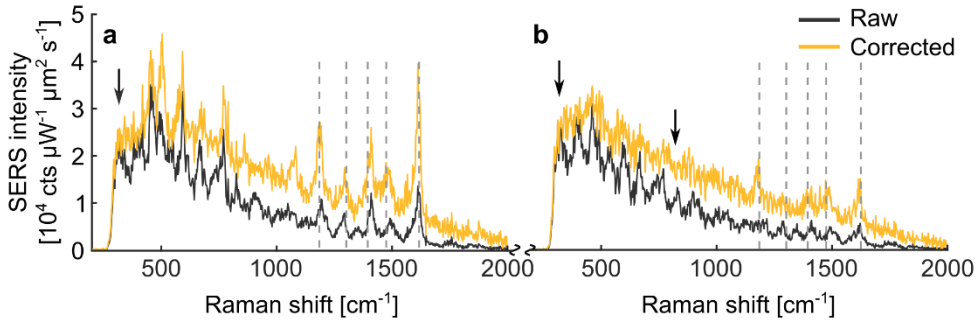

Figure 5.9 ***Example SERS spectra of 80 nm NPoMs under 785 nm illumination*** *showing an NPoM with a) strong SERS signature and b) background-dominated signal. Fingerprint region Raman peaks of MB (dashed lines) are difficult to distinguish from the etaloning fringes without the correction in b). The correction curve also removes artificial peaks due to etaloning (black arrows).*

Figure 5.9 shows two SERS spectra of single NPoMs functionalised with MB: one with high SERS-to-background ratio (a) and one with a strong background and weak MB SERS (b). In the wavenumber region below ~ 1000 cm^{-1}, the background is the strongest resulting in highest signal modulation due to etaloning and appearance of artifact peaks (black arrows). In the fingerprint Raman region, etaloning correction is only necessary to capture the correct amplitude of MB Raman peaks in strong SERS spectrum, whereas it is crucial to correctly identify SERS peaks in the spectrum dominated by background.

Background subtraction

Due to high variability of the background baselines and SERS bursts characteristic for single-particle SERS, the background-subtracted SERS was obtained by summing the SERS counts across each peak and subtracting the signal at slightly higher and lower Raman shift averaged over the same number of wavenumbers as the SERS band (Figure 5.10). This is equivalent to a linear interpolation of the background for each peak based on the signal on either side of the SERS band. As opposed to typical Raman background subtraction such as fitting a polynomial function to the background, our approach is robust with respect to intensity bursts and can be used for noisy spectra such as the non-resonant SERS under 785 nm illumination.

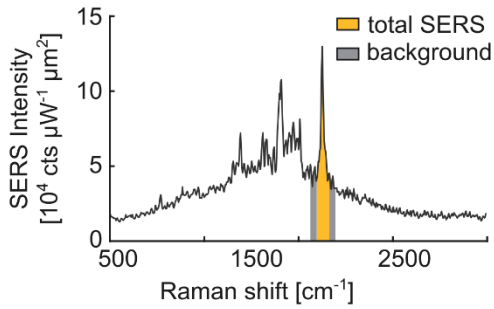

Figure 5.10 ***Example SERS background subtraction for MB C=C stretch at 1625 cm^{-1}.*** *Total counts within the SERS band are integrated and background counts across half the bandwidth on either side are subtracted. This approach is robust with respect to fluctuations of the SERS baseline and poor signal-to-SERS background.*

5.3 Results

5.3.1 Oil immersion for efficient in- and out-coupling

The linear optical response of the NPoM system has been well-characterised already.[173–177] Hence we can benchmark our microscope against the literature. Typical aromatic C=C SERS intensity from a self-assembled monolayer of thiols inside a 40 nm NPoM is ~ 10 counts μW^{-1} s^{-1}.[176,178,179] Using the same illumination wavelength, 633 nm, and a similar setup (air objective with a similar NA, the same spectrometer camera etc.), we detect ~ 500 times higher counts (Figure 5.11a), consistent with an additional SERS enhancement due to the electronic resonance of MB with the laser.

A control sample of CB7 without MB does not show any detectable Raman signal except for a very small number of NPoMs that give a weak Stokes-shifted signal dominated by a broad background (Figure 5.11a, grey). These NPoMs are distributed much more sparsely than in a normal MB sample suggesting the signal originates from some rare contamination rather than CB7 itself. Moreover, the SERS and Raman spectra of CB7 in literature show only two dominant bands in the fingerprint region at ~ 455 and 825 cm^{-1}, corresponding to "ring scissor" and "ring deformation" modes, respectively.[180] Although the lower frequency mode lies close to a ~ 450 cm^{-1} C-N-C skeletal deformation of MB,[167] there are no significant SERS bands of MB in the 800-850 cm^{-1} region. Thus, an absence of a sharp SERS feature in this region provides an additional proof that the SERS signal observed under experimental conditions used here reports on the MB molecules inside the nanojunction.

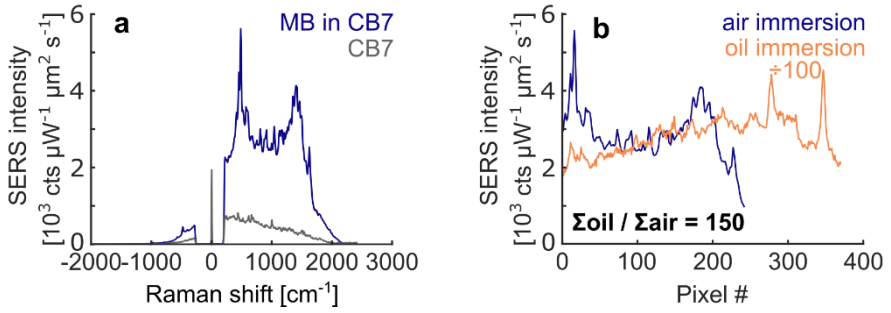

Figure 5.11 ***Raman setup benchmarking for 40 nm NPoMs****. a) SERS spectra in air immersion of MB in CB7 and CB7 only showing that most of the measured SERS originates from the MB molecules. b) MB spectrum from a) plotted against camera pixels and overlaid with a typical MB spectrum measured in the oil configuration. The oil-immersion shows a 150-fold signal increase at the same illumination conditions.*

The lack of detectable CB7 SERS signal at measurement conditions for MB is likely due to two main factors: higher polarizability and additional resonance enhancement of MB. Unlike in CB7, the π-conjugated system of MB can be easily polarised by the incident electric field resulting in a large induced dipole moment and hence strong Raman scattering. Even more importantly, the electronic resonance of CB7 lies in the UV region[181] whereas MB is resonant with the 633 nm illumination used here. The resonance enhancement can increase Raman scattering intensity by several orders of magnitude.[20] Indeed, studies of cucurbituril-guest systems with guest resonance close to the illumination wavelength showed SERS spectra without significant CB7 contribution,[182] whereas for a guest with a resonance in the UV region, the SERS intensities of CB7 and the guest were similar.[183,184]

Having reproduced the air-immersion experiments, we move on to measure the same system in oil-immersion. We covered the sample with a type F microscopy oil and a cover slip (section 5.2.1) and used a 1.49 NA objective for both in- and out-coupling (section 5.2.3). The representative SERS spectra for both configurations are shown in Figure 5.11b. The signal is normalised to the illumination and wavelength-dependence of the setup and the oil-immersion spectrum is scaled down by a factor of 100 for clarity. The two measurements used a different focal length spectrometer lens so the same spectral bandwidth from 400 to 1700 cm^{-1} spans a different number of pixels. Integrating the counts across this bandwidth yields a 150-fold improvement in detected signal for oil-immersion. We attribute this improvement to the higher NA of the system giving rise to a better in-coupling to the cavity dipole thanks to a higher-angle illumination and a higher efficiency of light collection, especially at higher angles.[176] Additional improvement can arise from the change of refractive index surrounding the nanoparticle yielding better far-field out-coupling of higher-order modes.[40] Note that it has been observed that increasing the incidence angle beyond 60 ° reduced SERS out-coupling from an NPoM cavity with a silicon dioxide spacer,[177] but we verified that this was not the case here by monitoring the SERS intensity while varying the incidence angle by scanning the rod mirror across the back-focal plane of the objective.

The 150-fold increase of SERS signal via oil immersion is comparable to the highest improvements achieved by nanofabricating a lens on top of each NPoM[179] at a fraction of experimental difficulty. Furthermore, the increased efficiency of coupling to the cavity lowers the required illumination power and the improved collection allows shorter integration times, both being crucial for ultrafast measurements.

5.3.2 Plasmonic resonances of NPoM cavities

The plasmonic response of the NPoM cavity is strongest at its resonance, which is determined by the nanoparticle size, nanoparticle-mirror separation, refractive index of the dielectric layer in the gap and around the nanoparticle and finally, the shape and orientation of the nanoparticle itself.[40,164,176,185–188] To gain a deeper insight into our results, we performed most of the experiments on four different nanoparticle sizes: 40, 50, 60 and 80 nm. Here, we determine the plasmonic modes of the four NPoM sizes using FDTD simulations combined with dark-field (DF) spectroscopy.

Dark-field scattering in air immersion

Firstly, we measured DF spectra of 40-80 nm NPoMs in an air-immersion configuration, similar to the SERS setup in Figure 5.8. A tungsten-halogen lamp was used as an illumination source at a steep illumination angle where the directly reflected light was outside of the collection cone of the objective. Approximately 300 bright spots were measured one by one for each NPoM size and an example dataset for 60 nm NPoM is plotted in Figure 5.12a. The median scattering maximum is shown above the spectra along with the lower and upper quartile visualised as "error bars".

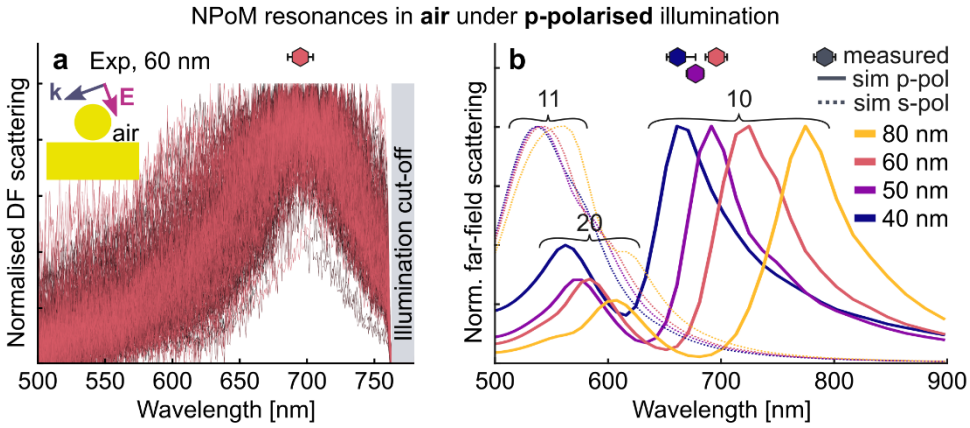

Figure 5.12 ***DF spectra of NPoMs in air.*** *a) Spectra of 300+ 60 nm NPoMs where the median and lower and upper quartile scattering maxima are marked on top. b) Simulated far-field scattering spectra at s- (dotted) and p-polarisations (solid) with measured median scattering maxima plotted on top. The measured resonances agree well with simulations under p-polarised illumination.*

The DF scattering is dominated by a resonance around 700 nm typical for a bonding dipole (10) mode of the 60 nm NPoM cavity in air.[176] This dipole mode can only be excited via the steep angle illumination that provides electric field along the long axis of the NPoM and therefore only appears in the simulations under p-polarisation (Figure 5.12b). Moreover, the corresponding simulated electric field is

centrosymmetric with no radial nodes further confirming the bonding dipolar nature of the mode. An example 2D electric field distribution of the bonding dipole mode in an oil-immersion configuration is shown in Figure 5.14a.

Note that in this work, we use an (ℓm) notation for the NPoM modes, where the indices ℓ and m are related to the number of radial and angular nodes in the electric field distribution in the NPoM gap, respectively.[189] Following this convention and the simulated electric field distributions at the scattering maxima in Figure 5.12b, we assigned the remaining scattering resonances as a bonding quadrupole (20) mode (p-polarisation) and a (11) mode (s-polarisation). Experimentally, the quadrupole (20) mode is not observed, possibly due to its low out-coupling efficiency (chapter 2).[176]

Note that the match between the simulations and experiment could be slightly improved by a systematic variation of multiple parameters that affect the DF scattering such as the gap size, refractive index in the gap, nanoparticle shape and orientation. However, even a few-parameter optimisation requires hundreds of simulations without guaranteeing that convergence to the experimental observation is a result of a more truthful description of the simulated system. For example, increasing the gap size blueshifts the resonance, but deviation of the gold nanoparticle from a spherical shape yields a compensating redshift. Therefore, we employ simulation parameters derived from experimental data, such as the height of the CB7, without additional modifications, which in this case, captures the NPoM physics well.

Dark-field scattering in oil immersion

Having established an agreement among the literature, experiments and the simulations in the air configuration, we are in a position to explore the NPoM resonances in oil where literature data are not available. Measuring DF scattering spectra in the oil-configuration is complicated because the background-free in-coupling from a side of the sample (Figure 5.8, air) is no longer possible due to refractive index mismatch between air and immersion oil. On the other hand, we only need sufficient experimental data for a simulation benchmark. Therefore, we coupled the tungsten-halogen lamp into an existing water-immersion microscope with a spectrally-resolved detection. This setup allowed us to interrogate the sample with minimal optical aberrations thanks to the approximate refractive index match between the immersion oil and water. Importantly, the setup was not optimised for high-angle incidence yielding an s-polarised illumination. By adding a DF mask into the detection, we measured the corresponding DF scattering spectra manually selecting ~ 50 bright spots for each NPoM size.

DF spectra measured for 60 nm NPoMs are plotted in Figure 5.13a. Each spectrum shows three and an occasional fourth peak whose maxima were selected by hand and plotted in Figure 5.13b. The variability of the resonance positions reports on variations in the local environment and size distribution of the NPoMs. It also helps identifying the corresponding plasmonic modes as the lowest energy, (11) mode is expected to shift faster with nanoparticle size variation than the (21) or transverse (T) mode, the latter related to the Au nanoparticle itself.[176,189] Corresponding simulated spectra under s-polarised illumination yield resonances (Figure 5.13c) and electric field distributions (not shown) matching the experimental data and mode assignments. The experimental resonances for the other NPoM sizes are also well-reproduced by the FDTD simulations (Figure 5.13d), thus successfully validating the simulations for the oil-immersion sample configuration.

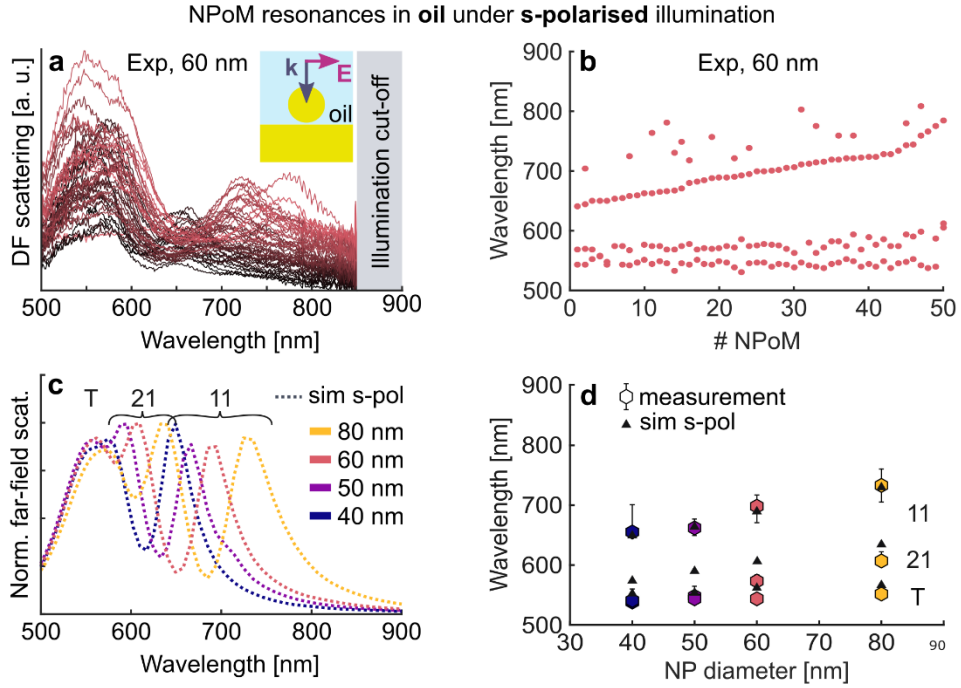

Figure 5.13 ***Dark-field scattering spectra under s-polarised illumination for 40-80 nm NPoMs functionalised with CB7-MB****. a) Measured DF spectra of 50 single 60 nm NPoMs. b) Hand-selected peak maxima of the spectra in a). Some NPoMs show an additional peak at the red end of the spectrum. c) Simulated DF spectra for 40-80 nm NPoMs with the (11), (21) and transverse (T) modes labelled according to the corresponding simulated electric field distribution. d) Measured distributions of DF scattering maxima for 40-80 nm NPoMs. The 50-80 nm datasets comprise 50 single-NPoM measurements each. The 40 nm NPoMs were on the edge of the setup sensitivity and 25 NPoMs were measured, likely oversampling the large edge of the real NP distribution. The vertical bars represent the lower and upper quartiles showing the spread of the individual NPoM resonances. Simulated resonances from c) are overlaid on the same plot for clarity.*

Interestingly, the experimental DF spectra in Figure 5.13a show that the higher-order (21) plasmonic mode is even brighter than the (11) mode in oil-immersion. It has recently been proposed that increasing the refractive index around the NPoM enhanced the retardation effects (phase shift between the incoming radiation and induced plasmon-polariton response) hence increasing the radiative out-coupling efficiency of higher order plasmonic modes.[40] Therefore, SERS enhancements in the oil-configuration may be influenced by more plasmonic modes than the typically-considered dipole.

Finally, despite the high reproducibility of the NPoM nanojunction self-assembly, at the small gap size of ~ 1 nm, even a small change in the constituent elements can yield a significant shift of the plasmon as seen from the spread of individual DF resonances. For example, the measured (11) mode of 80 nm NPoMs varies across a 70 nm range, showing that a statistically-significant number of single NPoM measurements will be key to uncover the underlying physics.

5.3.3 NPoM hotspots and number of MB molecules

Before moving on to experimental results, it is useful to gain an approximate idea about the plasmonic enhancements and number of MB molecules participating in the SERS signal for each NPoM. Therefore, we ran FDTD simulations at the experimental conditions of 70 ° p-polarised illumination at 633 and 785 nm. Placing a 2D electric field monitor into the NPoM gap (Figure 5.5), we extracted electric field and plasmonic enhancement profiles and an example for a 60 nm NPoM under 785 nm illumination is plotted in Figure 5.14.

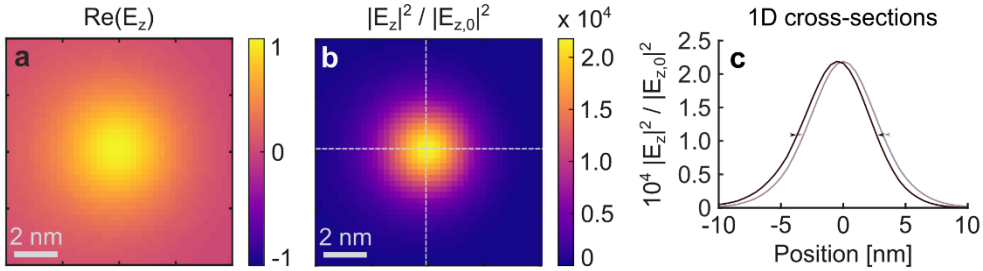

Figure 5.14 ***Simulated electric field maps inside the gap of a 60 nm NPoM in oil immersion under 70 ° p-polarised illumination at 785 nm.*** *a) Normalised real part of the electric field perpendicular to the NPoM gap showing a (10) dipole bonding mode. b) Plasmonic enhancement map in the NPoM gap normalised to a simulation without the nanoparticle. c) Cross-section of the plasmonic enhancement along the dashed lines in b). The maximum enhancement is 2x10^4 and the arrows denote the FWHM used to estimate the mode cross-section area.*

For a 60 nm NPoM, 785 nm wavelength approaches the bonding dipole resonance (Figure 5.13d) which is consistent with the electric field distribution in Figure 5.14a.

The normalised intensity map in Figure 5.14b shows enhancements up to 2.2 x10^4, similar to NPoM systems with different spacers with comparable gap sizes.[176]

The maximum enhancements for each NPoM size and illumination wavelength used in the experiments are summarised in Table 5.1 and show approximately 2-fold stronger enhancement at 633 nm with respect to the 785 nm illumination.

*Table 5.**1 Simulated maximum SERS enhancements, $|E_z|^2/|E_{z,0}|^2$, for four NPoM diameters and two illumination wavelengths.***

	40 nm	**50 nm**	**60 nm**	**80 nm**
633 nm	21 000	32 100	42 900	38 300
785 nm	11 500	21 000	21 900	24 500

Plotting the cross-section of the local intensity enhancement (Figure 5.14c), we can estimate the maximum number of MB molecules giving rise to the SERS signal for each NPoM. Defining the FWHM enhancement as the diameter of the plasmonic hotspot, we calculate the corresponding hotspot area. We then divide it by the area of one CB7 molecule (diameter 1.6 nm)[163] yielding the number of MB molecules at full CB7 occupancy. Alternatively, one can multiply the hotspot area by the reported surface coverage of CB7 on a gold surface (2.41 x10^{13} molecules cm^{-2})[190] and both methods yield the same result summarised in Table 5.2. Note that the molecules in this hotspot produce ~ 90 % of the total SERS signal as the SERS enhancement scales with the square of the plasmonic enhancement.

For all measurement conditions, the number of MB molecules in each hotspot lies in the few-molecule limit. At 633 nm, the number of MB molecules is approximately half of that under 785 nm, consistent with the reverse trend for the maximum enhancement factors as the incoming electric field is concentrated into a smaller hotspot at 633 nm.

*Table 5.2 **Estimated maximum number of MB molecules in the NPoM hotspot, for four NP diameters and two illumination wavelengths.***

	40 nm	**50 nm**	**60 nm**	**80 nm**
633 nm	8	8	8	10
785 nm	12	14	16	19

Having a basic understanding of the plasmonic and molecular properties of the MB-NPoM system, we can move on to experimentally characterising the SERS response of the system in the oil-immersion configuration.

5.3.4 SERS in the continuous-wave regime

We measured SERS spectra of MB-functionalised NPoMs for NP diameters of 40, 50, 60 and 80 nm with a 633 nm HeNe laser resonant with MB absorption and a 785 nm CW laser (Figure 5.15). For each set of conditions, 1000+ single-NPoM spectra were recorded, sorted by the SERS to background ratio and the middle 50 % spectra averaged to avoid skewing the results by outliers. The entire measurement set was also repeated on a separate set of samples to ensure reproducibility.

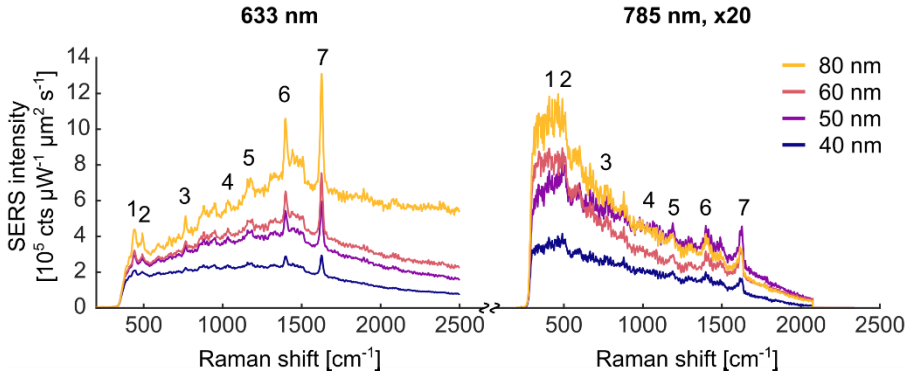

Figure 5.15 ***Mean SERS spectra of MB inside 40-80 nm NPoM junctions under 633 nm and 785 nm CW illumination.*** *The spectra are normalised to the illumination intensity, corrected for wavelength-dependent efficiency and the 785 nm spectra are multiplied by 20 to match the intensity scale of the 633 nm data. Each measurement comprises 1000+ single NPoMs where the spectra are sorted based on their SERS to background ratio, the bottom and top 25% of spectra are rejected and the remaining spectra averaged. This produces representative spectra for each NPoM size without outliers such as dirt particles and picocavity events. The 7 highlighted Raman bands are considered in further analysis of background-subtracted SERS counts.*

The spectra were normalised for illumination and detection efficiency allowing a quantitative comparison between the two wavelengths. The 7 brightest peaks are highlighted and the sum of their background-subtracted counts used as a measure of overall MB SERS. The total signal at 633 nm is ~ 20 times stronger than at 785 nm. This difference increases to ~ 100 times when comparing MB SERS only as the Stokes scattering at 785 nm is dominated by a broad background. The difference in SERS intensity at 633 nm and 785 nm illuminations cannot be purely explained by the 2-fold difference in enhancement factors or number of MB molecules in the NPoM hotspot suggesting that the dominant factor is actually the resonance of the laser with the electronic transition of MB (resonant Raman).

In addition to the SERS counts, the shape of the broad background changes: for 633 nm, the background moves to a higher Stokes shift with increasing NP diameter whereas for 785 nm, it shifts the other way – towards the Rayleigh line.

For a deeper insight into the interplay of the NP size and SERS, we plotted the full distribution of background-subtracted SERS intensity of the 7 peaks highlighted in Figure 5.15, along with the relevant MB and NPoM resonances (Figure 5.16).

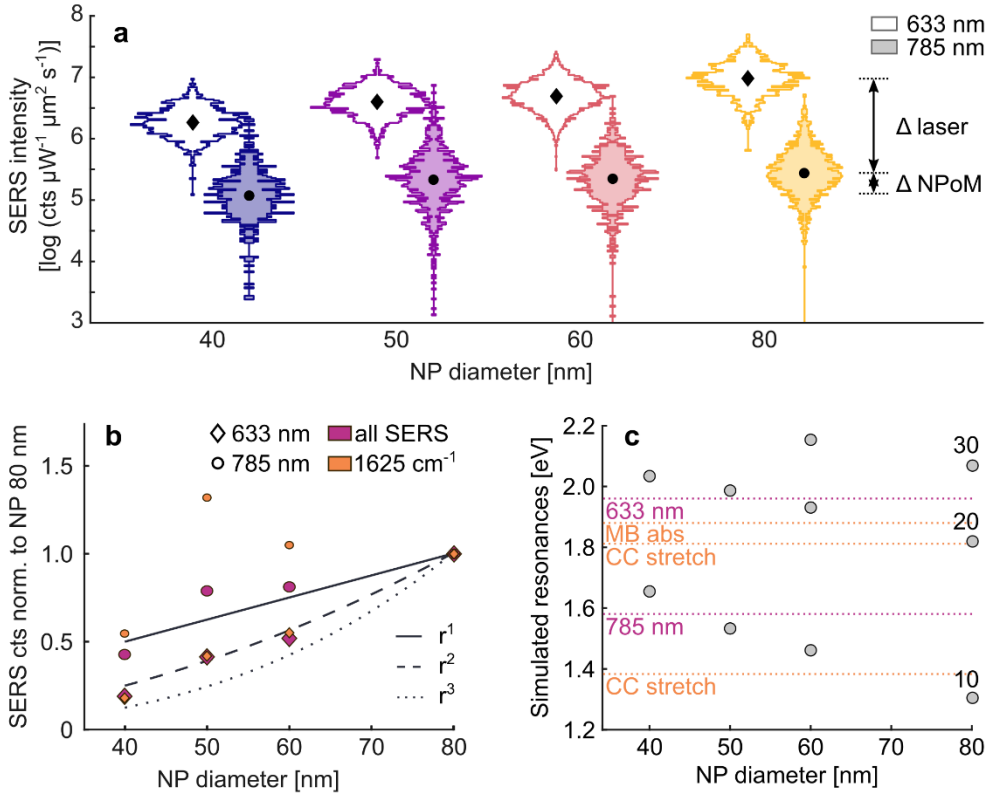

Figure 5.16 ***SERS intensity dependence on NP size and laser wavelength.*** *a) SERS counts distributions of 1000+ single NPoMs for different nanoparticle sizes under 633 and 785 nm illumination. b) Medians of the Stokes (purple) and 1625 cm^{-1} band (orange) distributions in a) normalised to 80 nm NPoM. Different scalings with the NP radius (r) are overlaid as black lines. c) Simulated NPoM resonances under p-polarisation along with relevant laser and MB resonances marked by horizontal lines.*

As already seen from the mean spectra, the SERS counts at 633 nm are 1-2 orders of magnitude higher than at 785 nm. The distributions are also narrower at 633 nm showing lower relative variability in SERS intensity. This is interesting as in a non-resonant SERS, higher signal often comes from extreme randomly formed hotspots resulting in very wide SERS distributions. The median SERS was also overlaid with several lines with expected scaling with the NP radius, r, based on previous results in literature (Figure 5.16b).[176] At 633 nm (diamonds), SERS follows an r^2-r^3 trend. Similar scaling has been observed for non-resonant SERS upon scanning the quadrupolar resonance of the NPoM cavity across the illumination laser[176] which is the case at 633 nm here (Figure 5.16c). The lack of significant SERS

increase for 50 and 60 nm NPoMs whose 20 quadrupole modes, that do seem to couple to the far-field, overlap with the laser show that the electronic resonance of MB with the illumination dominates over the plasmonic resonance of the NPoM cavity itself.

The off-resonant laser at 785 nm yields a more complicated SERS intensity dependence. This is more clearly seen by examining the brightest vibration at 1625 cm^{-1} (Figure 5.16b, orange circles). Taking the r^2 trend line as a reference and see that the strongest additional SERS enhancement of ~ 3-fold is achieved for the 50 nm NPoM, followed by ~ 2-fold additional SERS for 60 nm and 40 nm NPoMs. This trend follows the overlap of the NPoM 10 dipole resonance with the laser.

A more detailed insight into the mechanism of SERS signal scaling with NP size is beyond the scope of this work. However, we did establish two important observations: the resonance Raman enhancement reaches up to 2 orders of magnitude in addition to the SERS at 785 nm illumination and is superior to the few-fold signal gain achieved by tuning the NPoM dipolar resonance to the illumination. This knowledge is crucial for experimental design of multi-wavelengths experiemnts such as pump probe Raman spectroscopy.

5.3.5 Pulsed laser-induced phototoxicity

Pump-Probe Raman or excited state Raman works by promoting a system into a non-equilibrium state and interrogating the transient evolution by a spontaneous Raman scattering. The time resolution is dictated by the duration of the pump and probe pulses and the lifetime of the vibration itself. Typically however, the main limiting factor is the pulse duration of the probe, because it tends to be spectrally filtered to ~ 10 cm^{-1}, otherwise yielding too broad Raman bands that may get buried within the noise of the detector. Through the time bandwidth product, the probe pulse then stretches to a few picoseconds.

A picosecond pulse of a typical Ti:Sapphire oscillator with an 80 MHz repetition rate has 10^4 higher peak power than an equivalent CW laser as given by the ratio of the laser pulse period and the pulse length. Combining this temporal concentration of illumination with the spatial plasmonic enhancement of another 10^4, it is easy to reach phototoxic conditions and damage the system under study. The Raman scatterer can undergo chemical reaction and the NPoM itself can also be damaged if the NP is restructured via heating (NP melts) or if the cavity gap is fused by gold atom movement. The NPoM gap, given by the thickness of the CB7 molecular spacer, is only ~ 3 gold atoms thick and therefore, a one-atom protrusion could already be enough to induce a tunnelling current and short-circuit the nanojunction.

In this section, we will experimentally establish the viable measurement conditions for ultrafast Raman on the NPoM platform and give insight into the underlying processes that limit the experimentally-explorable regimes, ultimately paving way for better design of plasmonic structures for time-resolved spectroscopy.

It has been shown that pulsed and CW illuminations yield the same number of SERS photon at low powers. With increasing power, the pulsed laser yields more photons until the SERS disappears due to a some permanent change in the system.[191] As a first estimate of the viable illumination fluences, we compared the SERS emission from the 60 nm NPoM under a CW and pulsed illumination at 633 nm. We added an OPO to the setup to tune the output of the Ti:Sapphire laser from 785 nm to 633 nm (Figure 5.8). We then spectrally filtered the light using a grating stretcher down to ~ 10 cm^{-1} bandwidth which also stretched the pulses in time to 4 ps. We recorded SERS spectra of MB inside 60 nm NPoMs under this pulsed illumination (50 NPoMs) and using a HeNe (other 50 NPoMs on the same sample). The median spectra and corresponding overall signal (including background) and SERS counts (background-subtracted signal at 1625 cm^{-1}) under each illumination are plotted in Figure 5.17. Both measurements were normalised for incident laser intensity (average power measured at focus divided by the laser spot area) and the wavelength dependence of the detection efficiency. The latter normalisation was the same for the CW and pulsed laser as both were tuned to 633 nm.

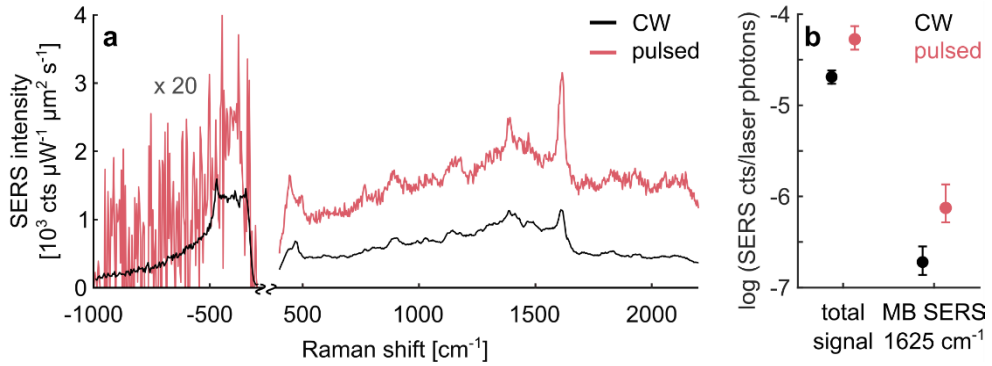

Figure 5.17 ***SERS under CW and pulsed illumination at 633 nm for 60 nm NPoMs.*** *a) Median SERS spectrum where the anti-Stokes part is multiplied by 20 for clarity. b) Detected SERS photons per laser photons ("SERS quantum efficiency") corrected for illumination, instrument transmission and quantum efficiency. The dot represents the median and the vertical bars the lower and upper quartiles. The average laser irradiance was 260 and 5.7 μW μm^{-2} for the CW and pulsed laser, respectively.*

The median pulsed SERS spectrum in Figure 5.17a is significantly noisier than the CW spectrum. This is expected as the CW SERS signal is emitted continuously whereas the 4 ps laser pulse is 3300-times shorter than the Ti:Sapphire laser pulse period and thus for ~ 99.97% of the time, the camera integrates noise only.

Simulating the extinction cross-section of the 60 nm NPoM at 633 nm (details later in Figure 5.23), allows us to estimate the "SERS quantum efficiency", $QE_{SERS} = r_{SERS}/r_{NPoM}$, as the ratio of the SERS rate, $[r_{SERS}] = cts/s$, and the rate of photons incident on a single NPoM, $[r_{NPoM}] = cts/s$. The former quantity is simply the detection efficiency-normalised SERS intensity used in the plots throughout this work. The rate of photons that interact with a single 60 nm NPoM can be estimated using the average laser intensity, I_{las}, the 60 nm NPoM extinction cross-section, σ_{ext} , and the photon energy, E_{ph} , as: $r_{NPoM} = 2\, I_{las}\, \sigma_{ext}/E_{ph}$. Note that the factor of two takes into account the NPoM being placed in the centre of the approximately Gaussian illumination spot where the power is twice as high as the average power.

The quantum efficiency distributions for the measurements from Figure 5.17a are plotted in Figure 5.17b for the total detected signal including the broad background and the background-subtracted 1625 cm^{-1} Raman band. Interestingly, the pulsed SERS is ~ 2.5 (4) times more efficient than the CW signal for all non-Rayleigh scattered light (1625 cm^{-1} MB band) suggesting the illumination power is close to the damage threshold. This has been confirmed experimentally by increasing the power of the pulsed illumination 10 times, which caused the MB SERS signal to disappear completely (not shown).

Hence the first estimate of viable experimental conditions at 633 nm are laser intensity up to ~ 10 μW μm^{-2} for 4 ps pulse length where the system emits one non-Rayleigh photon (SERS + broad background) for every 10^4 laser photons. Also, the CW spectra were recorded at 46 times higher average laser intensity without any deterioration of the SERS signal suggesting that the phototoxicity has a multi-photon origin.

An in-depth study recording the pulsed SERS at various powers is complicated by the narrow range of powers that gives stable and detectable[146] signal at a reasonable integration time. This issue can be circumvented by monitoring an indirect effect of the pulsed laser on a CW SERS serving as a probe of the integrity of both the MB molecule and the NPoM cavity itself. Leveraging on the insight into SERS dependence on illumination and NPoM size, we use a 633 nm CW SERS as a stable, non-phototoxic probe. As the pulsed perturbation, we employ a 785 nm Ti:Sapphire laser with a ~ 150 cm^{-1} bandwidth and study the phototoxicity as a function of pulse length and average power. The wavelength offset of the two lasers guarantees that changes in the CW SERS spectrum do not come from a direct Raman or fluorescence due to the 785 nm laser, but result from some modification of the molecule, NPoM cavity or the surrounding environment.

Experimentally, the two lasers are overlapped at the sample and a CW SERS trace is recorded (Figure 5.18a). For a middle third of the trace, the pulsed laser is added such that the first third serves as a CW reference, the middle shows modifications due to the pulsed illumination and the final segment shows any persisting changes after the pulsed laser is off. In the example spectral trace (Figure 5.18b), the SERS intensity drops upon pulsed illumination and does not recover after the 785 nm laser is blocked showing a permanent loss of SERS. This is also seen in the time trace of background-subtracted SERS counts of the 1625 cm^{-1} band (Figure 5.18c), which we will use as an estimate of MB SERS.

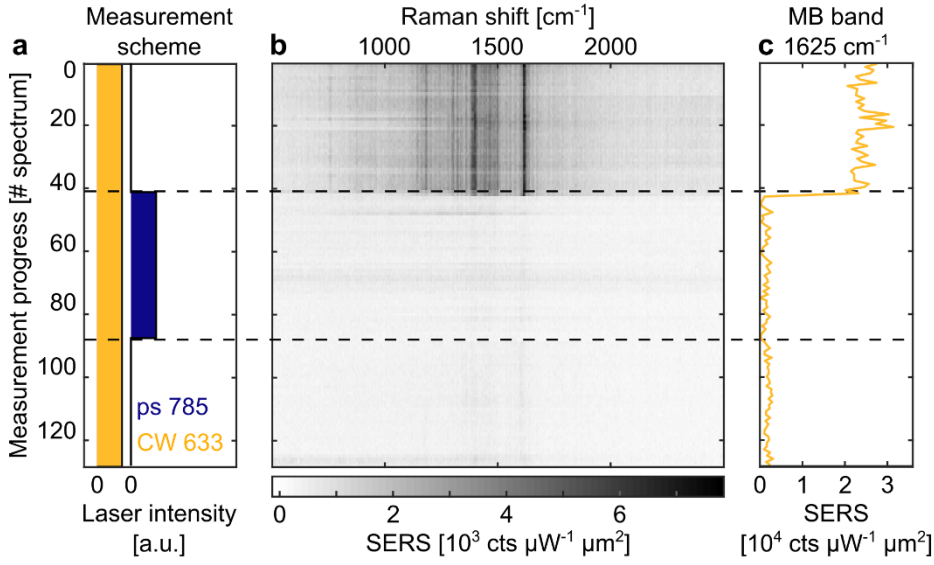

Figure 5.18 ***Measurement scheme of pulsed laser impact on NPoM SERS*** *a) Laser illumination during each single NPoM measurement. b) SERS time trace of a 60 nm NPoM showing an irreversible loss of SERS upon pulsed laser illumination. c) Integrated, background-subtracted SERS intensity of the strongest MB Raman band at 1625 cm^{-1}. Each spectrum was integrated for 50 ms.*

To compare many single-NPoM measurements, it is useful to reduce the information within the SERS trace into a few numbers. Firstly, we can plot the median spectra of the three segments of the measurement trace (Figure 5.19a). Upon exposure to the pulsed laser, the original healthy SERS drops by > 90 % in intensity and the broad background becomes more dominant, but the SERS spectrum remains otherwise unchanged (Figure 5.19a, inset). Taking the brightest SERS band as a measure of MB SERS, we can integrate the background-subtracted intensity of the 1625 cm^{-1} peak for each spectrum, repeat the measurement on 1000+ NPoMs and plot the distributions of MB SERS for each segment of the spectral time trace (Figure 5.19b). Note that due to an approximately exponential distribution of SERS enhancements, it is meaningful to plot the logarithm of the SERS

intensities. The distributions under CW + ps and CW after ps illumination overlap showing that the pulsed laser damage is permanent. Hence it is sufficient to evaluate the relative change in SERS counts between the two CW illuminations (Figure 5.19c). The majority of the NPoMs show a 90 % decrease in MB SERS, from ~ 10^5 to ~ 10^4 cts/ µW µm^{-2} s. Approximately 15 % of particles show SERS loss below the detection sensitivity limit (~ 5 cts µW^{-1} µm^2 s^{-1}) and are marked by an asterisk.

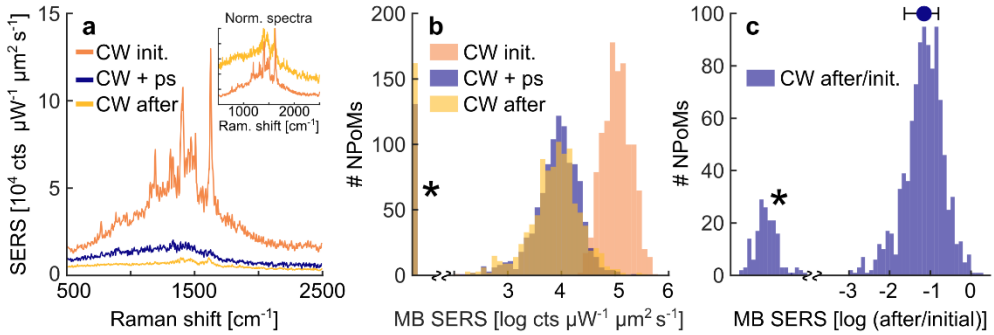

Figure 5.19 ***Quantitative insight into pulsed laser impact on NPoM SERS*** *a) Median CW SERS spectra under CW, CW+pulsed and a following CW illumination. The pulsed laser intensity was 25 µW µm^{-2} and the pulse duration 3.5 ps. The inset shows spectra normalised to the 1625 cm^{-1} band. b) Distributions of background-subtracted MB SERS intensities of the 1625 cm^{-1} band under the same illumination as in a). c) Distribution of the change in CW MB SERS before and after pulsed illumination with the median and lower and upper quartiles marked on the top. The asterisk marks a fraction of NPoMs that did not show detectable MB SERS after pulsed illumination.*

The distribution in Figure 5.19c can be characterised by its median and lower and upper quartiles as shown on top of the histogram plot. Using this measure to characterise the pulsed laser influence on the MB SERS, we repeated the measurement for a wide range of average powers and pulse durations. The former parameter was adjusted using a neutral density filter. The pulse duration was controlled by removing the spectral filtering slit from the grating stretcher and varying the distance between the grating and the collimation lens (Figure 5.8). The resulting chirp yielded laser pulses between hundreds of femtoseconds and a few picoseconds. Additionally, we placed a “fibre stretcher” into the pulsed laser path where the light propagated through different lengths of a single-mode fibre gaining an extra chirp. Combining the two “stretchers”, we produced pulses from 265 fs to 18 ps at the focus of the microscope as measured by an autocorrelator.

For each set of conditions, we recorded 100-1000 single-NPoM SERS traces, calculated the relative SERS change upon pulsed illumination and plotted the median and lower and upper quartiles of each dataset for easy comparison between the measurement conditions (Figure 5.20). The colour of the points represents a

series of measurements done on (different areas of) the same sample by either varying the average power while keeping the pulse length constant (Figure 5.20a) or vice versa (Figure 5.20b).

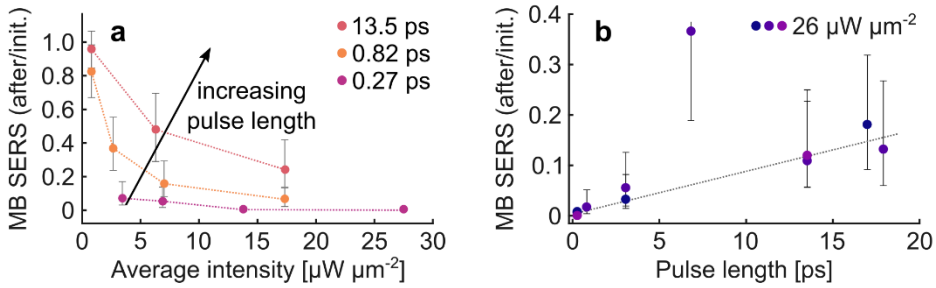

Figure 5.20 ***Relative change in MB SERS before and after pulsed illumination for 60 nm NPoM.*** *a) Three series of measurements with constant pulse lengths and b) three series of measurements under constant average laser intensity.*

As expected, increasing average laser intensity results in higher loss of MB SERS signal. Interestingly, stretching the laser pulse in time counteracts the phototoxicity as evidenced by SERS change distributions at similar laser intensities in Figure 5.20a and the linear trend of SERS change when the pulse length is varied systematically for each sample Figure 5.20b. The repetition rate of the laser is constant and thus dependence on pulse length at the same average intensity reports on the peak intensity of the laser pulses calculated as the average intensity scaled by the ratio of the laser pulse period to pulse length.

Overlaying all measurements on the same plot against the peak intensity of the pulsed laser reveals further insight into the nature of the photoinduced SERS loss (Figure 5.21). The peak intensities achieved by power and pulse length variation span five orders of magnitude uncovering two phototoxicity regimes. Note that the blue and violet points at the lowest peak intensities were measured with the Ti:Sapphire laser in a CW operation to give an “infinite pulse length” reference.

Below a threshold peak intensity of ~ 10^4 μW $μm^{-2}$, the loss of SERS is moderate, up to ~ 50 %, and does not depend on the peak power suggesting a single-photon mechanism. The interquartile range of each single-NPoM distribution (Figure 5.21, inset) is ~ 40 %, reporting on the heterogeneity among the individual NPoMs within the same sample. Variation among different samples can be estimated to ~ 30 % as shown by a repeated measurement on two different samples (two pink points at the lowest average intensity). Therefore, the observed phototoxicity yielding SERS loss up to 50 % is comparable to the phototoxicity variations due to the inherent heterogeneity of the NPoM system stemming from the extreme SERS enhancement

in the gap. As such, we conclude that this moderate SERS loss with a single-photon mechanism is present for virtually all laser intensities.

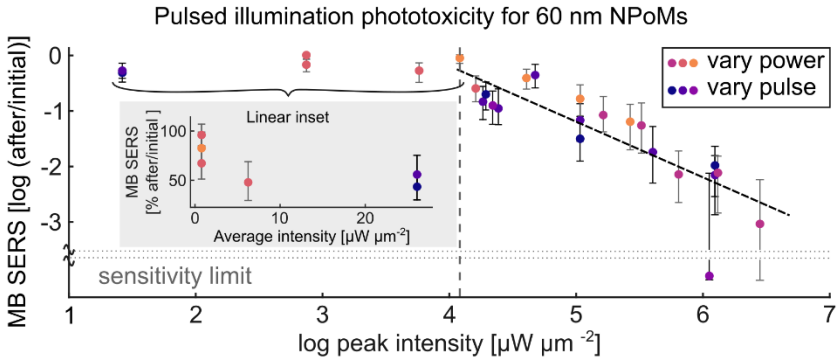

Figure 5.21 ***60 nm NPoM distributions of the relative change in MB SERS before and after pulsed illumination****. Main plot) Quantitative MB SERS evolution before and after pulsed illumination. Each dot represents a set of 100-1000 single NPoM SERS traces where the colour denotes measurements on (a different area of) the same sample. Points represent medians and vertical bars the lower and upper quartiles of the underlying distributions. The vertical axis is discontinued at the sensitivity limit of the setup. Points above ~ 10⁴ μW μm⁻² peak power are overlaid with a black dashed line with a slope of -1. Inset) SERS loss of the points at peak powers below ~ 10⁴ μW μm⁻² plotted on a linear scale against the average laser intensity.*

Above the ~ 10^4 μW μm^{-2} threshold, the relative SERS change upon pulsed illumination follows a log-log trend with a slope of -1 with peak intensity down to over 1000-fold SERS loss at which point the remaining signal reaches the detection limit of the setup. In other words, $SERS_{CW,after} = SERS_{CW,initial} / I_{pulsed,peak}$.

Varying average power or pulse length are interchangeable, further confirming that the key parameter to the laser-induced SERS loss is the peak intensity. This finding is crucial as it suggests that heating, proportional to number of absorbed photons and hence pulse energy, is likely not responsible for the loss of SERS.

The combination of a peak intensity threshold points to a multi-photon photochemistry of the SERS loss. Furthermore, since the peak power dependence holds true across the 265 fs – 18 ps pulse length range probed here, the photodamage must occur faster than the shortest pulse of 265 fs. In a contrary case, the longer pulses would be less phototoxic with a change of peak power scaling around the lifetime of the process, or the SERS loss would depend on pulse energy, which we ruled out already (see section 5.4.2 for more details).

The experimental observations for the 60 nm NPoMs can be summarised as follows. In a single-photon regime below ~ 10^4 μW μm^{-2} peak intensity, pulsed illumination induces SERS loss down to 50 % across all laser intensities. The median SERS loss is

relatively mild as it is comparable to the interquartile range of the underlying single NPoM distribution of ~ 40 %. At higher peak laser intensities, the relative loss of SERS scales with peak intensity across pulse lengths of 265 fs to 18 ps suggesting a multi-photon damage mechanism that occurs on a faster timescale than the shorter pulse length of 265 fs.

To shed more light on the multiphoton SERS loss regime, we repeated the measurements for NPoM sizes of 40-80 nm at both p- and s-polarised pulsed illumination for the 60 nm NPoM threshold peak intensity of 10^4 µW µm^{-2} and a 100-fold higher peak intensity of 10^6 µW µm^{-2} (Figure 5.22).

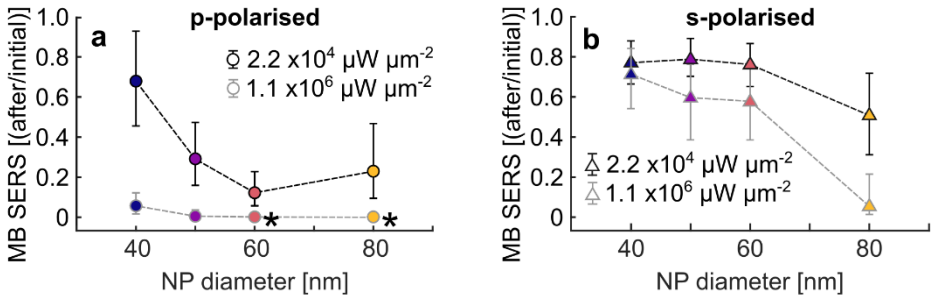

Figure 5.22 ***Impact of pulsed illumination on MB SERS for different NPoM sizes*** *for a) p-polarised pulsed illumination parallel to the long axis of the NPoM and b) s-polarised pulsed illumination perpendicular to the long axis of the NPoM. Each point is a median of a distribution of 1000+ single-NPoM measurements and the vertical bars show the lower and upper quartiles. Distributions with over 50 % NPoMs with SERS after pulsed illumination below the detection sensitivity limit are marked by an asterisk. The dashed lines are a guide for the eye.*

For each set of conditions, we measured over 1000 NPoMs and plotted the median and lower and upper quartiles of the distribution of relative SERS change upon pulsed illumination. For p-polarised pulsed laser illumination along the long NPoM axis, the high peak intensity yields a SERS loss below the setup sensitivity for 60 and 80 nm NPoMs. The lower peak power dataset shows the highest damage for 60 nm NPoM followed by 50 and 80 nm with similar phototoxicity, and finally the 40 nm NPoM with a significantly lower SERS decrease upon pulsed illumination. Recall that varying the NPoM size from 40 to 80 nm scans the dipole (10) mode across the laser wavelength of 785 nm (Figure 5.16c). The maximum of the phototoxicity for 60 nm NPoM then suggests that the underlying mechanism is assisted by the plasmon resonance, as opposed to for example a pure size effect.

The s-polarised geometry (Figure 5.22b) exhibits a significantly lower phototoxicity than the p-polarised illumination across all NPoM sizes. Even at 10^6 µW µm^{-2} peak intensity, the 40-60 nm NPoMs remain within the ballpark of < 50 % SERS loss, which dominates at low powers (Figure 5.21). This can be rationalised by the inability of

s-polarised light to excite the longitudinal modes of the NPoM that produce strong electric field inside the gap between the nanoparticle and the mirror. In fact, all modes excited by an s-polarised source have a node of zero intensity at the centre of the NPoM gap, which is the region of strongest SERS enhancement probed by the CW laser that is p-polarised in all experiments.

Considering that the NPoM modes excited by the s-polarisation are all significantly blueshifted from the laser at 785 nm (Figure 5.13d), the damage increase with increasing NPoM size follows the expected trend of stronger optical response of larger particles stemming from the Mie theory (chapter 2). The only severe SERS loss under s-polarisation was achieved at peak intensity of 1.1 x 10^6 μW $μm^{-2}$ for the 80 nm NPoM and this is likely due to imperfect polarisation preservation by the high-NA illumination objective.[16]

The resonance dependence of the multi-photon phototoxicity in Figure 5.22a can be explored in more detail by calculating NPoM cross-sections and maximum SERS enhancements using FDTD simulations. Recall, that the extinction cross-section is a sum of absorption and scattering cross-sections and scales with the ability of the NPoM to interact with light (chapter 2). Interestingly, the experimentally-observed SERS loss trends (Figure 5.22) match closely onto the calculated near-field properties (Figure 5.23). Under p-polarisation, the 40 nm NPoM shows the lowest damage accompanied by a steep decrease in extinction cross-section and SERS enhancement with respect to other NPoM sizes. For s-polarisation, both highest phototoxicity and near-field plasmonic response are achieved for the 80 nm NPoM. Although both experimental and simulated differences among 50-80 nm NPoMs are rather subtle, we note that the phototoxicity under p-polarisation maps best onto the scattering cross-section and it would be interesting to expand the NPoM size library to verify this trend.

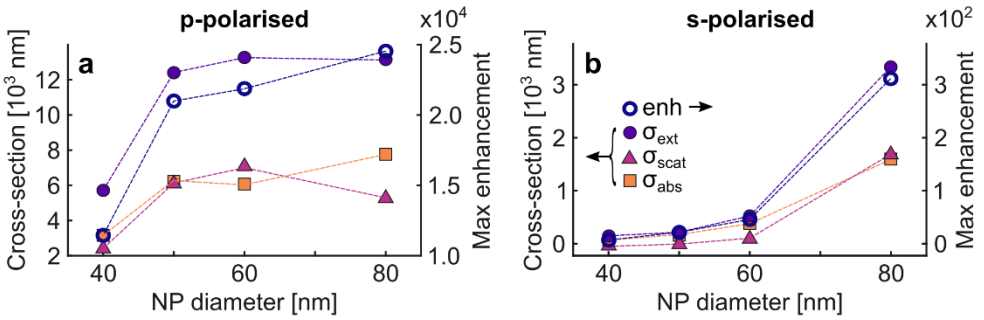

Figure 5.23 ***Simulated cross-sections and electric field enhancements under 785 nm illumination for NPoMs immersed in oil.*** *The enhancements are calculated as electric field intensity in the NPoM gap normalised to the value without a nanoparticle, $|E_z|^2/|E_{z,0}|^2$. The illumination angle is 70 ° matching the experiment and the incident light is a) p-polarised and b) s-polarised. The dashed lines are a guide for the eye.*

In summary, we have identified two phototoxicity regimes due to pulsed illumination. A single-photon mechanism yielding < 50 % SERS loss dominant at low peak intensities and a multi-photon mechanism with a peak intensity threshold at ~ 10^4 μW μm^{-2} for a 60 nm NPoM at 785 nm. The multi-photon process occurs on a faster timescale than the shortest laser pulse of 265 fs based on its constant dependence on peak power across 265 fs-18 ps pulse lengths. Measurements on four NPoM sizes at two different polarisations showed that coupling to the longitudinal mode of the NPoM is key for the multi-photon induced SERS loss. This conclusion is further supported by FDTD simulations showing a good match between the calculated near-field properties and measured SERS loss for the four nanoparticle sizes and two laser polarisations. Below, we interpret these findings within the context of plasmon-assisted photochemistry mechanisms most commonly proposed in literature. We show that the single-photon phototoxic regime corresponds to gold surface restructuralisation and narrow down the possible mechanisms of the multi-photon phototoxicity to hot electrons, multi-photon ionisation, or from a plasmon-mediated vibrational pumping of the MB inside the NPoM cavity.

5.4 Discussion

5.4.1 SERS evolution in the single-photon regime

In the regime under mild illumination, SERS loss is independent of the peak laser intensity pointing to a single-photon mechanism. The phototoxicity does however loosely follow the average laser intensity (Figure 5.21). In other words, higher number of incident photons yields higher SERS loss suggesting a series of independent single-photon underlying processes. We can verify this by examining the time trace of the background-subtracted MB CW SERS of single 60 nm NPoMs (Figure 5.24) retrieved from the measurements summarised in Figure 5.21. The three selected peak laser intensities of 25, 10^4 and 10^6 μW μm^{-2} correspond to the mildest (Ti:Sapphire operating in a CW mode), threshold and multi-photon phototoxic regimes, respectively.

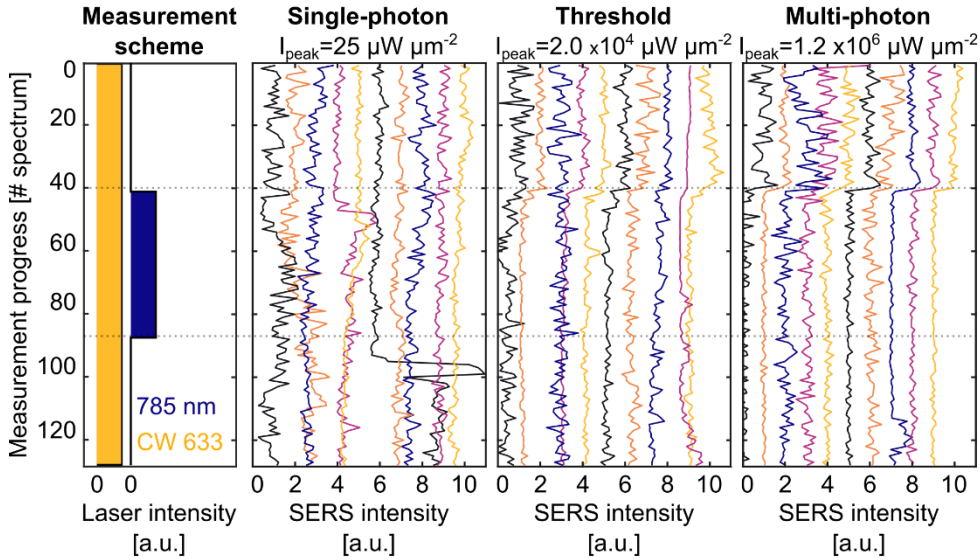

Figure 5.24 ***MB SERS from 60 nm NPoMs under 633 nm CW illumination modulated by a pulsed laser at 785 nm****. left) Illumination scheme within each measurement trace. The 633 nm CW laser is on during the whole measurement giving rise to the observed SERS spectrum. The horizontal dotted lines delimit the 785 nm illumination duration. right) Example NPoM SERS traces normalised to the average of the first 40 spectra. Each set is illuminated by the same average power of the 785 nm laser of 25 μW μm^{-2} and the corresponding pulse lengths and peak powers are marked at the top of each set.*

In Figure 5.24, we see that the SERS change within the single-photon SERS loss regime proceeds gradually over many small intensity jumps. Interestingly, these jumps occur either above or below the original SERS rate with an overall trend towards lower SERS intensity. This step-wise SERS change is in stark contrast with the single-step sharp SERS loss at the onset of the pulsed 785 nm illumination that

is visible at the threshold peak intensity and even clearer in the traces measured well inside the multi-photon regime.

The positive and negative jumps in intensity with an overall downward trend in the linear phototoxicity regime are consistent with a reconstruction of the gold facets in the NPoM gap. Each 785 nm photon carries sufficient energy to overcome the activation barrier of surface atom diffusion of gold ~ 0.9 eV.[140] The atoms at defect sites have the lowest binding energy and will migrate easiest, step-by-step hopping across the gold surface converging to lower energy positions until the system reaches a steady state geometry. Since the highest SERS enhancements occur for the most irregular hotspots, the overall trend will be a decrease in SERS, except for occasional transient bursts as the atoms temporarily hop into a high energy site as they migrate through the gap. The slow step-wise decrease of SERS intensity has also been observed in related systems of nanoparticle dimers down to 80 and 40 % of the original SERS level, consistent with our findings.[149,192,193]

Although this gold atom migration induces SERS fluctuations that may be experimentally undesired, it can be actually exploited to push the reproducibility of the nanogaps beyond the ballpark achieved by the self-assembly itself. A prolonged gentle illumination of an NPoM should yield the lowest energy gap geometry, which could be useful in applications where reproducibility is more important than a 50 % decrease in the SERS signal, which is vanishingly small compared to the overall SERS enhancement of many orders of magnitude. In fact, a similar prolonged illumination strategy has been employed in gold dimer antennas to improve the linear SERS reference in a pump-probe SERS experiment.[149] One must consider the acceptable SERS enhancement loss carefully, however, because at some point dielectric antennas may provide comparable performance to the “laser-stabilised” gold equivalent.[194]

5.4.2 SERS evolution in the multi-photon regime

The limiting factor for ultrafast SERS measurements is laser-induced SERS loss that stars to dominate above a certain peak intensity threshold (10^4 μW μm^{-2} for 60 nm NPoMs at 785 nm) suggesting a multi-photon underlying mechanism. In the results section, we briefly outlined how the SERS loss dependence on peak laser intensity pointed to a timescale of the damage process well-below the shortest pulse length of 265 fs. Here, we describe this reasoning in greater detail within the context of two limiting cases: when incident laser pulses are much shorter than the characteristic timescale of the process ($\tau_{pulse} << \tau_{process}$) and vice versa ($\tau_{pulse} >> \tau_{process}$). In the former scenario (Figure 5.25a), all photons within the laser

pulse (proportional to the area under the pulse power profile) contribute to the same iteration of the multi-photon process because they are supplied essentially instantaneously with respect to the process duration. As the number of photons is proportional to the pulse energy, $E_{pulse} = E_{photon}\, n_{photon}$, the multi-photon process will depend on the pulse energy. In the opposite extreme (Figure 5.25c) where the pulse length is considerably longer than the process, only part of its photons will be relevant for each iteration yielding an effective peak power dependence. For an intermediate case where the probed pulse lengths span both regimes (Figure 5.25b), a mixture of the two cases will occur. The threshold at which the multi-photon process will start to occur will then be given by the pulse energy (∝ number of photons) for shorter pulses and peak power (∝ number of photons in the relevant timescale) for the longer pulses. Therefore, the peak power dependence across pulse length of 265 fs to 18 ps probed here points to a process on a sub-265 fs timescale.

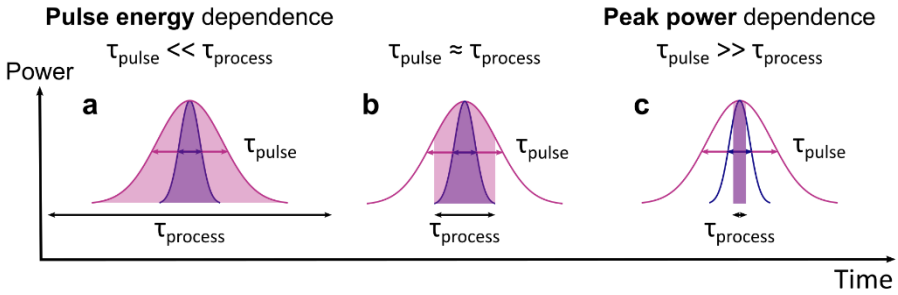

Figure 5.25 ***Conceptual representation of effective energy and power dependence regimes of multi-photon processes based on their timescale with respect to pulse length of the incident laser.***

Below, we discuss the SERS loss in terms of common plasmon-induced processes that match the experimental observations of a multi-photon mechanism on a sub-265 fs timescale (Figure 5.1). Firstly, we explore the role of hot electrons. Despite the incompatible timescale, we also verify the contribution of lattice heating because it has often been proposed as an alternative explanation to hot electron-induced chemistry.[195–200] Secondly, we explore the possibility of multi-photon absorption into the ionisation potential of MB. Lastly, we cover the feasibility of stepwise ultrafast vibrational excitations of MB ("vibrational pumping") followed by a chemical bond dissociation.

Lattice heating and hot electrons

When a metallic particle absorbs a photon, most of the photon's energy is converted into heat.[195] This heating process can be described by a two-temperature model where the electrons and the lattice of the metal are approximated as two coupled

systems each with its own effective temperature.[201] The photon absorption creates a non-equilibrium distribution of electrons with energies up to that of the incident photon. Within ~ 100 fs, the electrons self-thermalise via electron-electron scattering to a Fermi-Dirac distribution that can be assigned an effective temperature.[202] The effective electronic temperature can reach up to several thousands of Kelvin because the electron heat capacity is ~ 100 times smaller than that of the gold lattice at room temperature.[203] Therefore, they are often termed as "hot electrons". On a few-ps timescale,[204] the hot electrons transfer heat to the lattice phonons via electron-phonon scattering. The lattice equilibrates with the surrounding environment on a much longer timescale ~ 100 ps to several ns, depending on the properties of the environment.

Measuring the full time evolution of the temperature of the electron and lattice subsystems is extremely complicated due to the short time and length scales involved and sensitivity of the data analysis models to incorrect assumptions such as neglecting heating contributions of structures surrounding the simulated particle.[196,205,206] In our case, we are only interested in the temperature of the self-thermalised hot electrons and an estimate of the lattice temperature to definitively rule out lattice heating as the mechanism underlying the observed phototoxicity trend with peak intensity.

The electronic temperature prior to electron-phonon thermalisation can be extracted from the anti-Stokes Raman emission by fitting an exponential distribution to the broad emission background:[206,207]

$$I_{aS}(\omega) = A \exp\left(-\frac{\omega}{k_B\, T_e}\right) \qquad (5.1)$$

A is a proportionality constant, ω is the Raman shift, k_B the Boltzmann constant in cm^{-1}/K and T_e the effective temperature of the thermalised electrons. Although we did not measure the SERS spectra originating from the pulsed laser responsible for the non-linear SERS loss at 785 nm, we did manage to record a series of single-NPoM picosecond SERS spectra at 633 nm that can inform on typical plasmonic heating in the MB-NPoM system. As a control, we also recorded CW SERS spectra on the same sample at the same wavelength. Example spectra and the corresponding exponential fits to the anti-stokes background are shown in Figure 5.26a,b.

The validity of this approach is shown by the electronic temperature under CW illumination that remains close to the room temperature of 300 K. The pulsed laser yields hot electrons with effective temperatures of approximately 550 K. Note that

the picosecond SERS measurement was performed just below the ultrafast damage threshold at 633 nm to be able to retrieve the anti-Stokes signal. Yet, the effective temperature obtained here should be similar at the threshold intensity as the temperature increase diminishes with increasing laser powers because the heat capacity of electrons increases with temperature.[206]

The lattice temperature increase due to electron-phonon scattering can be estimated numerically. Remembering that the majority of absorbed light is converted into heat, the lattice temperature will be determined by the laser intensity and the absorption cross-section and the heat capacity of gold. Also, since the electron-phonon scattering occurs on a much faster timescale than lattice heat dissipation, we can assume that the absorbed light is instantaneously converted into lattice heat to yield the upper estimate of the lattice temperature.

For the CW illumination, the maximum lattice temperature will be given by the rate of light absorption and lattice heat dissipation that for a gold film occurs on a timescale of $T \approx 900$ ps.[208] The lattice temperature with evolve in time, t, according to:

$$T_l(t) = \frac{I_{CW}\,\sigma_{abs}\,t}{V_{NP}\,C_l}\,\exp\left(-\frac{t}{T}\right) \qquad (5.2)$$

where I_{CW} is the intensity of the laser, σ_{abs} and V_{NP} are the absorption cross-section and volume of the nanoparticle on a mirror, respectively and C_l = 2.45 10^6 Jm^{-3} K^{-1} is the lattice heat capacity of gold.[209] Using the average intensity value of 260 µW $µm^{-2}$ used to record the spectrum in Figure 5.26a, we obtain a maximum lattice temperature increase of ~ 2 K (Figure 5.26c).

For the picosecond laser, the pulse length is much shorter than the lattice heat dissipation and the laser pulse period is long enough for the system to equilibrate. Therefore, the lattice heating will simply be dictated by the energy of one laser pulse that is absorbed by the NPoM as:

$$\Delta T_l = \frac{I_{ps,avg}\,\sigma_{abs}}{f_{rep} V_{NP}\,C_l} \qquad (5.3)$$

where f_{rep} is the repetition rate of the laser. Inserting the experimental conditions of the measurement in Figure 5.26b into the equation yields a lattice temperature increase of 1.7 K. Figure 5.26d summarises the lattice temperatures calculated above as well as electronic temperatures obtained from exponential fits in to

anti-Stokes background of ~ 50 particles for CW and ~ 20 particles for ps illumination at 633 nm.

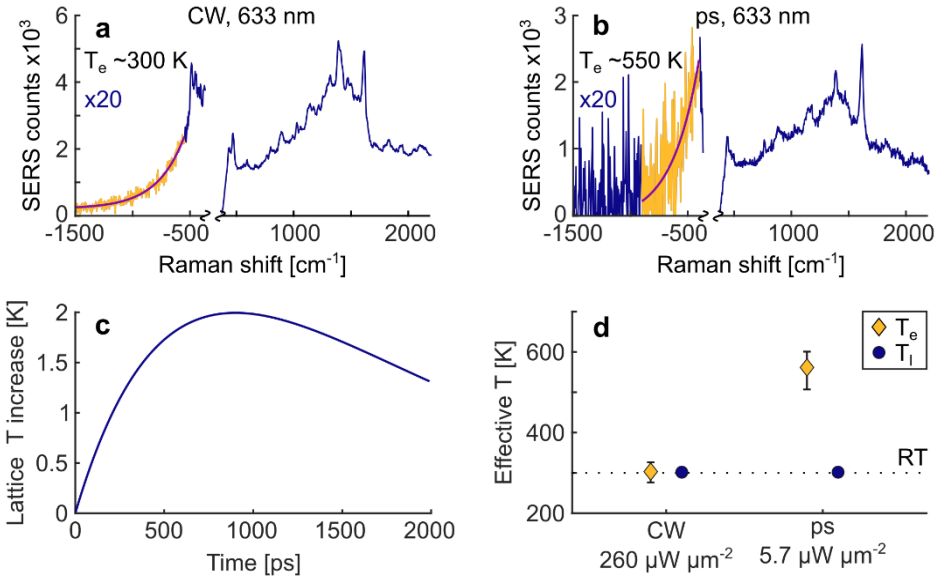

Figure 5.26 ***Temperature estimates of 60 nm NPoMs under CW and pulsed laser at 633 nm.*** *Example SERS spectra showing the anti-Stokes background fitted to an exponential to retrieve the electronic temperature of NPoMs under a) CW illumination at 260 µW µm^{-2} and b) illumination by ~ 4 ps pulses at 5.7 µW µm^{-2}. c) Estimated lattice temperature rise in time under CW illumination assuming an exponential lattice heat dissipation with a 900 ps lifetime. d) Summarised lattice and electron temperatures of 60 nm NPoMs under CW and pulsed illumination. The electronic temperature vertical bars represent the 25th and 75th percentile of ~ 50 (CW) and 20 (ps) measurements. The dotted line at 300 K marks the initial (room) temperature of the system.*

The lattice heating under our experimental conditions reaches up to 2 K and as such does not contribute to the SERS change in the non-linear regime. This is consistent with the observed constant decrease in SERS with peak power while the lattice heating would otherwise be proportional to the pulse energy, in other words the number of photons absorbed.

The exponential hot electron distribution follows a ~ 1/550 K decay under 633 nm illumination by 4 ps pulses just below the damage peak intensity threshold. This temperature seems unlikely to cause chemical change to MB as electronic temperatures of nanoparticles of several thousands of degrees have been reported in literature without photodamaging molecules in the plasmonic hotspot.[210] Yet, the precise threshold for a chemical change would depend on the alignment of the electron energy and the lowest unoccupied molecular orbital (LUMO) of the MB encapsulated by CB7 and the ability of the electrons of gold to tunnel into LUMO.

The orbital energies of MB would be affected by interaction with the NPoM and CB7 and could be calculated using density functional theory (although including sufficient atoms to capture the extramolecular influence would be costly). This is beyond the scope of this work, but we schematically outlined the possible hot electron-induced chemical change of the MB molecule in Figure 5.27.

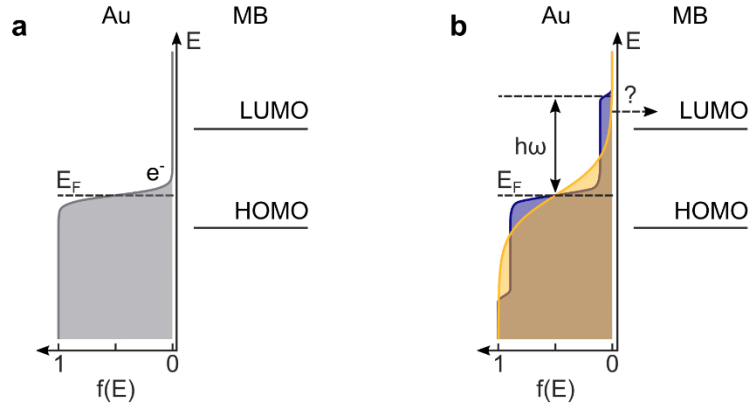

Figure 5.27 ***Schematic diagram of electron energy distribution in NPoM with respect to molecular orbitals of MB.*** *Electrons are distributed around the Fermi energy (E_F) that lies between the highest occupied molecular orbital (HOMO) and lowest unoccupied molecular orbital (LUMO) of MB. a) System at room temperature without any external influence, b) system under laser illumination with photon energy hω showing non-thermal electron distribution immediately after photon absorption (blue) and a corresponding hot electron distribution after self-thermalisation by electron-electron scattering (yellow). The tentative electron tunnelling into the LUMO of MB is shown by a dashed horizontal arrow.*

Figure 5.27a shows electron distribution in the gold NPoM nanocavity at room temperature without the influence of an external laser as well as the most relevant orbitals of MB for chemical reactions: LUMO and the highest occupied molecular orbital (HOMO). The electrons in gold are distributed around the Fermi energy (E_F) with a small fraction above E_F due to thermal excitations. In Figure 5.27b, incident photons excite electrons into a non-thermal distribution (blue) with energies up to the photon energy. Within ~ 100 fs, the electrons self-thermalise into a thermal distribution with effective temperature above the lattice temperature (yellow). Both, pre-thermalised and hot electrons could in principle tunnel into the LUMO of MB and initiate a chemical reaction.

The pre-thermalised or hot electron mediated mechanism is compatible with the experimentally observed timescale of the photochemical change of < 265 fs. The peak laser intensity threshold could also suggest a multielectron mechanism such as the well-known MB reduction in water into leucomethylene blue.[211] Specifically, MB can gain two electrons and a proton to form an oxidated state that is characteristic

by losing the electronic resonance in the visible spectrum, which would also explain the loss of SERS signal at 633 nm. Yet, it is not clear whether a multielectron mechanism is compatible with the short lifetimes of the out-of-equilibrium electrons, or what molecular species could serve as a proton donor for MB encapsulated in CB7 in the oil-immersion sample.

To shed more light into the role of pre-thermalised and hot electrons in the photoinduced changes, it would be interesting to repeat the experiment at a different pulsed laser wavelength and monitor the peak intensity threshold or employ a different dye molecule to vary the E_F-LUMO energy gap. Removing the laser-molecule resonance would also shed more light on the chemical products after the photochemistry took place by monitoring the SERS signatures of the products (with no loss of SERS due to loss of resonance enhancement). Finally, if MB reduction explains our observations, repeating the measurements in water immersion would allow us to easily introduce oxidising or reducing agents into the sample, which should allow us to reverse the laser-induced chemistry.

To summarise, lattice heating does not explain the observed laser-induced photochemistry in the high peak laser intensity regime. The hot electrons under experimental conditions here reach exponential distributions with a characteristic temperature of ~ 550 K, which is far below temperatures reported for other molecules in metallic nanojunctions. Yet, both pre-thermalised and hot electrons in principle match the experimentally observed timescales and could therefore contribute to the observed photochemistry. A more definitive insight could be obtained by repeating the measurement with different laser wavelength or molecule. Alternatively, water immersion could be used to combine laser-induced and traditional chemistry.

Ionisation by strong electric fields

The NPoM nanoantenna yields an extremely high plasmonic enhancement due to the small, only one molecule thick, separation between the nanoparticle and the mirror.[186] Recall that the experimentally-determined non-linear SERS loss depends on the peak intensity of the laser and therefore the instantaneous electric field inside the NPoM hotspot. Under these extreme conditions, non-linear processes can start to dominate the observable physics and here we explore whether the observed, peak intensity-dependent SERS loss can be explained by multi-photon ionisation (MPI) or electron tunnelling out of the MB molecule inside the NPoM hotspot.

MPI has been observed for peak intensities of $10^{11\text{-}12}$ μW μm^{-2} in noble gases.[212] At even higher electric field intensities, the external field is strong enough to cause electron tunnelling out of the molecular potential.[213] The onset of this tunnelling regime is defined by the Keldysh parameter, γ. For $\gamma < 1$, tunnelling dominates the ionisation mechanism and for $\gamma > 1$, ionisation occurs via non-linear photon absorption.[214]

The Keldysh parameter can be calculated as follows:

$$\gamma = \sqrt{\frac{I_p}{2U_p}} = \gamma; U_p = \frac{e^2 E_0^2}{4\, m_e \omega_0^2}$$

(5.4)

where I_p is the ionisation potential of the atom or molecule and U_p is the ponderomotive energy equal to the mean kinetic energy of a free electron in an electromagnetic field. It can be calculated from physical constants including the electron charge, e, electron mass, m_e, and laser-dependent quantities of the electric field generated at the sample, E_0, and laser frequency, ω_0. Inserting the values of the physical constants, the equation can be written as:

$$\gamma \approx \sqrt{\frac{5.38\ 10^{16}\ I_p[eV]}{enh\ I_{peak}[\mu W\ \mu m^{-2}]\ \lambda^2[nm]}}$$

(5.5)

where I_{peak} is the peak laser intensity, λ the laser wavelength. Thus, the Keldysh parameter is proportional to the inverse square root of the electric field intensity. Note that an enhancement factor, enh is added to yield the near-field intensity in the NPoM gap. Inserting the experimental values of $I_p = \sim 5\ eV$,[215] $enh = 10^4$ (Table 5.**1**), and $\lambda = 785\ nm$, we obtain $\gamma = 66$ at the onset of the non-linear regime ($I_{peak} = 10^4 \mu W\ \mu m^{-2}$) and $\gamma = 6$ at the highest experimental peak powers ($I_{peak} = 10^6 \mu W\ \mu m^{-2}$)). The Keldysh parameter suggests that tunnelling can be neglected, however multi-photon ionisation could be possible.

Since multi-photon ionisation probability drops dramatically with the number of required photons, a definitive check could be varying the laser wavelength and observing the laser intensity onset of the non-linear damage mechanism. Here, we conclude that it is a possible contribution to the observed damage satisfying the ultrashort timescale requirement and feasibility estimated by the Keldysh

parameter. Next, we explore the final proposed mechanism that can be responsible for the observed ultrafast SERS loss: vibrational pumping.

Vibrational pumping

Vibrational pumping has been long-debated in the context of SERS.[216] Stimulated by the observation of a quadratic dependence of the anti-Stokes signal on illumination intensity, most of the vibrational pumping mechanism focused on distinguishing optical pumping via Stokes scattering from a thermal vibrational population induced by plasmonic heating.[217] In fact, optical vibrational pumping has been proposed to explain anomalous anti-Stokes to Stokes ratios in an NPoM platform with a thiol molecular spacer.[191] For an optical vibrational pumping to reach a phototoxic regime, several photons must interact with the molecule within the vibrational relaxation time.[191] This is easily verified by integrating the Stokes photons in a picosecond SERS spectrum such as the one in Figure 5.17 and dividing by the laser repetition rate and detection efficiency.

$$n_{Stokes,pulse} = \frac{I_{SERS}}{rep_{las}\ eff} \tag{5.6}$$

For the strongest Raman band at 1625 cm^{-1}, we get $I_{SERS} = 3 \cdot 10^5 cts\ /\ s$, the laser repetition rate is 76 MHz and the detection efficiency approximately 0.2 (in addition to the correction factors already assumed in the spectral normalisation). This yields approximately 0.02 Stokes photon per pulse at pulse powers close to the damage threshold. As such, optical pumping does not seem to explain the observed phototoxicity.

Vibrational pumping has also been proposed via dark channels.[210,218] A stimulated Raman experiment on a related system of a nanoparticle dimer[210] demonstrated an inversion of the vibrational population attributing it to scattering of the plasmon electrons on the molecular layer in the hotspot causing electron-vibration excitation.

This mechanism could explain our experimental observations. Firstly, plasmon relaxation occurs on a 10 fs timescale[41] matching the experimental estimate of a < 265 fs timescale. Furthermore, we would expect pumping dependence on the scattering cross-section of the NPoM that is proportional to plasmon damping processes other than collision and Laudau processes due to the electrons and crystal lattice within the plasmonic metal itself. This does seem to be the case according to the FDTD calculations (Figure 5.23). Moreover, the peak power threshold of 10^4 µW µm^{-2} can also be explained by the surface plasmon damping mechanism. Estimating

the number of photons per pulse interacting with the 60 nm NPoM from the peak laser intensity, NPoM extinction cross-section (Figure 5.23) divided by the photon energy at 785 nm. $I_{peak}\,\sigma_{ext}\,/\,E_{photon}\cdot\tau_{plasmon}$ yields ~ 3 photons for plasmon decay time of 10 fs at 785 nm. Assuming an almost unity efficiency of the electron-vibration scattering,[210] this would give vibrational pumping to a $v = 3$ level that was shown to be irreversibly phototoxic for an aromatic thiol inside an NPoM cavity.[191]

To verify this mechanism further, several experiments could be conducted. As plasmon damping depends on molecular dipole and causes slight broadening of the dark-field scattering spectra of the nanoantenna,[219] it would be interesting to repeat the experiments on molecules with different, or differently oriented, dipoles and correlate high-resolution DF spectra width to the non-linear SERS loss at high peak powers. Also, it is interesting that the strongest multi-photon phototoxicity is observed for 60 nm NPoM with a dipole resonance between the incident laser and the CC stretch Stokes (Figure 5.16c). This suggests that tuning the cavity resonance could selectively pump different vibrational modes, which could open doors to selective bond breaking and new exciting chemistry, all in the ground electronic state of the molecule. Finally, our data indicate that tuning the plasmon resonance to the laser wavelength maximises the SERS intensity and a further redshift results in a more severe photodamage. This resonance separation of the maximum SERS and maximum damage regime is encouraging as it enables experimentalists to carefully tune the experimental conditions depending on the aim to study few-molecule SERS or exotic non-linear physics. The latter processes can be interesting from the point of nanocatalysis or fundamental physics at a few-molecule limit if suitable wavelength tuning allows for the multi-photon ionisation.

Overall, the experimentally observed ultrafast SERS loss is most likely related to a chemical change of MB that shifts its resonance out of the visible spectrum range causing a decrease in the observed SERS. This could occur by pre-thermalised or hot electron tunnelling into the LUMO of MB, a multiphoton ionisation or a vibrational pumping followed by bond dissociation. Lattice heating can be convincingly ruled out by its long timescale, pulse energy dependence and only ~ 2 K estimates based on FDTD simulated cross-sections and experimental parameters. Further insight into the mechanism could be gained by varying the pulsed laser wavelength and repeating the measurements in non-resonant SERS settings either by varying the CW laser wavelength or the molecule. Our preliminary simultaneous dark-field scattering and SERS measurements (not shown here) revealed that the NPoM cavity

remains intact after the pulsed illumination further supporting the conclusions above.

Feasibility of time-resolved SERS at a single-NPoM level

The non-linear SERS loss process represents a fundamental limit to maximum achievable SERS intensity for the MB-NPoM system. Yet, the SERS loss scales with power quite slowly: the remaining SERS after pulsed laser exposure is inversely proportional to the peak intensity of the laser:

$$SERS_{after} = SERS_{initial} / I_{pulsed,peak} \quad (5.7)$$

Therefore, spontaneous picosecond Raman should be well-suited to investigate vibrational dynamics in plasmonic hotspots as the laser pulse can be stretched to several picoseconds without a steep loss of signal. This contrasts with stimulated Raman techniques where the signal depends non-linearly on the pulse length (peak intensity).

We tested the feasibility of picosecond Raman experiments by verifying the possibility to obtain a clear SERS spectrum and stable pump-probe baseline on a single 60 nm NPoM. The importance of the latter parameter should not be underestimated because it is necessary to disentangle the pump-probe signal from random fluctuations, which involve spectral shifts of Raman bands, intensity fluctuations up to 2 orders of magnitude and even appearance of new Raman peaks.[171,174,179,220]

To take advantage of the ~ 100-fold enhancement from resonance Raman at 633 nm, we set both pump at the probe to 633 nm and modulated each beam with a shutter. We spectrally filtered the laser bandwidth to ~ 10 cm^{-1} yielding a 4 ps pulse length. We set the pulse time delay to 25 ps, which should probe the system after all vibrations have decayed and the pump-probe signal should report purely on SERS fluctuations inherent to the NPoM platform.

An example dataset for a single 60 nm NPoM is shown in Figure 5.28. The probe-only SERS spectra (Figure 5.28a) allow to clearly distinguish the two most prominent peaks at 1400 and 1625 cm^{-1}. The pump-probe signal at long time delay (Figure 5.28b) shows fluctuation of a few-percent after averaging 9 measurements (~ 20 s of signal integration in total). Therefore, pump-probe picosecond SERS looks promising to study vibrational dynamics of molecules inside plasmonic hotspots at a single-hotspot level and we are now in a position to probe the full temporal evolution of the SERS spectra.

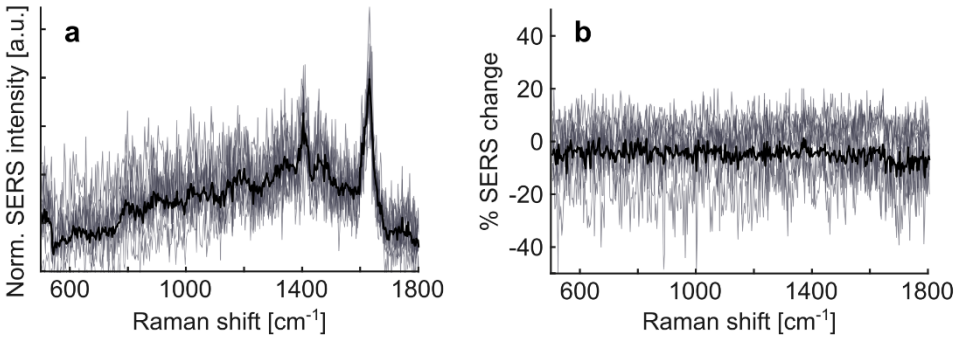

Figure 5.28 ***Pump-probe SERS at 633 nm and 25 ps pulse delay****. a) Picosecond SERS from the probe only. b) Pump-probe SERS evaluated as (pump+probe)/(pump only + probe only). Each plot shows nine repeated measurements on the same NPoM and their average in black.*

5.5 Conclusions and future outlook

In this chapter, we have explored SERS response of methylene blue molecules coupled to a nanoparticle on a mirror nanoantenna. We presented a new way of sample assembly using oil-immersion that yielded 150-fold improvement in detected signal compared to literature. Using finite-difference time-domain simulations and CW SERS at two wavelengths, we established the dominance of electronic resonance over the cavity resonance in enhancing the SERS molecular SERS signal. Using a two-colour concurrent CW and pulsed illumination, we characterised the relative SERS loss under peak powers across five orders of magnitude finding a linear and a non-linear phototoxicity regimes. In the former case, SERS decreased with average illumination power due to gold atom rearrangement within the nanoantenna gap as previously characterised in the literature. The non-linear mechanism could be explained by pre-thermalised or hot electron-induced chemistry, multiphoton ionisation or plasmon-mediated vibrational pumping, based on the sub-picosecond timescale and dependence on the nanoantenna resonance. Bulk heating of the gold lattice was eliminated based on experimental peak power scaling and timescale as well as very low temperature increase estimated from FDTD simulated cross-sections and experimental

parameters. This is an important distinction in itself as many recently-published hot electron-powered reactions are being challenged by alternative explanations based on lattice heating. Further light could be shed on the underlying photochemistry by repeating the experiments with different energy overlaps of the laser and the electronic transitions of the molecule or employing a water-immersion sample configuration that would provide an additional chemical degree of freedom.

Our findings open exciting possibilities for ultrafast studies in a few-molecule limit. Firstly, based on the Keldysh parameter, the highest employed peak intensities were inside the regime of multi-photon ionisation of methylene blue and within a few orders of magnitude of electron tunnelling from the molecular potential. This suggests that the nanoparticle on a mirror platform in the oil-immersion configuration could be useful to study physics under extreme electric fields.

Secondly, frustrating as a by-product of ultrafast SERS, the vibrational pumping by plasmon scattering could actually be exploited for vibrationally-assisted bond dissociation. By tuning the plasmon resonance to different vibrations, different selection rules could be achieved than in classical photoexcitation, provided the plasmon resonance was sufficiently narrow. The oil-immersed nanoparticle on a mirror platform would additionally ensure few-molecule observation at a time – down to the very fundamental limit of chemistry.

Finally, based on our preliminary data, spontaneous pump-probe Raman experiments should be suitable to study evolution of the molecules in plasmonic nanojunctions in time. Considering the scarcity of ultrafast SERS studies, our results show that maximising the in-and out-coupling by oil immersion and stretching the laser pulses to a few picoseconds are key to maximise signal and avoid phototoxicity, respectively. Furthermore, as heating and collapse of the nanoantenna do not seem to be the limiting factors, the gold mirror heat conductivity likely plays an important role in the plasmonic system design, offering an advantage over dimer nanoantennas.

6 Conclusions

6.1 Summary

In this thesis, we have used light to interrogate the fundamental properties of matter at a single-molecule and single-particle level. Using microscopy, we were able to "zoom in" down to the diffraction limit. To bridge the remaining gap towards the few-nanometre length scale of molecules, we employed metallic nanoantennas that not only concentrate electromagnetic fields into sub-diffraction hotspots, but also amplify the molecular signals thereby enormously facilitating their detection.

We studied energy transfer in photosynthesis by recording single-molecule fluorescence photon statistics of the Fenna-Matthews-Olson (FMO) complex. This pigment-protein complex is formed by three identical subunits each containing eight chromophores and the entire unit is optimised to non-radiatively funnel excitation energy along the photosynthetic chain. By employing microscopy, a cryostat and gold nanorod antennas, we managed to detect fluorescence of the extremely dim single FMO complexes for the first time at 77 K and room temperature. Furthermore, we recorded fluorescence photon statistics on the single complexes revealing that the entire system behaved as a single emitter. This constitutes the first experimental confirmation of energy transfer between the three subunits of the FMO complex, pointing to a likely role of excitation annihilation in the regulatory mechanisms of photosynthesis. Lastly, for resonantly enhanced FMO complexes, plasmonic coupling was able to shorten a fluorescence lifetime component below the timescale of the energy transfer between the subunits. The dominance of this short component correlated with an increase in the effective number of emitters up to the number of FMO subunits as reported by the single-complex photon statistics. This suggests that the plasmonic nanorods managed to outcompete the neighbouring pigment-protein subunits in excitation energy harvesting. Therefore, nanoantennas could be used to affect the amount of excitation annihilation in multichromophore systems to the extent of effectively uncoupling its individual subunits.

Secondly, we developed an automated SERS microscope capable of high-throughput single-particle screening. Using a wide-field image to identify individual nanoparticles followed by a single-spot SERS timetrace measurement, we were able to characterise the SERS sensing potential of ten common nanoparticle types functionalised by 2-naphthalenethiol at two different wavelengths. We sampled over a thousand nanoparticles for each set of conditions and evaluated SERS parameters such as intensity, signal to background ratio and temporal stability. The

single-spot distributions revealed information beyond the averaged value available in bulk measurements and more importantly, allowed correlating different parameters. For example, comparing the background-subtracted SERS to the overall Stokes-shifted signal for each measurement gave insight into the variability of SERS hotspots within each nanoparticle type, which is a key parameter for quantitative SERS sensing. Interestingly, the increased hotspot variability was linked to intensity variations in the broad SERS background, most prominent when the laser matched the plasmon resonance of the nanoparticle. Therefore, tuning the laser to the nanoparticle resonance may be counterintuitively a poor strategy for SERS sensing and redshifting the laser slightly may improve the reproducibility by selecting a smaller subset of SERS hotspots that give rise to the observed signal. Lastly, we combined the SERS measurement with dark-field scattering imaging that allowed classification of the measurements between single and multiple particles. We found that distributions of SERS performance among single and a few nanoparticles were indistinguishable marking the probed platforms unsuitable for quantitative SERS sensing without additional modifications. Overall, this single-spot analysis directly probed the relationship between various nanoscale properties of SERS substrates, yielding a more accurate insight than bulk techniques. This approach can greatly facilitate optimisation of new generations of more reproducible SERS platforms.

In the final chapter, we studied the effect of gold nanostructures beyond amplifying weak molecular signals, to actually drive chemistry of molecules at their surface. We used the automated single-particle SERS microscope to study photochemistry induced by a pulsed laser at metallic nanocavities formed by a gold nanoparticle close to a gold “mirror” surface. By developing a new sample assembly method compatible with oil-immersion microscopy we managed to increase SERS signal of the < 10 methylene blue molecules inside the hotspot of one nanojunction by 150 times compared to previous literature. This allowed us to build sufficient single-particle statistics and probe the impact of pulsed laser on a continuous wave SERS of methylene blue for different pulse lengths and average powers. We uncovered two regimes: an average power-dependent SERS loss down to 50 % assigned to movement of gold atoms in the gap and a peak power threshold above which laser-induced SERS loss was dominated by an irreversible ultrafast process on a sub-265 fs timescale. The peak power dependence and ultrafast timescale eliminated lattice heating as the driving force for the loss of the molecular SERS signal pointing to plasmon-mediated vibrational pumping, multiphoton ionisation or hot-electron driven transformation. The relative SERS retention after pulsed laser illumination was inversely proportional to the peak power, which marks spontaneous picosecond Raman with linear power dependence as a much more

suitable technique to study chemical reactions at metallic surfaces than the currently prevalent non-linear Raman methods.

6.2 Future outlook

Overall, our work can inspire future research into both fundamental and applied directions. It would be interesting to repeat the single-molecule fluorescence experiments on a range of photosynthetic complexes to probe the universality of the relationship between the lifetime shortening and photon emission statistics. This could shed more light on the role of excitation annihilation in photosynthesis regulation and its possible link to the prevalence of circular structures with the FMO complex trimer representing the most primitive form of a circle. Furthermore, the promising findings from the experiments in the nanoparticle on a mirror cavity suggest that the nanojunction itself withstands high instantaneous photon fluxes making it suitable for ultrafast spontaneous Raman experiments. These combine a picosecond time resolution with chemically-rich information and can therefore address the mechanism of reactions on metallic surfaces including the longstanding debate on the role of lattice heating compared to hot electrons.

On the more applied side, the holistic nanoscale characterisation of SERS nanoparticles will accelerate the development of nanoparticle architectures suitable for quantitative SERS. SERS substrates that yield reproducible enhancements will unlock the possibility of chemically-specific ultrasensitive tests, enabling more precise testing relevant to food safety, environmental contamination or earlier medical diagnoses paving way for personalised medicine. Furthermore, the insight into plasmonically-induced reactions from the proposed spontaneous picosecond Raman experiments on plasmonic nanocavities can yield crucial insight into the field of plasmonic catalysis. Finding new reaction pathways that do not rely on traditional heat-based catalysis for industrially-important chemicals such as hydrogen production can immensely reduce the worldwide energy consumption, which is key towards managing the current global climate crisis.

In summary, this thesis yielded fundamental single-molecule and single-particle insights into energy transfer in photosynthesis, potential of metallic nanoparticles for chemically-specific ultrasensitive sensing and ultrafast plasmon-mediated processes in metallic nanocavities. These findings will drive further research into the structure-function relationship in photosynthetic complexes and the mechanism of plasmonically-induced chemical reactions. Hopefully, some of our research will also contribute towards practical applications of SERS sensing and plasmonic catalysis, addressing the current needs of society for better and greener technologies.

Acknowledgements

Although the idea of a PhD thesis is to show one's ability to conduct research independently, there are many people who accompanied me through my PhD journey and the work in this thesis would not be possible without their contribution. First and foremost, Niek, thank you for the opportunity to do my PhD research in your group. Also, thank you for the scientific freedom that, I admit was not "comfortable" at the beginning, but ultimately made me a much better and independent scientist. I do value this greatly. I am also grateful for your support of the student chapter initiatives and during my thesis submission. Finally, I enjoyed and will miss our little agricultural exchanges like turning the lemons from your garden into tasty beverages!

A special acknowledgement goes to the thesis committee members: Dr. Emilie Wientjes, Prof. Eric O. Potma and Prof. María F. García-Parajo. Thank you for your useful comments that enhanced the quality of the thesis.

Next, I would like to acknowledge the crucial help I received. Luca, we embarked on the single-molecule journey together and you helped me wrap my head around so many things from setup technicalities to data analysis. Moreover, you were always cheerful and patient (c.f. "why" and writing my first monster matlab code!). I am really glad you accompanied me in the fluorescence part of my PhD journey! Transitioning to Raman, I could not have progressed as quickly as I did without the support of Matz. Thank you for passing on your knowledge of spectroscopy microscopy and non-linear optics. Finally, thanks to Johann and Saurabh, for the many hours spent in the cleanroom for the FMO and NPoM projects.

There were also people who did not work on my project, but profoundly shaped my PhD experience. Monse, we spent the first years of our PhDs essentially living in lab 2, sharing not only the optical table, but also all the joys and struggles that come with science. I am fortunate to have had you as a partner in crime inside the lab and outside. Thank you for all the laughs and motivation, cleanroom sessions, hobbit-style meal schedules, language exchanges (the dangers of reflexive verbs!) and just being a great friend. Thank you, Lisa, for being the bubbly core of the group and remembering everyone's birthdays, Pawel, for your infinite inner peace and joy for polarisation, Unai, for the intensive course on Spanish punk and the entire NvH group: Alex B, Sylwester, Alex D, Nicola, Esther, Vikas, Richard, Nick, Giulia, Guillermo, Joe and Sandra.

All the work presented here was also greatly facilitated by all the ICFO units that allowed me to spend most of my time on doing science. Namely, Carlos, Núria and the maintenance team, electronic and mechanical workshops, Vittoria, the biolab team, the IT support, the purchasing department, the cleaning staff and the very nice bus driver who always waited…

Last but not least, a big thanks to my family for the unconditional support and sharing my excitement and struggles along the PhD journey. Also, thank you, Igor, for being a constant that grounded me during these years. You always found time to listen to my “important” daily challenges at work and created an environment where I could fully immerse myself into science – at times for weeks, which made a lot of this thesis possible.

7 Bibliography

1 J. Neitz and M. Neitz, *Eye*, 2017, **31**, 286–300.

2 C. Hiramatsu, A. D. Melin, W. L. Allen, C. Dubuc and J. P. Higham, *Proc. R. Soc. B Biol. Sci.*, 2017, **284**, 20162458.

3 A. U. Acuña, F. Amat-Guerri, P. Morcillo, M. Liras and B. Rodríguez, *Org. Lett.*, 2009, **11**, 3020–3023.

4 A. J. M. Wollman, R. Nudd, E. G. Hedlund and M. C. Leake, *Open Biol.*, 2015, **5**, 150019.

5 In *Newton: Philosophical Writings*, Cambridge University Press, 2014, pp. 1–14.

6 E. Abbe, *Arch. für Mikroskopische Anat.*, 1873, **9**, 413–468.

7 B. Valeur and M. N. Berberan-Santos, *J. Chem. Educ.*, 2011, **88**, 731–738.

8 W. E. Moerner and L. Kador, *Phys. Rev. Lett.*, 1989, **62**, 2535–2538.

9 M. Orrit and J. Bernard, *Phys. Rev. Lett.*, 1990, **65**, 2716–2719.

10 M. Fleischmann, P. J. Hendra and A. J. McQuillan, *Chem. Phys. Lett.*, 1974, **26**, 163–166.

11 U. C. Fischer and D. W. Pohl, *Phys. Rev. Lett.*, 1989, **62**, 458–461.

12 W. E. Moerner, *J. Phys. Chem. B*, 2002, **106**, 910–927.

13 W. E. Moerner, Y. Shechtman and Q. Wang, *Faraday Discuss.*, 2015, **184**, 9–36.

14 S. Adhikari and M. Orrit, *J. Chem. Phys.*, 2022, **156**, 160903.

15 G. Acuna, D. Grohmann and P. Tinnefeld, *FEBS Lett.*, 2014, **588**, 3547–3552.

16 L. Novotny and B. Hecht, *Principles of nano-optics*, 2009.

17 W. E. Moerner and D. P. Fromm, *Rev. Sci. Instrum.*, 2003, **74**, 3597–3619.

18 J. R. Lakowicz, *Principles of Fluorescence Spectroscopy*, Springer US, Boston, MA, 3rd edn., 2006.

19 P. W. Atkins and R. S. Friedman, *Molecular Quantum Mechanics*, Oxford Oxford University Press, 3rd edn., 2001.

20 E. Le Ru and P. Etchegoin, *Principles of Surface-Enhanced Raman Spectroscopy and Related Plasmonic Effects*, Elsevier Science, 1st edn., 2008.

21 D. A. Long, *The Raman effect: a unified treatment of the theory of Raman scattering by molecules.*, John Wiley & Sons Ltd, 1st edn., 2002.

22 E. C. Le Ru, E. Blackie, M. Meyer and P. G. Etchegoin, *J. Phys. Chem. C*, 2007, **111**, 13794–13803.

23 F. Pahang, P. Parvin, H. Ghafoori-Fard, A. Bavali and A. Moafi, *OSA Contin.*,

2020, **3**, 688.
24 W. R. Ware, *J. Phys. Chem.*, 1962, **66**, 455–458.
25 C. G. Hübner, A. Renn, I. Renge and U. P. Wild, *J. Chem. Phys.*, 2001, **115**, 9619–9622.
26 Q. Zheng, S. Jockusch, Z. Zhou and S. C. Blanchard, *Photochem. Photobiol.*, 2014, **90**, 448–454.
27 K. Kneipp and H. Kneipp, *Appl. Spectrosc.*, 2006, **60**, 322A-334A.
28 P. Drude, *Ann. Phys.*, 1900, **306**, 566–613.
29 M. Dressel and G. Grüner, *Electrodynamics of Solids*, Cambridge University Press, 1st edn., 2002.
30 S. A. Maier, *PLASMONICS_Fundamentals and Applications*, Springer, 1st edn., 2007.
31 E. D. Palik, *Handbook of Optical Constants of Solids*, Academic Press, 1st edn., 1998.
32 W. J. Scouler, *Phys. Rev. Lett.*, 1967, **18**, 445–448.
33 R. Rosei, C. H. Culp and J. H. Weaver, *Phys. Rev. B*, 1974, **10**, 484–489.
34 A. Otto, *Zeitschrift für Phys. A Hadron. Nucl.*, 1968, **216**, 398–410.
35 E. Kretschmann and H. Raether, *Zeitschrift für Naturforsch. A*, 1968, **23**, 2135–2136.
36 H. Raether, *Surface Plasmons on Smooth and Rough Surfaces and on Gratings*, Springer Berlin Heidelberg, Berlin, Heidelberg, 1988, vol. 111.
37 C. F. Bohren and D. R. Huffman, *Absorption and Scattering of Light by Small Particles*, Wiley, 1998.
38 H. C. Van de Hulst and V. Twersky, *Phys. Today*, 1957, **10**, 28–30.
39 A. Crut, P. Maioli, N. Del Fatti and F. Vallée, *Chem. Soc. Rev.*, 2014, **43**, 3921.
40 R. Chikkaraddy, J. Huang, D. Kos, E. Elliott, M. Kamp, C. Guo, J. J. Baumberg and B. de Nijs, *ACS Photonics*, 2023, **10**, 493–499.
41 S. V. Boriskina, T. A. Cooper, L. Zeng, G. Ni, J. K. Tong, Y. Tsurimaki, Y. Huang, L. Meroueh, G. Mahan and G. Chen, *Adv. Opt. Photonics*, 2017, **9**, 775.
42 C. Ciracì, R. T. Hill, J. J. Mock, Y. Urzhumov, A. I. Fernández-Domínguez, S. A. Maier, J. B. Pendry, A. Chilkoti and D. R. Smith, *Science*, 2012, **337**, 1072–1074.
43 P. F. Liao and A. Wokaun, *J. Chem. Phys.*, 1982, **76**, 751–752.
44 P. Muhlschlegel, *Science*, 2005, **308**, 1607–1609.
45 A. G. Curto, G. Volpe, T. H. Taminiau, M. P. Kreuzer, R. Quidant and N. F. van Hulst, *Science*, 2010, **329**, 930–933.

46 M. Pelton, *Nat. Photonics*, 2015, **9**, 427–435.
47 S. Eustis and M. A. El-Sayed, *Chem. Soc. Rev.*, 2006, **35**, 209–217.
48 P. Anger, P. Bharadwaj and L. Novotny, *Phys. Rev. Lett.*, 2006, **96**, 113002.
49 E. Wientjes, J. Renger, A. G. Curto, R. Cogdell and N. F. van Hulst, *Phys. Chem. Chem. Phys.*, 2014, **16**, 24739–24746.
50 S. Kühn, U. Håkanson, L. Rogobete and V. Sandoghdar, *Phys. Rev. Lett.*, 2006, **97**, 017402.
51 G. W. Bryant, F. J. García de Abajo and J. Aizpurua, *Nano Lett.*, 2008, **8**, 631–636.
52 K. Kneipp, Y. Wang, H. Kneipp, L. T. Perelman, I. Itzkan, R. R. Dasari and M. S. Feld, *Phys. Rev. Lett.*, 1997, **78**, 1667–1670.
53 S. Nie and S. R. Emory, *Science*, 1997, **275**, 1102–1106.
54 R. E. Blankenship, *Molecular Mechanisms of Photosynthesis, 2nd Edition*, 2014.
55 R. J. Cogdell, A. Gall and J. Köhler, *Q. Rev. Biophys.*, 2006, **39**, 227.
56 H. Lokstein, G. Renger and J. Götze, *Molecules*, 2021, **26**, 3378.
57 M. T. W. Milder, B. Brüggemann, R. van Grondelle and J. L. Herek, *Photosynth. Res.*, 2010, **104**, 257–274.
58 R. E. Fenna and B. W. Matthews, *Nature*, 1975, **258**, 573–577.
59 D. E. Tronrud, M. F. Schmid and B. W. Matthews, *J. Mol. Biol.*, 1986, **188**, 443–454.
60 A. Kell, A. Y. Khmelnitskiy, T. Reinot and R. Jankowiak, *J. R. Soc. Interface*, 2019, **16**, 20180882.
61 J. Dostál, J. Pšenčík and D. Zigmantas, *Nat. Chem.*, 2016, **8**, 705–710.
62 Y.-F. Li, W. Zhou, R. E. Blankenship and J. P. Allen, *J. Mol. Biol.*, 1997, **271**, 456–471.
63 A. Löhner, K. Ashraf, R. J. Cogdell and J. Köhler, *Sci. Rep.*, 2016, **6**, 1–7.
64 L. Limantara, P. Koehler, B. Wilhelm, R. J. Porra and H. Scheer, *Photochem. Photobiol.*, 2006, **82**, 770.
65 G. S. Engel, T. R. Calhoun, E. L. Read, T. K. Ahn, T. Mančal, Y. C. Cheng, R. E. Blankenship and G. R. Fleming, *Nature*, 2007, **446**, 782–786.
66 E. Thyrhaug, R. Tempelaar, M. J. P. Alcocer, K. Žídek, D. Bína, J. Knoester, T. L. C. Jansen and D. Zigmantas, *Nat. Chem.*, 2018, **10**, 780–786.
67 M. Cho, H. M. Vaswani, T. Brixner, J. Stenger and G. R. Fleming, *J. Phys. Chem. B*, 2005, **109**, 10542–10556.
68 A. Khmelnitskiy, R. G. Saer, R. E. Blankenship and R. Jankowiak, *J. Phys. Chem.*

B, 2018, **122**, 3734–3743.

69 A. Khmelnitskiy, A. Kell, T. Reinot, R. G. Saer, R. E. Blankenship and R. Jankowiak, *Biochim. Biophys. Acta - Bioenerg.*, 2018, **1859**, 165–173.

70 J. Adolphs and T. Renger, *Biophys. J.*, 2006, **91**, 2778–2797.

71 G. Ritschel, J. Roden, W. T. Strunz, A. A. Aspuru-Guzik and A. Eisfeld, *J. Phys. Chem. Lett.*, 2011, **2**, 2912–2917.

72 D. E. Tronrud, J. Wen, L. Gay and R. E. Blankenship, *Photosynth. Res.*, 2009, **100**, 79–87.

73 E. Thyrhaug, K. Žídek, J. Dostál, D. Bína and D. Zigmantas, *J. Phys. Chem. Lett.*, 2016, **7**, 1653–1660.

74 S. Savikhin and W. S. Struve, *Biochemistry*, 1994, **33**, 11200–11208.

75 T. Főrster, *Discuss. Faraday Soc.*, 1959, **27**, 7–17.

76 A. Kell, K. Acharya, V. Zazubovich and R. Jankowiak, *J. Phys. Chem. Lett.*, 2014, **5**, 1450–1456.

77 N. Herascu, A. Kell, K. Acharya, R. Jankowiak, R. E. Blankenship and V. Zazubovich, *J. Phys. Chem. B*, 2014, **118**, 2032–2040.

78 V. Gulbinas, L. Valkunas, D. Kuciauskas, E. Katilius, V. Liuolia, W. Zhou and R. E. Blankenship, *J. Phys. Chem.*, 1996, **100**, 17950–17956.

79 J. Moix, J. Wu, P. Huo, D. Coker and J. Cao, *J. Phys. Chem. Lett.*, 2011, **2**, 3045–3052.

80 J. Wu, F. Liu, Y. Shen, J. Cao and R. J. Silbey, *New J. Phys.*, 2010, **12**, 105012.

81 N. C. M. Magdaong, R. G. Saer, D. M. Niedzwiedzki and R. E. Blankenship, *J. Phys. Chem. B*, 2017, **121**, 4700–4712.

82 G. S. Orf, D. M. Niedzwiedzki and R. E. Blankenship, *J. Phys. Chem. B*, 2014, **118**, 2058–2069.

83 G. S. Orf, R. G. Saer, D. M. Niedzwiedzki, H. Zhang, C. L. McIntosh, J. W. Schultz, L. M. Mirica and R. E. Blankenship, *Proc. Natl. Acad. Sci. U. S. A.*, 2016, **113**, E4486–E4493.

84 J. Hofkens, M. Cotlet, T. Vosch, P. Tinnefeld, K. D. Weston, C. Ego, A. Grimsdale, K. Mullen, D. Beljonne, J. L. Bredas, S. Jordens, G. Schweitzer, M. Sauer and F. De Schryver, *Proc. Natl. Acad. Sci.*, 2003, **100**, 13146–13151.

85 R. Monshouwer, M. Abrahamsson, F. van Mourik and R. van Grondelle, *J. Phys. Chem. B*, 1997, **101**, 7241–7248.

86 E. Wientjes, J. Renger, R. Cogdell and N. F. van Hulst, *J. Phys. Chem. Lett.*, 2016, **7**, 1604–1609.

87 J. Wen, H. Zhang, M. L. Gross and R. E. Blankenship, *Biochemistry*, 2011, **50**,

3502–3511.

88 V. Cherezov, J. Clogston, M. Z. Papiz and M. Caffrey, *J. Mol. Biol.*, 2006, **357**, 1605–1618.

89 E. Wientjes, J. Renger, A. G. Curto, R. Cogdell and N. F. van Hulst, *Nat. Commun.*, 2014, **5**, 4236.

90 L. Saemisch, Universität Bonn, 2016.

91 W. E. Moerner and M. Orrit, *Science*, 1999, **283**, 1670–1676.

92 M. Stepanova and S. Dew, Eds., *Nanofabrication*, Springer Vienna, Vienna, 2012.

93 B. B. Goldberg, S. B. Ippolito, L. Novotny, Zhiheng Liu and M. S. Unlu, *IEEE J. Sel. Top. Quantum Electron.*, 2002, **8**, 1051–1059.

94 S. M. Mansfield and G. S. Kino, *Appl. Phys. Lett.*, 1990, **57**, 2615–2616.

95 D. P. O'Leary and B. W. Rust, *Comput. Optim. Appl.*, 2013, **54**, 579–593.

96 M. Rätsep and A. Freiberg, *Chem. Phys. Lett.*, 2007, **434**, 306–311.

97 P. Bharadwaj, B. Deutsch and L. Novotny, *Adv. Opt. Photonics*, 2009, **1**, 438.

98 H. Ishitobi, T. Kai, K. Fujita, Z. Sekkat and S. Kawata, *Chem. Phys. Lett.*, 2009, **468**, 234–238.

99 T. Vosch, M. Cotlet, J. Hofkens, K. Van Der Biest, M. Lor, K. Weston, P. Tinnefeld, M. Sauer, L. Latterini, K. Müllen and F. C. De Schryver, *J. Phys. Chem. A*, 2003, **107**, 6920–6931.

100 R. A. Álvarez-Puebla and L. M. Liz-Marzán, *Energy Environ. Sci.*, 2010, **3**, 1011.

101 S. Tang, Y. Li, H. Huang, P. Li, Z. Guo, Q. Luo, Z. Wang, P. K. Chu, J. Li and X.-F. Yu, *ACS Appl. Mater. Interfaces*, 2017, **9**, 7472–7480.

102 B. Lin, J. Chen, Y. Zeng, L. Li, B. Qiu, Z. Lin and L. Guo, *ACS Sensors*, 2019, **4**, 1844–1850.

103 N. Logan, S. A. Haughey, L. Liu, D. T. Burns, B. Quinn, C. Cao and C. T. Elliott, *npj Sci. Food*, 2022, **6**, 3.

104 J. Luo, Z. Wang, Y. Li, C. Wang, J. Sun, W. Ye, X. Wang and B. Shao, *Sensors Actuators B Chem.*, 2021, **347**, 130602.

105 K. Monisha, K. Suresh, A. Bankapur and S. D. George, *Sensors Actuators B Chem.*, 2023, **377**, 133047.

106 P. RiveraGil, C. Vazquez-Vazquez, V. Giannini, M. P. Callao, W. J. Parak, M. A. Correa-Duarte and R. A. Alvarez-Puebla, *Angew. Chemie Int. Ed.*, 2013, **52**, 13694–13698.

107 Z. Zhang, X. Han, Z. Wang, Z. Yang, W. Zhang, J. Li, H. Yang, X. Y. Ling and B. Xing, *Chem. Commun.*, 2018, **54**, 7022–7025.

108 X. Qian, X.-H. Peng, D. O. Ansari, Q. Yin-Goen, G. Z. Chen, D. M. Shin, L. Yang, A. N. Young, M. D. Wang and S. Nie, *Nat. Biotechnol.*, 2008, **26**, 83–90.

109 D. Jimenez de Aberasturi, A. B. Serrano-Montes, J. Langer, M. Henriksen-Lacey, W. J. Parak and L. M. Liz-Marzán, *Chem. Mater.*, 2016, **28**, 6779–6790.

110 L. M. Almehmadi, S. M. Curley, N. A. Tokranova, S. A. Tenenbaum and I. K. Lednev, *Sci. Rep.*, 2019, **9**, 12356.

111 W. H. Kim, J. U. Lee, S. Song, S. Kim, Y. J. Choi and S. J. Sim, *Analyst*, 2019, **144**, 1768–1776.

112 A. Zengin, U. Tamer and T. Caykara, *Biomacromolecules*, 2013, **14**, 3001–3009.

113 H. Chon, C. Lim, S.-M. Ha, Y. Ahn, E. K. Lee, S.-I. Chang, G. H. Seong and J. Choo, *Anal. Chem.*, 2010, **82**, 5290–5295.

114 M. P. Oyarzún, A. Tapia-Arellano, P. Cabrera, P. Jara-Guajardo and M. J. Kogan, *Sensors*, 2021, **21**, 2067.

115 L. Liu, P. Martinez Pancorbo, T. Xiao, S. Noguchi, M. Marumi, H. Segawa, S. Karhadkar, J. Gala de Pablo, K. Hiramatsu, Y. Kitahama, T. Itoh, J. Qu, K. Takei and K. Goda, *Adv. Opt. Mater.*, 2022, **10**, 2200054.

116 E. H. Koh, W.-C. Lee, Y.-J. Choi, J.-I. Moon, J. Jang, S.-G. Park, J. Choo, D.-H. Kim and H. S. Jung, *ACS Appl. Mater. Interfaces*, 2021, **13**, 3024–3032.

117 J. Langer, D. Jimenez de Aberasturi, J. Aizpurua, R. A. Alvarez-Puebla, B. Auguié, J. J. Baumberg, G. C. Bazan, S. E. J. Bell, A. Boisen, A. G. Brolo, J. Choo, D. Cialla-May, V. Deckert, L. Fabris, K. Faulds, F. J. García de Abajo, R. Goodacre, D. Graham, A. J. Haes, C. L. Haynes, C. Huck, T. Itoh, M. Käll, J. Kneipp, N. A. Kotov, H. Kuang, E. C. Le Ru, H. K. Lee, J.-F. Li, X. Y. Ling, S. A. Maier, T. Mayerhöfer, M. Moskovits, K. Murakoshi, J.-M. Nam, S. Nie, Y. Ozaki, I. Pastoriza-Santos, J. Perez-Juste, J. Popp, A. Pucci, S. Reich, B. Ren, G. C. Schatz, T. Shegai, S. Schlücker, L.-L. Tay, K. G. Thomas, Z.-Q. Tian, R. P. Van Duyne, T. Vo-Dinh, Y. Wang, K. A. Willets, C. Xu, H. Xu, Y. Xu, Y. S. Yamamoto, B. Zhao and L. M. Liz-Marzán, *ACS Nano*, 2020, **14**, 28–117.

118 Q. Li, X. Ge, J. Ye, Z. Li, L. Su, Y. Wu, H. Yang and J. Song, *Angew. Chemie Int. Ed.*, 2021, **60**, 7323–7332.

119 F. Nicolson, B. Andreiuk, C. Andreou, H.-T. Hsu, S. Rudder and M. F. Kircher, *Theranostics*, 2019, **9**, 5899–5913.

120 I. B. Becerril-Castro, I. Calderon, N. Pazos-Perez, L. Guerrini, F. Schulz, N. Feliu, I. Chakraborty, V. Giannini, W. J. Parak and R. A. Alvarez-Puebla, *Anal. Sens.*, , DOI:10.1002/anse.202200005.

121 Y. Fang, N.-H. Seong and D. D. Dlott, *Science*, 2008, **321**, 388–392.

122 E. C. Le Ru and P. G. Etchegoin, *Annu. Rev. Phys. Chem.*, 2012, **63**, 65–87.

123 J. Yin, T. Wu, J. Song, Q. Zhang, S. Liu, R. Xu and H. Duan, *Chem. Mater.*, 2011, **23**, 4756–4764.

124 Y. C. Cao, R. Jin and C. A. Mirkin, in *Spherical Nucleic Acids*, Jenny Stanford Publishing, 2020, vol. 17, pp. 1467–1477.

125 J. Feng, L. Xu, G. Cui, X. Wu, W. Ma, H. Kuang and C. Xu, *Biosens. Bioelectron.*, 2016, **81**, 138–142.

126 J. Shim, Y. J. Kim, J. Choe, T. G. Lee and E. You, *ACS Appl. Mater. Interfaces*, 2022, **14**, 38459–38470.

127 S. E. J. Bell, G. Charron, E. Cortés, J. Kneipp, M. L. Chapelle, J. Langer, M. Procházka, V. Tran and S. Schlücker, *Angew. Chemie Int. Ed.*, 2020, **59**, 5454–5462.

128 S. Fornasaro, F. Alsamad, M. Baia, L. A. E. Batista de Carvalho, C. Beleites, H. J. Byrne, A. Chiadò, M. Chis, M. Chisanga, A. Daniel, J. Dybas, G. Eppe, G. Falgayrac, K. Faulds, H. Gebavi, F. Giorgis, R. Goodacre, D. Graham, P. La Manna, S. Laing, L. Litti, F. M. Lyng, K. Malek, C. Malherbe, M. P. M. Marques, M. Meneghetti, E. Mitri, V. Mohaček-Grošev, C. Morasso, H. Muhamadali, P. Musto, C. Novara, M. Pannico, G. Penel, O. Piot, T. Rindzevicius, E. A. Rusu, M. S. Schmidt, V. Sergo, G. D. Sockalingum, V. Untereiner, R. Vanna, E. Wiercigroch and A. Bonifacio, *Anal. Chem.*, 2020, **92**, 4053–4064.

129 M. Liebel, I. Calderon, N. Pazos-Perez, N. F. van Hulst and R. A. Alvarez-Puebla, *Angew. Chemie*, , DOI:10.1002/ange.202200072.

130 J. T. Hugall and J. J. Baumberg, *Nano Lett.*, 2015, **15**, 2600–2604.

131 Y.-Y. Cai, J. G. Liu, L. J. Tauzin, D. Huang, E. Sung, H. Zhang, A. Joplin, W.-S. Chang, P. Nordlander and S. Link, *ACS Nano*, 2018, **12**, 976–985.

132 S. Mahajan, R. M. Cole, J. D. Speed, S. H. Pelfrey, A. E. Russell, P. N. Bartlett, S. M. Barnett and J. J. Baumberg, *J. Phys. Chem. C*, 2010, **114**, 7242–7250.

133 P. G. Etchegoin and E. C. Le Ru, *Phys. Chem. Chem. Phys.*, 2008, **10**, 6079.

134 R. Alvarez-Puebla, L. M. Liz-Marzán and F. J. García de Abajo, *J. Phys. Chem. Lett.*, 2010, **1**, 2428–2434.

135 P. Aldeanueva-Potel, E. Carbó-Argibay, N. Pazos-Pérez, S. Barbosa, I. Pastoriza-Santos, R. A. Alvarez-Puebla and L. M. Liz-Marzán, *ChemPhysChem*, 2012, **13**, 2561–2565.

136 V. Giannini, R. Rodríguez-Oliveros and J. A. Sánchez-Gil, *Plasmonics*, 2010, **5**, 99–104.

137 J. A. Snyder, S. Haymond, C. A. Parvin, A. M. Gronowski and D. G. Grenache, *Clin. Chem.*, 2005, **51**, 1830–1835.
138 C. Dallari, C. Capitini, M. Calamai, A. Trabocchi, F. S. Pavone and C. Credi, *Nanomaterials*, 2021, **11**, 665.
139 C. D. Geddes, A. Parfenov, I. Gryczynski and J. R. Lakowicz, *Chem. Phys. Lett.*, 2003, **380**, 269–272.
140 T.-S. Lin and Y.-W. Chung, *Surf. Sci.*, 1989, **207**, 539–546.
141 U. Ortiz-Orruño, A. Jo, H. Lee, N. F. van Hulst and M. Liebel, *Nano Lett.*, 2021, **21**, 317–322.
142 H. Zhou, L. Xu, Z. Ren, J. Zhu and C. Lee, *Nanoscale Adv.*, 2023, **5**, 538–570.
143 R. R. Jones, D. C. Hooper, L. Zhang, D. Wolverson and V. K. Valev, *Nanoscale Res. Lett.*, 2019, **14**, 231.
144 N. L. Gruenke, M. F. Cardinal, M. O. McAnally, R. R. Frontiera, G. C. Schatz and R. P. Van Duyne, *Chem. Soc. Rev.*, 2016, **45**, 2263–2290.
145 P. Filipczak, M. Pastorczak, T. Kardaś, M. Nejbauer, C. Radzewicz and M. Kozanecki, *J. Phys. Chem. C*, 2021, **125**, 1999–2004.
146 K. T. Crampton, A. Zeytunyan, A. S. Fast, F. T. Ladani, A. Alfonso-Garcia, M. Banik, S. Yampolsky, D. A. Fishman, E. O. Potma and V. A. Apkarian, *J. Phys. Chem. C*, 2016, **120**, 20943–20953.
147 N. C. Brandt, E. L. Keller and R. R. Frontiera, *J. Phys. Chem. Lett.*, 2016, **7**, 3178–3185.
148 E. L. Keller and R. R. Frontiera, *ACS Nano*, 2018, **12**, 5848–5855.
149 Z. Yu and R. R. Frontiera, *ACS Nano*, 2022, **16**, 847–854.
150 M. Álvarez Ortíz, Universitat Politécnica de Catalunya, 2023.
151 J.-S. Huang, V. Callegari, P. Geisler, C. Brüning, J. Kern, J. C. Prangsma, X. Wu, T. Feichtner, J. Ziegler, P. Weinmann, M. Kamp, A. Forchel, P. Biagioni, U. Sennhauser and B. Hecht, *Nat. Commun.*, 2010, **1**, 150.
152 J. Aizpurua, G. W. Bryant, L. J. Richter, F. J. García de Abajo, B. K. Kelley and T. Mallouk, *Phys. Rev. B*, 2005, **71**, 235420.
153 N. J. Halas, S. Lal, W.-S. Chang, S. Link and P. Nordlander, *Chem. Rev.*, 2011, **111**, 3913–3961.
154 P. Biagioni, J.-S. Huang and B. Hecht, *Reports Prog. Phys.*, 2012, **75**, 024402.
155 P. Nordlander, C. Oubre, E. Prodan, K. Li and M. I. Stockman, *Nano Lett.*, 2004, **4**, 899–903.
156 E. Prodan, C. Radloff, N. J. Halas and P. Nordlander, *Science*, 2003, **302**, 419–422.

157 J.-S. Huang, J. Kern, P. Geisler, P. Weinmann, M. Kamp, A. Forchel, P. Biagioni and B. Hecht, *Nano Lett.*, 2010, **10**, 2105–2110.

158 M.-W. Chu, V. Myroshnychenko, C. H. Chen, J.-P. Deng, C.-Y. Mou and F. J. García de Abajo, *Nano Lett.*, 2009, **9**, 399–404.

159 A. Alù and N. Engheta, *Phys. Rev. B*, 2008, **78**, 195111.

160 J. H. Yoon, F. Selbach, L. Schumacher, J. Jose and S. Schlücker, *ACS Photonics*, 2019, **6**, 642–648.

161 R. Chikkaraddy, V. A. Turek, Q. Lin, J. Griffiths, B. Nijs, U. F. Keyser and J. J. Baumberg, *J. Raman Spectrosc.*, 2021, **52**, 348–354.

162 S. Yampolsky, D. A. Fishman, S. Dey, E. Hulkko, M. Banik, E. O. Potma and V. A. Apkarian, *Nat. Photonics*, 2014, **8**, 650–656.

163 K. I. Assaf and W. M. Nau, *Chem. Soc. Rev.*, 2015, **44**, 394–418.

164 R. Chikkaraddy, B. de Nijs, F. Benz, S. J. Barrow, O. A. Scherman, E. Rosta, A. Demetriadou, P. Fox, O. Hess and J. J. Baumberg, *Nature*, 2016, **535**, 127–130.

165 M. E. Nedu, M. Tertis, C. Cristea and A. V. Georgescu, *Diagnostics*, , DOI:10.3390/diagnostics10040223.

166 A. Seitkazina, J.-K. Yang and S. Kim, *Precis. Futur. Med.*, 2022, **6**, 193–208.

167 C. Li, Y. Huang, K. Lai, B. A. Rasco and Y. Fan, *Food Control*, 2016, **65**, 99–105.

168 S. Cui, J. Du, T. Wang and X. Hu, *Spectrochim. Acta - Part A Mol. Biomol. Spectrosc.*, 2012, **96**, 188–192.

169 Y. Zhou, H. Yu, L. Zhang, H. Xu, L. Wu, J. Sun and L. Wang, *Microchim. Acta*, 2009, **164**, 63–68.

170 P. B. Johnson and R. W. Christy, *Phys. Rev. B*, 1972, **6**, 4370–4379.

171 W. Chen, P. Roelli, A. Ahmed, S. Verlekar, H. Hu, K. Banjac, M. Lingenfelder, T. J. Kippenberg, G. Tagliabue and C. Galland, *Nat. Commun.*, 2021, **12**, 2731.

172 Lumerical Inc., Understanding injection angles in broadband simulations, https://support.lumerical.com/hc/en-us/articles/360034382894-Understanding-injection-angles-in-broadband-simulations.

173 L. Li, T. Hutter, U. Steiner and S. Mahajan, *Analyst*, 2013, **138**, 4574.

174 F. Benz, M. K. Schmidt, A. Dreismann, R. Chikkaraddy, Y. Zhang, A. Demetriadou, C. Carnegie, H. Ohadi, B. de Nijs, R. Esteban, J. Aizpurua and J. J. Baumberg, *Science*, 2016, **354**, 726–729.

175 D. O. Sigle, S. Kasera, L. O. Herrmann, A. Palma, B. de Nijs, F. Benz, S. Mahajan, J. J. Baumberg and O. A. Scherman, *J. Phys. Chem. Lett.*, 2016, **7**, 704–710.

176 F. Benz, R. Chikkaraddy, A. Salmon, H. Ohadi, B. de Nijs, J. Mertens, C. Carnegie, R. W. Bowman and J. J. Baumberg, *J. Phys. Chem. Lett.*, 2016, **7**, 2264–2269.

177 S. Mubeen, S. Zhang, N. Kim, S. Lee, S. Krämer, H. Xu and M. Moskovits, *Nano Lett.*, 2012, **12**, 2088–2094.

178 J. Huang, D. Grys, J. Griffiths, B. de Nijs, M. Kamp, Q. Lin and J. J. Baumberg, *Sci. Adv.*, 2021, **7**, eabg1790.

179 M. Kamp, B. de Nijs, N. Kongsuwan, M. Saba, R. Chikkaraddy, C. A. Readman, W. M. Deacon, J. Griffiths, S. J. Barrow, O. S. Ojambati, D. Wright, J. Huang, O. Hess, O. A. Scherman and J. J. Baumberg, *Proc. Natl. Acad. Sci.*, 2020, **117**, 14819–14826.

180 S. Mahajan, T. C. Lee, F. Biedermann, J. T. Hugall, J. J. Baumberg and O. A. Scherman, *Phys. Chem. Chem. Phys.*, 2010, **12**, 10429–10433.

181 Y. Liu, Y. Lin and Y. Tang, *IOP Conf. Ser. Earth Environ. Sci.*, 2019, **384**, 012034.

182 W.-I. K. Chio, S. Moorthy, J. Perumal, D. U. S., I. P. Parkin, M. Olivo and T.-C. Lee, *J. Mater. Chem. C*, 2020, **8**, 7051–7058.

183 G.-Y. Chen, Y.-B. Sun, P.-C. Shi, T. Liu, Z.-H. Li, S.-H. Luo, X.-C. Wang, X.-Y. Cao, B. Ren, G.-K. Liu, L.-L. Yang and Z.-Q. Tian, *Light Sci. Appl.*, 2021, **10**, 85.

184 D. O. Sigle, S. Kasera, L. O. Herrmann, A. Palma, B. De Nijs and F. Benz, 2016, 1–13.

185 K. Bedingfield, E. Elliott, N. Kongsuwan, J. J. Baumberg and A. Demetriadou, *EPJ Appl. Metamaterials*, 2022, **9**, 3.

186 W. Chen, S. Zhang, M. Kang, W. Liu, Z. Ou, Y. Li, Y. Zhang, Z. Guan and H. Xu, *Light Sci. Appl.*, 2018, **7**, 56.

187 J.-H. Huh, J. Lee and S. Lee, *ACS Photonics*, 2018, **5**, 413–421.

188 E. Elliott, K. Bedingfield, J. Huang, S. Hu, B. de Nijs, A. Demetriadou and J. J. Baumberg, *ACS Photonics*, 2022, **9**, 2643–2651.

189 N. Kongsuwan, A. Demetriadou, M. Horton, R. Chikkaraddy, J. J. Baumberg and O. Hess, *ACS Photonics*, 2020, **7**, 463–471.

190 Q. An, G. Li, C. Tao, Y. Li, Y. Wu and W. Zhang, *Chem. Commun.*, 2008, 1989.

191 A. Lombardi, M. K. Schmidt, L. Weller, W. M. Deacon, F. Benz, B. de Nijs, J. Aizpurua and J. J. Baumberg, *Phys. Rev. X*, 2018, **8**, 011016.

192 S. Abedin, Y. Li, A. A. Sifat, K. Roy and E. O. Potma, *Nano Lett.*, 2022, **22**, 6685–6691.

193 M. Zhu, M. Li, M. Su, J. Liu, B. Liu, Y. Ge, H. Liu and J. Hu, *J. Phys. Chem. C*, 2021, **125**, 13443–13448.

194 S. Abedin, K. Roy, X. Jin, H. Xia, S. R. J. Brueck and E. O. Potma, *J. Phys. Chem. C*, 2022, **126**, 8760–8767.
195 Y. Dubi and Y. Sivan, *Light Sci. Appl.*, 2019, **8**, 89.
196 Y. Dubi, I. W. Un and Y. Sivan, *Chem. Sci.*, 2020, **11**, 5017–5027.
197 S. Mukherjee, F. Libisch, N. Large, O. Neumann, L. V Brown, J. Cheng, J. B. Lassiter, E. A. Carter, P. Nordlander and N. J. Halas, *Nano Lett.*, 2013, **13**, 240–247.
198 J. J. Baumberg, *Faraday Discuss.*, 2019, **214**, 501–511.
199 J. R. Adleman, D. A. Boyd, D. G. Goodwin and D. Psaltis, *Nano Lett.*, 2009, **9**, 4417–4423.
200 L. Mascaretti and A. Naldoni, *J. Appl. Phys.*, 2020, **128**, 041101.
201 A. Schirato, M. Maiuri, G. Cerullo and G. Della Valle, *Nanophotonics*, 2023, **12**, 1–28.
202 M. Bauer, A. Marienfeld and M. Aeschlimann, *Prog. Surf. Sci.*, 2015, **90**, 319–376.
203 M. Bonn, D. N. Denzler, S. Funk, M. Wolf, S.-S. Wellershoff and J. Hohlfeld, *Phys. Rev. B*, 2000, **61**, 1101–1105.
204 W. S. Fann, R. Storz, H. W. K. Tom and J. Bokor, *Phys. Rev. B*, 1992, **46**, 13592–13595.
205 G. Baffou, I. Bordacchini, A. Baldi and R. Quidant, *Light Sci. Appl.*, 2020, **9**, 108.
206 T. Jollans, M. Caldarola, Y. Sivan and M. Orrit, *J. Phys. Chem. A*, 2020, **124**, 6968–6976.
207 J. Huang, W. Wang, C. J. Murphy and D. G. Cahill, *Proc. Natl. Acad. Sci.*, 2014, **111**, 906–911.
208 A. Block, M. Liebel, R. Yu, M. Spector, Y. Sivan, F. J. García de Abajo and N. F. van Hulst, *Sci. Adv.*, 2019, **5**, 1–8.
209 C. Kittel, *Introduction to solid state physics*, Wiley, 8th edn., 2005.
210 K. T. Crampton, A. Fast, E. O. Potma and V. A. Apkarian, *Nano Lett.*, 2018, **18**, 5791–5796.
211 J. D. Mahlum, M. A. Pellitero and N. Arroyo-Currás, *J. Phys. Chem. C*, 2021, **125**, 9038–9049.
212 M. D. Perry, O. L. Landen, A. Szöke and E. M. Campbell, *Phys. Rev. A*, 1988, **37**, 747–760.
213 S. Kim, T.-I. Jeong, J. Park, M. F. Ciappina and S. Kim, *Nanophotonics*, 2022, **11**, 2393–2431.

214 L. V. Keldysh, *J.Exp.Theor.Phys*, 1965, **20**, 1307–1314.

215 R. G. Selsby and R. C. Nelson, *J. Mol. Spectrosc.*, 1970, **33**, 1–18.

216 E. C. Le Ru and P. G. Etchegoin, *Faraday Discuss.*, 2006, **132**, 63–75.

217 R. C. Maher, C. M. Galloway, E. C. Le Ru, L. F. Cohen and P. G. Etchegoin, *Chem. Soc. Rev.*, 2008, **37**, 965.

218 C. M. Galloway, E. C. Le Ru and P. G. Etchegoin, *Phys. Chem. Chem. Phys.*, 2009, **11**, 7372.

219 B. Foerster, V. A. Spata, E. A. Carter, C. Sönnichsen and S. Link, *Sci. Adv.*, 2019, **5**, 1–6.

220 C. Carnegie, M. Urbieta, R. Chikkaraddy, B. de Nijs, J. Griffiths, W. M. Deacon, M. Kamp, N. Zabala, J. Aizpurua and J. J. Baumberg, *Nat. Commun.*, 2020, **11**, 1–9.

8 List of publications

Photocurrent-Detected 2D Electronic Spectroscopy Reveals Ultrafast Hole Transfer in Operating PM6/Y6 Organic Solar Cells
J. Phys. Chem. Lett. **12**, 3983–3988 (2021)
https://doi.org/10.1021/acs.jpclett.1c00822

Contributed to the development of the measurement methodology.

Direct Modular Printing of Plasmonic Chemosensors
ACS Appl. Mater. Interfaces **14**, 57165–57170 (2022)
https://doi.org/10.1021/acsami.2c17202

Built the 2D scanning Raman microscope and measured the SERS maps.

Excitation energy transfer in plasmonically-enhanced Fenna-Matthews-Olson photosynthetic complexes probed by single-molecule fluorescence
In preparation

Conducted experiments, analysed data and defined the manuscript.

Ultrafast phenomena in gold plasmonic nanojunctions
In preparation

Conducted experiments, analysed data and defined the manuscript.